In Situ Metal Matrix Nanocomposites: Towards Understanding Formation Mechanisms and Microstructural Control

by

Caleb Reese

A dissertation submitted in partial fulfillment
of the requirements for the degree of
Doctor of Philosophy
(Materials Science and Engineering)
in the University of Michigan
2020

Doctoral Committee:

Professor Ashwin Shahani, Co-Chair
Assistant Professor Alan Taub, Co-Chair
Professor Brajendra Mishra, Worcester Polytechnic Institute
Professor Veera Sundararaghavan

Caleb Reese

reesecw@umich.edu

ORCID-ID: 0000-0001-8898-0741

ACKNOWLEDGEMENTS

I am tremendously grateful to my advisors, Professor Alan Taub and Professor Ashwin Shahani. Over the course of this dissertation work, your rigorous approach towards understanding the underlying mechanisms behind materials science phenomenon and willingness to jump into new research directions have shaped the way I approach my own research. Thank you both for your constant support, thoughtful mentorship and endless patience. Your scientific enthusiasm and curiosity have been inspiring and a continual source of motivation over the many unexpected turns this project has taken.

I am also grateful to my committee members, Professor Veera Sundararaghavan and Professor Brajendra Mishra. Thank you for the insight, critical feedback and guidance you provided during the course of this research work. Additionally, I am especially thankful for your flexibility and understanding these past few months as we all navigated an uncertain COVID-19 situation.

I am thankful to the University of Michigan scientists and staff who have made everything run so smoothly behind the scenes for myself and many others. Thank you to the Department of Materials Science staff – Keith McIntyre, Dr. Tim Chambers, Ying Qi, Dr. Sahar Farjami, Kevin Worth, Chris Cristian, Debbie Johnson, Renee Hilgendorf, Shelley Fellers, and Patti Vogel – for your help and advice on my sample preparation problems, equipment and computer troubleshooting, administrative issues and everything in between. Thank you to the Michigan Center of Materials Characterization staff – Bobby Kerns, Dr. Allen Hunter, Dr. Nancy Muyanja, Dr. Haiping Sun, Dr. Kai Sun, and Deanna Wendel – for your patience and providing endless guidance and assistance with the materials characterization and sample preparation needed for this dissertation.

I would like to give a special thank you to the researchers and professionals who I had the privilege of working closely with on the LIFT Melt R2-2 project. In particular, thank you to Jeremy Fedors and Professor Brajendra Mishra at Worcester Polytechnic Institute for your excellent materials processing work, discussions, and early advice that made much of this work possible. I

am also especially grateful to David Weiss at Eck Industries and Steve Udvardy at NADCA for your invaluable industry perspectives, experimental advice and discussions, and seemingly endless metallurgical knowledge. An additional very special thanks to my nanocomposites team mates at University of Michigan who I had the privilege of working and learning with on this project, Aaron Gladstein and Dr. Xun Liu. None of this work would have been possible without your experimental help and advice.

I am thankful to the beamline scientists at the Advanced Photon Source at Argonne National Laboratory for assistance with and advice on the synchrotron X-ray experiments contained in this dissertation. In particular, thanks to Dr. Vincent De Andrade, Pavel Shevchenko, and Dr. Francesco De Carlo.

Working in the Taub Lab has been a great experience and I cannot thank all my lab mates enough for making it such a collaborative and welcoming environment when I joined. Thank you to my past and present colleagues – Dr. Avi Bregman, Dr. Maya Nath, Dr. Wesley Chapkin, Dr. Yipeng He, Dr. Xun Liu, Aaron Gladstein, Randy Cheng, Anshul Singhal, Daney Zhang, Kanat Anurakparadorn, Anita Luong, Amy Langhorst, and Erika Salem. In particular, thanks to the members of the metals team for helpful discussions, experimental insights, and the occasional much needed coffee break.

Although I have not had the opportunity to work with everyone in the Shahani Lab, I am grateful to all I have had the chance to collaborate with and learn from. Thank you to Dr. Nancy Muyanja, Dr. Saman Moniri, and Dr. Insung Han for teaching me the ins and outs of synchrotron experiments, data reconstruction and image processing, and what items to avoid at the 401 Grill. Thanks to Yeqing Wang, Dr. Ning Lu, Jiwoong Kang, Paul Chao, and Geordie Lindemann for advice on sample preparation, assistance with experiments, and image processing help.

I would like to give a special thanks to Dr. Matthew Heun and Dr. Paul Harper at my undergraduate institution, Calvin College, for introducing me to scientific research and getting me excited about it in the first place. Thank you for allowing me to be a part of your labs, teaching me how to even begin to think about approaching research, and endless advice and discussions on graduate school.

I gratefully acknowledge financial support from the LIFT (Lightweight Innovations For Tomorrow) Institute, a Manufacturing Institute under contract from the Office of Naval Research

(contract # N00014-14-2-002), the National Science Foundation (award #1762657), and the University of Michigan College of Engineering.

To my family – Cliff, KJ, Janine, Sophie, Kyle, Asher, and all extended members of the Reese, Watson, Thomas, and Anderson families – thank you for your constant support and endless words of encouragement over the entirety of my education, which has lasted seemingly forever. The visits (to Nashville, Grand Rapids, and now Ann Arbor), the homecooked meals, frequent check-ins, and bags of coffee have kept me going during my time in graduate school. To my friends near and far, although I cannot list you all here, thank you for your friendship, support, and welcome occasional distractions from the lab. A special thanks to Dr. Davide Del Gaudio for your friendship and illuminating discussions at the beginning of graduate school and beyond.

Finally, and most importantly, I am endlessly grateful for my wife, Elaina. Your constant love, warmth, encouragement, wisdom, and silliness have been a source of both rest and motivation during my time here. Thank you for celebrating with me when days in the lab went well and shifting my perspective when it seemed nothing was working. I will be forever grateful that you continually remind me of the things that are really important. Graduate school has felt like it would stretch on forever on many occasions, but I am grateful for the growing together and the experiences we have shared during this time. I love you and am excited to see what comes during the next season of transitions.

TABLE OF CONTENTS

LIST OF TABLES

LIST OF FIGURES

ABSTRACT

Lightweight materials are critical to meet the ever-increasing demands for improved fuel economy in the automotive, aerospace and defense industries. Consequently, aluminum alloys have been employed extensively in these industries for structural applications owing to their high strength-to-weight ratio. However, Al alloys suffer from several shortcomings, such as poor thermal stability of mechanical properties, limiting their usage for components operating in elevated temperature environments. Recently, the incorporation of nano-scale particles in the Al matrix, termed metal matrix nanocomposites (MMNCs), has been identified as a promising approach to improved ambient and elevated temperature mechanical properties, while still retaining the lightweight benefits of Al.

MMNCs manufactured through typical *ex situ* incorporation methods, wherein pre-made particles are mixed into the matrix, can suffer from precursor contamination and undesirable particle/matrix interfacial reactions, making incorporation and large-scale processing difficult. *In situ* processing alternatives, where particles are created directly in the melt *via* direct reaction, have been demonstrated to exhibit improved particle/matrix interface stability and easier incorporation within the matrix. However, the ability to reliably control critical mechanical property-dependent particle characteristics (*i.e.*, particle size, volume fraction, and dispersion) remains a barrier to large-scale processing of *in situ* MMNCs.

The research for this dissertation is aimed at elucidating the mechanisms governing formation of the particles and provide guidance to controlling the resulting microstructure of MMNCs processed *via in situ* methods, for the purposes of informing large-scale processing efforts. In this work, we investigate the processing-microstructure-mechanical property relationships for two *in situ* processing methods, namely: *in situ* gas-liquid reaction (ISGR) for Al-AlN MMNCs and thermite-assisted self-propagating high-temperature synthesis (SHS) for Al-TiC MMNCs. We find that the SHS process is more capable of readily producing nano-scale TiC particles in a wide variety of volume fractions and dispersions dependent on processing conditions. Additionally, we report on successful SHS processing, at our industry partner, of commercial pilot-

scale quantities of *in situ* Al-TiC MMNCs exhibiting enhanced mechanical properties for relatively low amounts of particle addition. The preliminary results are a promising demonstration of the potential for commercial-scale processing of *in situ* MMNCs.

Building upon our study of large-scale processing of MMNCs, we then perform a more detailed investigation into understanding the formation mechanisms and microstructural control of the thermite-assisted SHS process. By leveraging 2D and 3D microstructural quantification techniques with a thermodynamic-based analysis, we identify three potential direct- and indirect-reaction pathways governing TiC formation and the conditions under which they are active. We also demonstrate an approach for correlating processing-property relationships *via* multivariate statistical analysis (*i.e.*, canonical correlation analysis (CCA)). Using CCA, we report on the dominant processing variables affecting final MMNC microstructure and particle characteristics and discuss the link between processing variables, reaction pathways, and resultant microstructural signatures. Our results and analysis are expected to inform a more rational approach to process control of *in situ* SHS MMNCs, as well as being applicable to other *in situ* processing methods.

CHAPTER 1
Introduction

1.1 Motivation

As global energy demands rise, and climate change considerations become increasingly important every year, the need for more fuel-efficient vehicles has become critical for the automotive, aerospace, and transportation industries. A key design goal towards improved fuel efficiency involves light-weighting, where a 10% reduction in weight can lead to a 6% increase in fuel economy [1]. Light-weighting can be accomplished *via* a variety of methods, including topology optimization and material selection [2]. However, it is critical that these designs and materials contribute to overall load reduction without sacrificing performance. To this end, lightweight metals such as Al have been employed extensively in these industries for a wide variety of structural applications, owing to its relatively high strength to weight ratio [2]. However, Al alloys suffer from several shortcomings, such as poor stability of mechanical properties above 200 °C, limiting their usage in components in high temperature environments (*e.g.*, Al automotive engine blocks currently require cast Fe liners in the cylinder and Al turbochargers have to operate at lower temperatures reducing efficiency). Consequently, material processing routes to improve the mechanical performance of Al-based materials (at both ambient and elevated temperatures) is of great interest.

A wide variety of approaches to strengthen Al alloys exist, including intermetallic strengthening [3], solid solution strengthening [4], precipitation hardening [5], and work hardening [6]. However, these processing approaches are not without their drawbacks. For example, work hardening increases the strength of the material through grain size reduction but also causes the ductility to suffer. Precipitation hardening strengthens the material through the introduction of nanoscale precipitates, but is also subject to over-aging and significant precipitate coarsening in elevated temperature applications [7, 8]. Recently, a composite approach involving the incorporation of hard nanoscale particles (commonly ceramic) directly in the Al matrix, termed metal matrix nanocomposites (MMNCs), has attracted much attention as a promising alternative.

MMNCs are attractive due to their ability to leverage the high strength and stiffness of the nanoparticles, while still retaining the ductility of the matrix at relatively low volume percentages, leading to improved mechanical properties [9, 10]. Furthermore, MMNCs are advantageous due to the stability (*e.g.* absence of coarsening or degradation) of the particles at elevated temperatures (*e.g.*, 200 – 350 °C), making them ideal for applications requiring higher temperature operating environments [7, 9, 10 ,11, 12, 13]. Consequently, Al-based MMNCs are a promising material for Al-based structural components with low weight, high strength, and high temperature-stable characteristics.

In processing MMNCs, the reinforcing particles are commonly pre-made and added to the melt *ex situ* (in powder form), allowing for a wide variety of reinforcement/matrix combinations. The reinforcement particles are typically composed of hard ceramic materials, such as nitrides, carbides, and oxides, but incorporation of other materials such as carbon nanotubes have also been demonstrated [9, 12, 13]. However, despite the flexibility of materials selection and the superior mechanical properties of MMNCs added *ex situ*, the cost of raw powder materials, lack of scalable processing technology, and difficulty incorporating the particles (*e.g.*, particle wetting considerations during addition [14]) remain current barriers to widespread commercialization. As an alternative approach, there has recently been much interest in producing the particles via *in situ* methods, where the particles are directly created in the matrix *via* reactive methods [7, 9, 12, 13]. *In situ* MMNCs are expected to be lower cost, easier to incorporate into melts due to *in situ* formation and exhibit similar mechanical properties as their *ex situ* counterparts. However, despite their promise, many aspects of *in situ* MMNCs are not well understood, including their formation mechanisms and achieving process control over microstructural and mechanical properties. Furthermore, a method of producing MMNCs at a commercial scale has yet to be demonstrated. Consequently, the primary goal of this research was to investigate *in situ* processing methods that may be viable for commercial scale production and understand the corresponding formation mechanisms and the processing-microstructure-property relationships needed to inform rational design of MMNCs.

1.2 Organization and overview of dissertation

The remainder of this dissertation is organized into four primary chapters. Chapter 2 presents an overview of the relvant literature for *in situ* MMNCs. We discuss the advantages and

disadvantages of *ex situ* and *in situ* MMNC processing approaches and provide an overview of some of the existing methods. We also provide a more detailed discussion of the *in situ* MMNC processing methods studied in the succeeding chapters, namely *in situ* gas-liquid reaction (ISGR), self-propagating high-temperature synthesis (SHS) and flux-assisted reaction synthesis. Chapter 2 also covers strengthening mechanisms and microstructure-mechanical property relationships for MMNCs, for the purposes of identifying reinforcement and microstructural characteristics of interest for tuning *via* processing parameters.

In Chapter 3, experimental processing-property relationships of *in situ* MMNCs processed *via* ISGR (Al-AlN) and SHS (Al-TiC) methods. The work in this chapter was conducted as part of a project under the Lightweight Innovations for Tomorrow (LIFT) Institute (Detroit, MI) and performed in close collaboration with Worcester Polytechnic Insitute (Worcester, MA), the Ohio State University (Columbus, OH), Eck Industries (Manitowoc, WI), and the North American Die Casting Association (NADCA) (Arlington Heights, IL). The primary goal of the LIFT project was to investigate the potential for ISGR and SHS processing methods to be scaled-up, and we present results on both lab-scale and commercial pilot-scale material production. Preliminary results suggest that SHS is a promising route for producing commercial pilot-scale quantities of material with both desirable reinforcement characteristics and enhanced mechanical properties.

In Chapter 4, a more detailed investigation into understanding the processing-property relationships of SHS Al-TiC MMNCs specifically is presented. We propose a set of TiC reaction pathways and formation mechanisms by combining 2D and 3D microstructural observations with a thermodynamics-based analysis. To understand the link between processing parameters, *in situ* particle reaction pathways, and final microstructural signatures, we demonstrate an approach combining quantitative microstructural analysis with canonical correlation analysis to identify dominant processing parameters tied to the final SHS microstructures.

In Chapter 5, we summarize the findings of this dissertation and provide some suggestions for future work based on our findings in Chapter 3 and Chapter 4. We also discuss some preliminary experiments on alternative MMNC processing methods (*i.e.*, flux-assisted reaction synthesis), a promising approach that leverages a low bulk processing temperature reaction pathway identified as part of the study in Chapter 4.

CHAPTER 2
Background

2.1 Production and processing of metal matrix nanocomposites

2.1.1 In situ versus ex situ processing methods

MMNCs have been successfully produced by a variety of different methods, which broadly can be separated into *ex situ* and *in situ* processes. *Ex situ* processing methods involve the insertion or dispersion of reinforcement particle powders into the Al matrix (either in the solid state or liquid state). Several examples of solid-state *ex situ* processing methods include: powder metallurgy and mechanical alloying [9, 15]. Several examples of liquid state processes include: microwave sintering, stir casting, melt infiltration, ultrasonic-assisted cavitation, disintegrated melt deposition (DMD), and high pressure die casting (See Table 2.1 for a summary of processing methods) [9, 15]. However, there are several drawbacks to using *ex situ* production methods, such as poor wettability of the ceramic nanoparticles and the melt during conventional casting processes [13, 14]. Due to the high surface energy/poor wetting between the particles and melt, particles will tend to agglomerate and cluster, which is detrimental to the overall mechanical properties of MMNCs [12, 16, 17]. These wetting issues make dispersion of *ex situ* MMNCs a challenge and can result in the rejection of nanoparticles by the melt front during solidification, which leads to agglomeration and interdendritic particle trapping [17, 18, 19, 20]. In addition to issues with wetting and agglomeration, the mechanical properties of *ex situ* MMNCs are also strongly affected by contamination and oxidization of the nanoparticle precursor powders [9], which can lead to porosity in the final product [13], as well as cracking and de-bonding of particle/matrix interfaces [9, 12, 21, 22]. Furthermore, *ex situ* processing methods may not be economically viable, as the high cost of raw materials and multiple processing steps and limited scalability of some methods may limit their usage [15]. Thus, alternative processing methods are necessary for producing MMNCs with superior mechanical properties, scalability, and economic benefit.

Alternatively, *in situ* MMNC processing methods involve the creation of the reinforcement particles or second phases directly in the Al melt during production, typically by chemical reaction

(*e.g.*, solid-solid, liquid-liquid, solid-liquid, or gas-liquid) or morphological methods (*e.g.*, solidification or microstructural deformation). Several examples of *in situ* chemical reaction processing methods include: mechanochemical synthesis, reaction milling (RM), friction stir processing, self-propagating high-temperature synthesis (SHS), exothermic dispersion (XD), flux-assisted reaction, MixAlloy™ (mixture of two molten alloys), and *in situ* gas-liquid reaction (ISGR) [13, 15, 23]. On the other hand, morphological *in situ* processing methods involve the creation of particles *via* non-reactive methods, such as by breaking large second phases into smaller particles through severe plastic deformation or the formation of metastable precipitates through rapid solidification (See Table 1.1 for a summary of processing methods) [13, 15]. *In situ* processing methods offer several advantages over *ex situ* methods, such as the potential for single stage MMNC processing, which leads to more cost effective and less complex, scalable processes [23]. Furthermore, *in situ* MMNCs have the advantage of particles that are thermodynamically stable in the matrix and free of contaminants, leading to a stronger interfacial bond with less degradation at high temperature applications; both of which translate to stronger mechanical properties as compared with *ex situ* MMNCs [12, 15, 19, 24, 25, 26, 27]. Additionally, the particles formed in master alloys by *in situ* methods are often more homogeneously dispersed than those formed by *ex situ* methods [24, 28]. Thus, *in situ* processing of MMNCs is attractive as a method of producing low cost and high strength material.

Table 2.1 Summary of selected *ex situ* and *in situ* metal matrix nanocomposite processing methods. More detailed descriptions of the individual processing methods are available in [13, 15].

Ex situ processing methods	Solid-state process	Powder metallurgy Mechanical alloying Microwave sintering
	Liquid-state process	Stir casting Melt infiltration Ultrasonic-assisted dispersion/cavitation Disintegrated melt deposition (DMD) High pressure die-casting
In situ processing methods	Solid-solid process	Mechanochemical synthesis Reaction milling (RM) Friction stir processing (FSP)
	Solid-liquid process	Self-propagating high-temperature synthesis (SHS) Exothermic dispersion (XD) Flux-assisted reaction synthesis
	Liquid-liquid process	MixAlloy™ (mixing molten alloys)
	Gas-liquid process	*In situ* gas-liquid reaction (ISGR)
	Morphological process	Rapid solidification Severe plastic deformation

More in depth summaries of the various processing methods outlined above are available in [9], [13], and [15]. However, of the various *in situ* and *ex situ* production methods, three are of particular interest for investigation in this thesis: *in situ* gas-liquid reaction (ISGR), *in situ* self-propagating high-temperature synthesis (SHS), and flux-assisted reaction synthesis. The focus on ISGR and SHS is based upon the fact that a large portion of this work was conducted as part of a project under the Lightweight Innovations for Tomorrow (LIFT) Institute (Detroit, MI), where they were identified as two of the most promising *in situ* methods for commercial scale-up (more details available in Chapter 3). The focus on flux-assisted reaction is based on its identification as a promising processing route stemming from the results of the LIFT project and recent results from Professor Xiaochun Li's group at the University of California – Los Angeles (more details available in Chapter 5). A brief description of these processing methods is outlined below.

2.1.2 In-situ gas-liquid reaction (ISGR)

In the ISGR process, nanoparticles are formed through a gas-liquid reaction mechanism, typically accomplished through the injection of gas into a molten metal alloy *via* a rotating impeller

mechanism [7, 13, 29, 30, 31]. The gaseous species (*e.g.*, N_2, NH_3, CH_4) bubbles react with the surrounding melt and break off to form a dispersion of thermodynamically stable ceramic particles (*e.g.,* AlN, TiC). Thus, the ISGR process requires careful control of the gas injection and melt parameters to tune the morphological characteristics of the particles and dispersion. Although the chemical composition of the particles is partially restricted by the compositions of the injected gas and metal melt, MMNCs generated via the ISGR process can also be created in the form of a master alloy and then further diluted into other Al-based alloys to allow for more flexibility in materials systems. The ISGR method has been used successfully to form MMNCs with a variety of different material combinations, including: Al-AlN [13, 29], Al-TiC [7, 27, 30], Al-TiN [26], and Fe-TiN [32]. A schematic depicting the ISGR process and setup is shown in Figure 2.1.

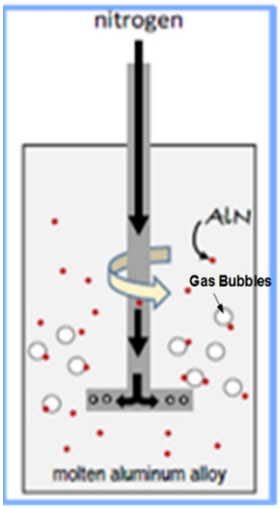

Figure 2.1. Schematic of the *in situ* gas-liquid reaction (ISGR) process. Adapted from [13].

2.1.3 Self-propagating high-temperature synthesis (SHS)

In the SHS process, nanoparticles are formed through solid-liquid and/or solid-solid reaction pathways when a reaction between elemental powders (typically a compacted pellet) is initiated *via* a high temperature source (*e.g.*, addition to a molten melt or spark ignition) or high-energy mechanical activation (*e.g.*, ball milling) [31, 33, 34, 35, 36, 37]. Under ignition conditions, a highly exothermic combustion reaction occurs, which in turn propagates through the powders and leads to the formation of compound materials from the elemental constituents. As an added advantage in the cases of ignition *via* a molten melt, the particles are thought to be somewhat dispersed by the explosive reaction propagation prior to solidification [38, 39, 40]. The SHS

process a large amount of flexibility as the reinforcement compounds are dependent only on the elemental powder chemistry when pure Al melts are used. Consequently, this processing technique has been demonstrated for a wide variety of material systems including: Al-TiC [36, 37, 38, 39], Al-TiB_2 [41], Mg-TiC [42], Cu-TiC [43], Ni-Ti shape memory alloys [44], and Cu_2Se thermoelectrics [45]. A schematic depicting the SHS process and setup is shown in Figure 2.2.

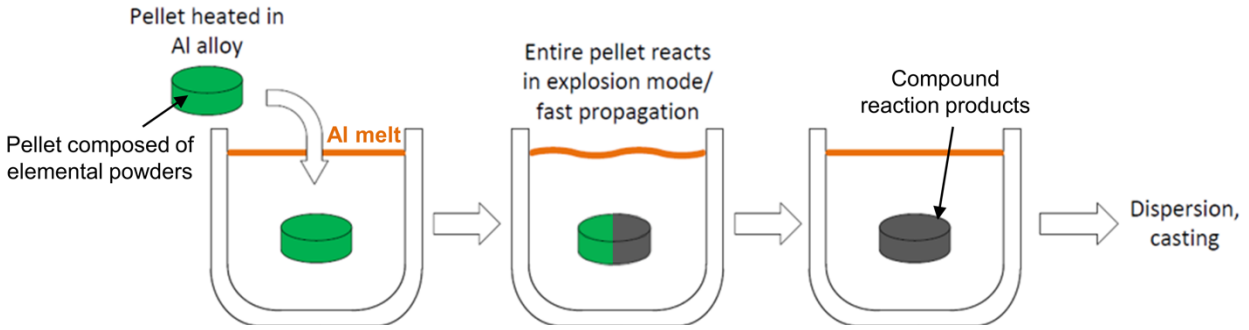

Figure 2.2. Schematic of the self-propagating high-temperature synthesis (SHS) process. Adapted from [31].

2.1.4 Flux-assisted reaction synthesis

Flux-assisted processing methods have been widely used in metallurgy as an *ex situ* method of particle incorporation as it can breakdown the oxide on the melt surface and enhance particle wetting [46, 47, 48]. However, careful choice of flux and elemental powder additives allows for flux-assisted reaction and nanoparticle creation directly in the melt [49, 50, 51, 52]. In flux-assisted reaction synthesis, a molten salt-based flux is blended with elemental powders and added to a melt, where the flux breaks down due to the high temperatures and reaction with surface oxides. The flux decomposition subsequently releases solutal atoms that can either react directly with the melt or the other elemental powders. Flux-assisted processing is promising for its potential scalability, but the composition of the manufactured particles is somewhat limited by the flux and elemental powder chemistries. Previous studies have typically utilized K_2TiF_6 or KBF_4 fluxes to produce composites, including Al-TiC [49, 50, 53, 54], Al-TiB_2 [51, 55], Al-Al_3Ti [56], and Al-AlB_2 [52]. A schematic depicting flux-assisted reaction synthesis is shown in Figure 2.3.

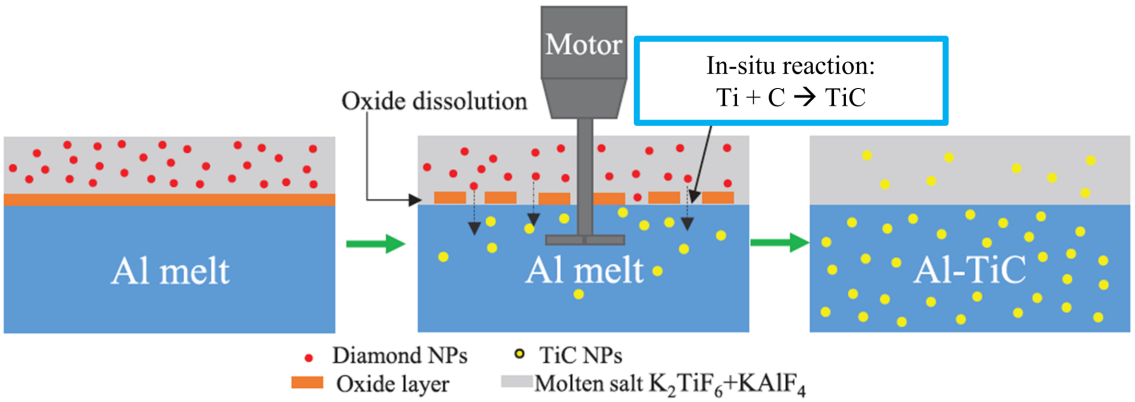

Figure 2.3. Schematic of the flux-assisted reaction synthesis process. Adapted from [49].

2.2 Mechanical property-microstructure relationships in metal matrix nanocomposites

In order to better inform MMNC processing approaches, it is necessary to first understand the microstructure-mechanical property relationships. Knowledge of these relationships can then be used to target specific desirable particle and microstructure characteristics and guide materials processing.

2.2.1 Metal matrix nanocomposite strengthening theory

In MMNCs, the mechanical property enhancement comes from strengthening contributions provided by the reinforcement, either in the form of direct (*i.e.*, matrix-to-particle load transfer) or indirect (*i.e.*, increased dislocation density stemming from particle/matrix thermal mismatch during solidification or Orowan strengthening) mechanisms [25]. Consequently, the overall properties of the composites are the sum of these strengthening contributions, where the magnitude of individual contributions vary depending on the reinforcement and microstructural characteristics of the material. The various strengthening mechanisms have been discussed at length in the literature [9, 12, 57, 58, 59, 60, 61, 62]. For the purposes of this thesis, a summary of the proposed mechanisms is outlined below using Ceschini *et. al.* [9] as a basis, where $\Delta \sigma_i$ denotes the increase in composite yield strength attributed to each individual mechanism.

- <u>*Load transfer/Load bearing*</u>: Load transfer is a form of direct strengthening in which an applied external load is transferred from the softer matrix to the to the higher stiffness reinforcement particles. The effectiveness of load transfer is highly dependent on both the

aspect ratio and size of the particles. The strengthening provided by nanoparticle load transfer is well described by a modified shear lag model [63] as,

$$\Delta\sigma_{Load\ Transfer} = \nu_p \sigma_m \left[\frac{(l+t)A}{4l}\right], \tag{2.1}$$

where υ_p is the total volume fraction of particles, σ_m is the yield strength of the matrix, A is the particle aspect ratio, and l and t are the width and height of the particles respectively [9, 12, 23]. For the case of spherical particles, Eqn. (2.1) reduces to Eqn. (2.2) [12],

$$\Delta\sigma_{Load\ Transfer} = \frac{1}{2}\nu_p \sigma_m. \tag{2.2}$$

- *Enhanced dislocation density (Coefficient of thermal expansion mismatch and elastic modulus mismatch)*: The density of dislocations in the material will have a significant effect on its mechanical properties as they impede dislocation motion. In coefficient of thermal expansion (CTE) mismatch, large thermal stresses occur at the matrix/nanoparticle interface during solidification. In elastic modulus (EM) mismatch, stresses become more localized around the matrix/nanoparticle interfaces under applied loads. In both cases, the additional localized stresses induce plastic deformation and thus create an increased density of dislocations around the interface, effectively reinforcing the microstructure [9, 12, 59, 64]. The enhanced dislocation densities owing to both CTE and EM mismatch are given by Eqn. (2.3) and (2.4) respectively,

$$\rho_{CTE} = \frac{A\upsilon_p \Delta\alpha \Delta T}{b d_p (1-\upsilon_p)} \tag{2.3}$$

$$\rho_{EM} = \frac{6\upsilon_p}{\pi d_p^3}\varepsilon. \tag{2.4}$$

Where A is a geometric factor between 10 and 12 depending on particle shape and geometry, b is the Burgers vector, v_p is the volume fraction of the reinforcing particles, d_p is the diameter of the reinforcing particles, ΔT is the temperature difference between the MMNC processing and tensile test temperatures, $\Delta\alpha$ is the difference in CTEs between the matrix and particles, and ε is the bulk material strain. The combined strengthening contribution of CTE and EM mismatch can then be described by,

$$\Delta\sigma_{CTE+EM} = M\beta G_m b\sqrt{\rho_{CTE}} + \sqrt{3}\alpha G_m b\sqrt{\rho_{EM}}, \tag{2.5}$$

where M is the Taylor factor (~1), β is a strengthening coefficient (usually ~1.25), α is a strengthening coefficient (usually ~0.5), G_m is the shear modulus of the matrix, and b is the Burgers vector [9, 12, 60].

- *Orowan strengthening/looping*: Orowan strengthening (or Orowan looping) is the phenomenon in which dislocation movements become pinned by closely spaced, hard reinforcement particles [65]. Orowan strengthening is particularly relevant for nanoparticles and can become the dominant mechanism for small particle diameters and low interparticle distances [66, 67]. However, the effectiveness of this mechanism is strongly dependent on the particle spacing uniformity and dispersion homogeneity [68, 69]. The strengthening effect of the Orowan mechanism can be described by,

$$\Delta\sigma_{Orowan} = \frac{0.13 G_m b}{\lambda} \ln\left(\frac{d_p}{2b}\right), \tag{2.6}$$

where G_m is the shear modulus of the matrix, b is the Burgers vector, d_p is the diameter of the reinforcement particles, and λ is the interparticle spacing. The interparticle spacing can be expressed as,

$$\lambda \approx d_p \left[\left(\frac{1}{2v_p}\right)^{1/3} - 1\right], \tag{2.7}$$

where v_p is the volume fraction of the particles.

- *Grain refinement/Hall-Petch effect*: In addition to strengthening *via* load transfer or dislocation-mediated interactions, the addition of nanoparticles can also induce significant grain refinement in MMNCs [70]. In general, grain size has a significant effect on the mechanical properties of alloys, as grain boundaries can act as barriers to dislocation motion [65]. The subsequent strength enhancement as a function of grain size is well described by Hall-Petch theory, given by,

$$\Delta\sigma_{Hall-Petch} = K {d_m}^{-1/2}, \tag{2.8}$$

where K is the Hall-Petch co-efficient and d_m is the average grain diameter. Nanoparticles may act as grain nucleation sites during solidification, leading to a refined grain structure in the final MMNC [70, 71, 72, 73, 74]. Additionally, the nanoparticles are able to interact with grain boundaries, thereby restricting grain growth and coarsening during high

temperature plastic deformation and recrystallization [9, 12, 59, 75, 76]. This phenomenon is known as the Zener pinning effect and the effective resultant grain size is given by,

$$d_m = \frac{4\alpha d_p}{3\upsilon_p}, \tag{2.9}$$

where α is a proportionality constant, d_p is the particle diameter, and υ_p is the volume fraction of the particles.

Ultimately, the total enhanced yield strength of the MMNCs can be estimated based on the sum of the relative contributions of each strengthening mechanism and several unified models have been proposed [57, 58, 60, 61, 67]. However, the approach taken by Santay-Zadeh [60] specifically considers reinforcement particle size (*e.g.,* micro- versus nano-particles) and combines several different models. The total strength enhancement using this approach assumes linear independence of each mechanism and is given by,

$$\sigma_{y,MMNC} = \sigma_m + \sqrt{(\Delta\sigma_{LT})^2 + (\Delta\sigma_{H-P})^2 + (\Delta\sigma_{CTE+EM})^2 + (\Delta\sigma_{Or})^2}, \tag{2.10}$$

where $\sigma_{y,MMNC}$ is the enhanced yield strength of the nanocomposite, σ_m is the yield strength of the matrix, and $\Delta\sigma_i$ is the contribution of the respective strengthening mechanism. Using this model, Sanaty-Zadeh found that the relative contributions of each strengthening mechanism varied drastically with particle size and that nanoparticles may be particularly important for enhanced dislocation density, grain refinement, and Orowan strengthening contributions (See Figure 2.4). Consequently, the use of smaller particles may be advantageous for MMNC material design.

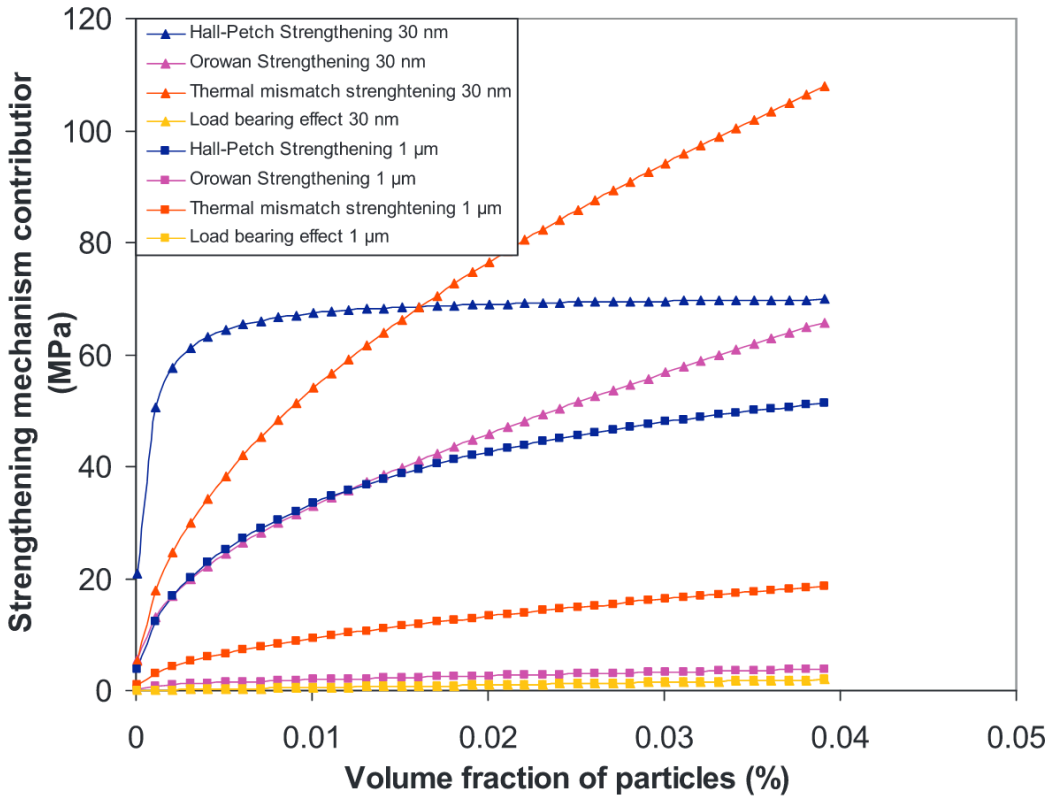

Figure 2.4. Strengthening mechanism contributions as a function of volume fraction considering both micro- and nano-particles using Eqn. (2.10). Adapted from [60].

From the strengthening theory outlined in this section, it is clear that it is difficult to separate out individual mechanism contributions. However, the equations can be used to identify key particle characteristics expected to inform bulk MMNC mechanical properties. In particular, volume fraction and particle diameter are re-occurring terms in the strengthening equations, which we define as:

- *Volume fraction (or weight fraction) of reinforcement particles*: The number of particles incorporated into the MMNCs, or total volume of particles relative to the matrix volume. The volume fraction, v_p, is expected to affect load transfer, enhanced dislocation density, and Orowan strengthening mechanisms as well as contribute to grain refinement.
- *Reinforcement particle size*: The size distribution (usually in nanometer or micrometer length scales) of the particles incorporated into the MMNCs. The particle diameter, d_p, is expected to affect load transfer, enhanced dislocation density, and Orowan strengthening mechanisms as well as contribute to grain refinement.

2.2.2 Influence of particle volume fraction

Consistent with the theory, the volume fraction of reinforcement particles is experimentally observed to have a significant effect on the improvement of MMNC properties [12, 24, 25]. For example, Borgonovo *et al*. [77] observed a significant increase in the ultimate tensile strength (UTS) and yield strength (YS) at room and elevated (300 ºC) temperatures for relatively low amounts of AlN particles added to cast A356 alloy (See Figure 2.5(a)). Increases in the UTS and YS as a function of particle volume fraction have also been observed in other *in situ* Al-AlN studies [78, 79], *in situ* Al-TiC [80, 81, 82], and *in situ* Al-Al_2O_3 [83], as well as *ex situ* materials systems such as AlCuMg-SiC [25], Al-Al_2O_3 [84], Al-Si_3N_4 [85], Al-TiB_2 [86], and AlCu-TiC [87] (See Figure 2.5(b)). In addition to improved tensile properties, increases in material hardness have also been observed to be directly correlated with increasing volume fractions of reinforcement particles [77, 80, 88].

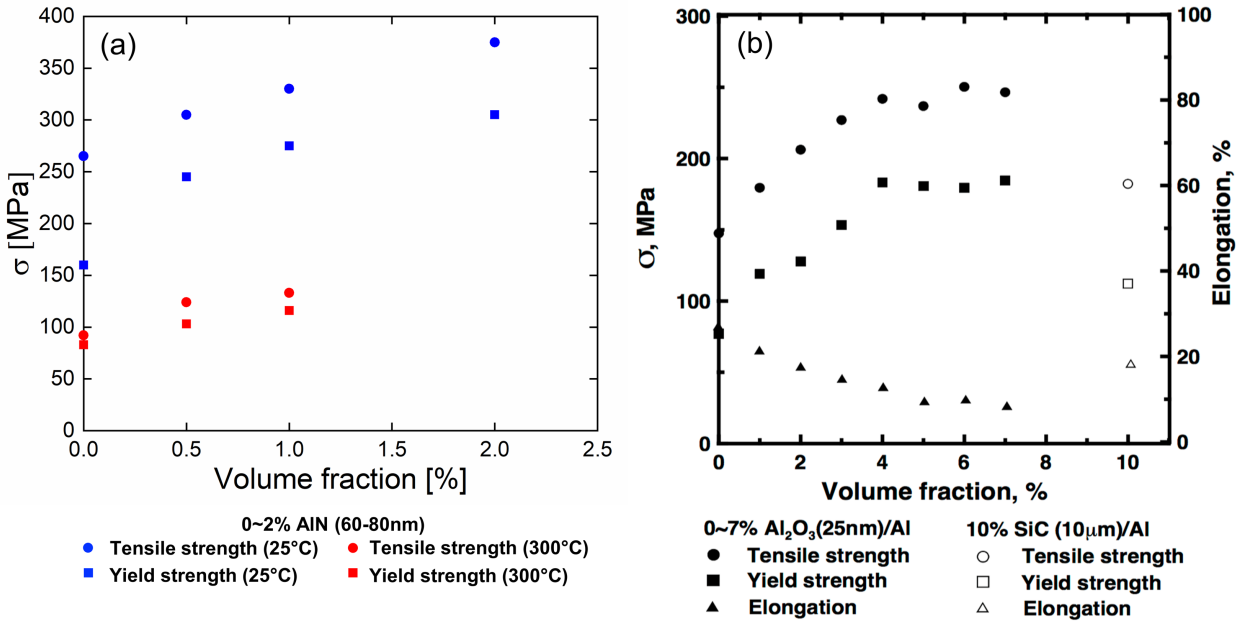

Figure 2.5. (a) Tensile and yield strength of A356 versus volume fraction of AlN particles, measured at room temperature and 300 ºC. Adapted from [13]. (b) Tensile strength, yield strength, and elongation of Al versus volume fraction of Al_2O_3 and SiC particles measured at room temperature. Adapted from [25].

Despite a general increase in tensile properties, higher amounts of particulate reinforcement are observed to decrease MMNC ductility, presumably owing to increased microplasticity (localized and inhomogeneous deformation) in the matrix [24, 25, 79, 77, 89, 90].

Decreases in ductility with increasing volume percentage are hypothesized to be caused by an increasing number of particle/matrix interfaces acting as preferential sites for crack initiation *via* particle/matrix debonding or particle cracking [91, 92]. This hypothesis may also be in good agreement with the observed inverse relationship between fracture toughness and ductility in MMNCs [93, 94, 95]. However, the opposite trend has also been reported by Tian *et. al.* [96] and Khdair *et. al.* [97], where increasing volume fractions of particles were observed to improve ductility. In these cases, it is likely that increases in ductility are due to particle induced grain refinement, where particles act as heterogeneous grain nucleation sites [70, 98, 99]. However, the degree of grain refinement by particulate inoculants is not only dependent on the amount of particles, but also on the overall refining efficiency (*e.g.,* number of activated refining particles) of the particle/matrix system, which may explain why ductility improvements are not always observed [71, 72, 100, 101, 102].

2.2.3 Influence of particle size

Particle reinforcement size is another key parameter for tuning mechanical properties of MMNCs in conjunction with the volume fraction. Smaller particles can be used to overcome some of the drawbacks associated with high reinforcement volume fractions in the matrix and increased tensile properties as a function of decreasing particle size (with a constant volume fraction) have been reported for micrometer-sized particles in SiC-Al based systems [25, 89, 103, 104] and nano-sized particles in Al_2O_3-Mg based systems [66] (See Figure 2.6). Presumably, for equivalent volume fractions as larger particle MMNCs, the use of smaller particles increases the available matrix/particle contact area, thus increasing interfacial dislocation density and improving particle-matrix load transfer [95, 103]. Additionally, smaller particles may contribute further strengthening improvements *via* Orowan strengthening as particles approach the sub-500 nm regime [105].

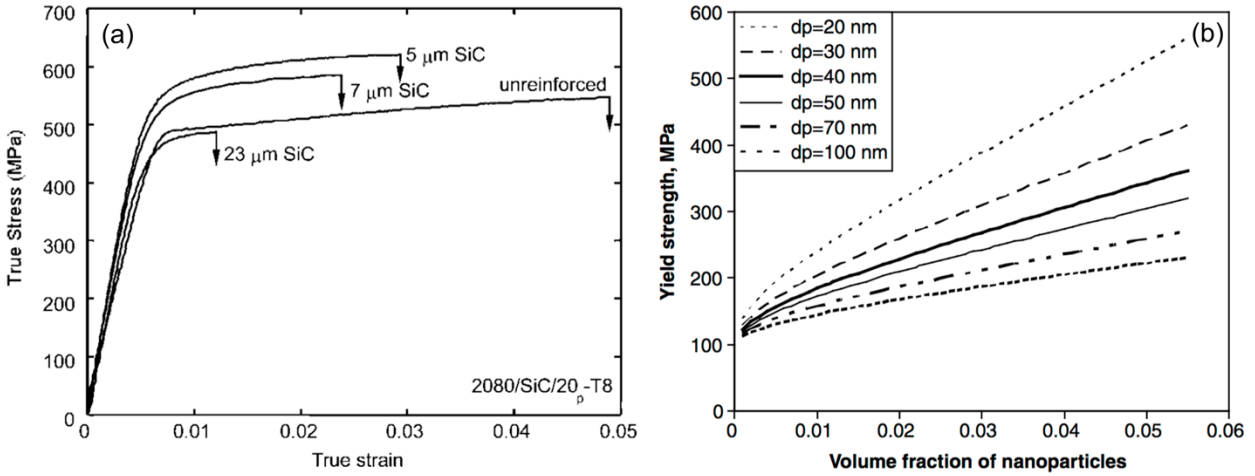

Figure 2.6. (a) True stress-strain curves for 2080 Al alloy reinforced 20 vol% SiC particles of various micro-scale diameters. Adapted from [25]. Yield strength of Mg as a function of volume fraction fraction of Al_2O_3 particles of various nano-scale diameters. Adapted from [66].

Previous studies on the effect of particle size on material ductility have come to conflicting conclusions, with increases in ductility [89, 106], decreases in ductility [95], and relatively little change [77] being observed. Similar to the effect of reinforcement volume percentage and ductility, some of the discrepancies may be due to the effect of particle induced grain refinement [70]. In general, the grain size has been observed to be reduced as particle size decreases to the few micrometers regime [107, 108]. Sub-micrometer particles have been reported to improve grain refinement even further in small amounts (*e.g.,* 1.5 vol%) [109], however a decrease in grain refining abilities have also been observed as particle sizes reach sub-micrometer scales [102, 108]. These conflicting observations of grain refinement as a function of particle size are presumably due the higher susceptibility of nanoparticles to agglomeration, as well as differences in overall refining efficiency of the different material systems [70, 72, 100, 101, 102].

2.2.4 Influence of particle dispersion and particle/matrix interface quality

Although particle volume fraction and diameter are expected to have a direct effect on the strengthening mechanism equations in Section 2.2.1, other factors such as particle dispersion can also play a significant role. Dispersion refers to the spatial distribution of the particles in the MMNCs and is also related to the degree of agglomeration or clustering and is thought to arise largely due to attractive van der Waals forces that cause clustering [110, 111]. It is expected that the degree of dispersion will affect Orowan strengthening *via* interparticle spacing (Eqn. (1.7)).

However, particle dispersion is also expected to indirectly affect multiple mechanisms, such as altering the local degree of grain refinement and grain size homogeneity [112, 113, 114]. Particles and agglomerates/clusters can be broken up and dispersed *via* various mixing methods, such as mechanical mixing [115, 116] and ultrasonic processing/cavitation [16, 117, 118]. However, the effectiveness of these methods is highly dependent on particle size, agglomerate strength, and mixing processing parameters [119, 120, 121]. Experimental studies have generally observed a link between improved mechanical properties and homogeneous particle dispersions [122, 123, 124, 125], but effective dispersion control remains a challenge for MMNCs [12, 126].

Another factor that is excluded theoretical models, but that may play a significant role in MMNC strengthening, is the particle/matrix interface. In Santay-Zadeh's [60] approach discussed in Section 2.2.1, the direct strengthening load transfer mechanism is hypothesized to be relatively insensitive to particle size and volume fraction. However, the model does not consider the quality or coherency of the particle/matrix interface, which is particularly relevant when considering *in situ* versus *ex situ* MMNCs [24, 127]. In *ex situ* MMNCs the precursor particle contamination and unfavorable interfacial reactions can both lead to interlayer formation that may significantly alter the particle/matrix bond strength *via* generation of additional weakly bonded interfaces [9, 128, 129, 130]. The strength and number of these interfacial bonds is hypothesized to be a major contributor to particle-matrix load transfer efficiency [130, 131, 132, 133, 134] as well as control whether MMNC failure will occur *via* particle/matrix debonding or particle cracking [92, 135, 136]. In some cases, the interfacial reactions can be tuned with post MMNC processing to form desirable interlayers for enhanced load transfer [136, 137]. However, *in situ* MMNCs may be advantageous due to their inherently stable interfaces upon initial creation, which can lead to clean bonding surfaces and improved particle/matrix coherency [24, 79, 138] (See Figure 2.7). However, it is important to consider that the coherency of the interface is also strongly dependent on the particle size. Previous studies have observed loss of interfacial coherency in nano-scale particles and a transition to semi-coherent or incoherent interfaces above a critical particle diameter (dependent on the particle-matrix system) [139, 140, 141, 142]. Consequently, while *in situ* MMNCs are advantageous from a reduced interfacial contamination perspective, decreased particle diameters are also expected to contribute to interface quality and coherency.

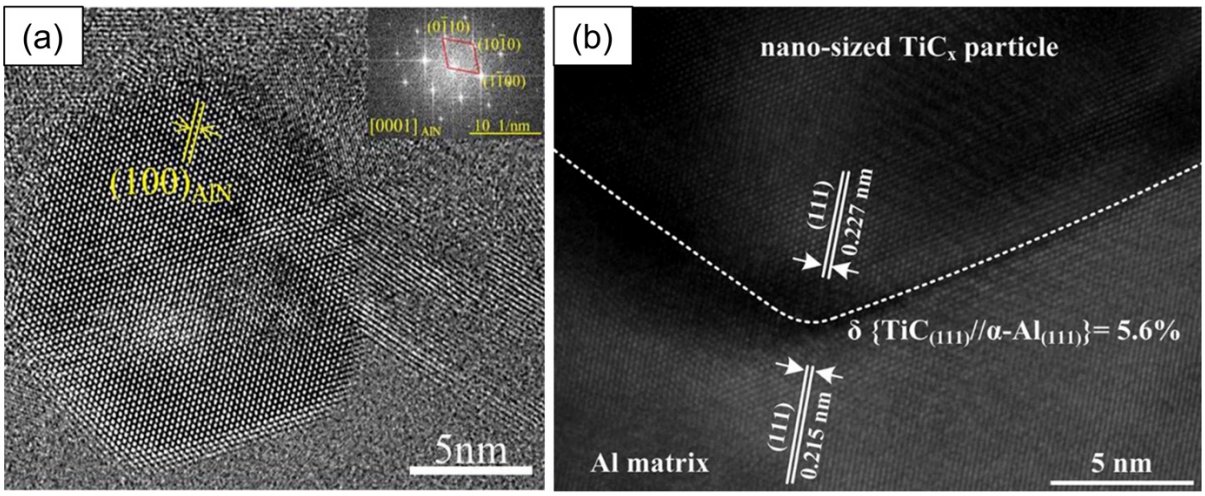

Figure 2.7. (a) Clean interface between AlN particle and Al matrix fabricated *via* a *in situ* high temperature extrusion method. Adapted from [79]. (b) Clean interface between TiC_x and Al-Cu-Mg matrix fabricated *via* a *in situ* combustion synthesis. Adapted from [138].

2.3 Background summary

The theory and experimental literature presented in the previous sections of this chapter indicate that control over the mechanical properties of MMNCs is largely related to the ability to control properties of the particulate reinforcement. Specfically, control over the particle volume fraction, particle diameter, dispersion and agglomeration, and particle/matrix interface are important for enhanced bulk material strengthening. Although a variety of MMNC processing methods exist, *in situ* approaches are particularly promising due to their inherently clean particle/matrix interfaces and particle stability. However, as the particles are created *in situ*, an understanding of the link between processing parameters and control over particle size, volume fraction yield, and dispersion remains an open question. Furthermore, an understanding of these relationships is a critical step in adapting *in situ* MMNC processing to commercial scales, despite their potential as a scalable approach. Consequently, in the following chapters we explore a rational approach to investigating *in situ* MMNC processing-property relationships and informing scale-up processing efforts.

CHAPTER 3

Towards Commercial Scale-Up of *In Situ* Metal Matrix Nanocomposite Production

Note: Portions of the work presented in this chapter have been adapted from C.W. Reese, *et. al.* in *Metallurgical and Materials Transactions A* [143] and, due to the collaborative nature of the LIFT project reflected in this chapter, J. Fedors thesis from Worcester Polytechnic Institute [31].

3.1 Introduction

Al-based metal matrix nanocomposites (MMNCs) are of high interest for a variety of structural applications in the automotive and aerospace industries, owing to the possibility of leveraging the combined mechanical properties of a relatively ductile Al matrix with high strength ceramic reinforcing particles [9, 10]. Typically, MMNCs can be created *via ex situ* or *in situ* methods, where particles are either added to or created directly in the matrix during processing respectively. *In situ* MMNCs have recently been seen as particularly promising due to their potential scalability and the possibility of bypassing issues with high precursor powder costs, precursor contamination, and particle wetting/incorporation plaguing *ex situ* methods [9, 12, 23, 127]. However, despite their promise, a commercial-scale approach to producing *in situ* MMNCs has yet to be demonstrated. Consequently, an investigation of large-scale MMNC processing and the corresponding processing-microstructure-property relationships is needed.

The work performed in this chapter is based upon a larger collaborative project conducted by the Lightweight Innovations for Tomorrow (LIFT) Institute (Detroit, MI), that sought to target the problem of commercial-scale MMNC processing. The overall project objective was to investigate and scale-up *in situ* processing methods for Al-based nanocomposite materials that would be compatible with existing commercial casting (*e.g.*, die- and squeeze-casting) technologies. As discussed in Chapter 2, there is a large breadth of research pertaining to MMNC processing methods, which could not all be evaluated over the course of this project. Consequently, an informed down select was performed by the LIFT project team beforehand and the project scope was set as identifying two *in situ* approaches of interest. The *in situ* methods chosen for this study

were *in situ gas-liquid reaction* (ISGR) [7, 13] and self-propagating high-temperature synthesis (SHS) [33, 34, 35, 36, 37, 38]. The remainder of this chapter will discuss the processing experimental efforts, both lab-scale and commercial-scale, and subsequent microstructural and mechanical properties of MMNCs produced *via* ISGR and SHS. Finally, we discuss conclusions about the viability of each process for meeting the project goals set forth by the LIFT.

Due to the heavily collaborative nature of this project, the work discussed in this chapter was performed in close conjunction with Worcester Polytechnic Institute (WPI) (Worcester, MA) and Eck Industries (Manitowoc, WI). WPI and Eck were heavily involved in the materials processing efforts, while the work described here at the University of Michigan was focused on the microstructural characterization and mechanical property evaluation used to inform processing efforts. The processing side of the experiments is briefly summarized in this chapter for completeness, but a complimentary document containing more detail regarding ISGR and SHS processing method development is available in J. Fedors's thesis from WPI [31].

3.2 *In situ* gas-liquid reaction (ISGR): Laboratory-scale

3.2.1 ISGR master alloys: Experimental methods

In situ Al-AlN master alloy composites were processed at WPI (Worcester, MA), using a process initially developed by C. Borgonovo [13] and refined by I. Añza [7] and J. Fedors [31]. It is important to note that several iterations of the lab-scale ISGR process were conducted, however many were unsuccessful due to equipment and hardware malfunctions (rather than due to processing conditions necessarily). Thus, for the purposes of this study, we focus on the experimental methods that led to the "best" laboratory-scale ISGR sample.

To create Al-AlN master alloys, approximately 1 kg equal parts high purity Al (99.99% purity) and Al-5wt%Li were melted together in a SiC coated graphite crucible at a temperature of 1323 K (1050 °C) under protective Ar atmosphere due to the high oxygen sensitivity of the Al-Li melt and ISGR process [13]. A 6-blade ceramic impeller rotating at 450 RPM was then lowered into the melt and Ar gas was flowed through for 5 min to purge the system and ensure homogenization. After purging, high purity N_2 was injected through the rotating impeller at a flow rate of 1000 sccm/min for 90 min. The N_2 gas was fed through a series of O_2 traps prior to reaching the impeller, to further ensure an oxygen-free environment. After nitridation, the impeller was purged again with Ar before removal from the melt, the furnace was shut off, and the master alloy

was allowed to solidify inside the furnace under continual Ar flow. A schematic of the ISGR setup used to create master alloys at WPI is shown in Figure 3.1. A summary of the processing conditions used to process small-scale Al-AlN master alloys is shown in Table 3.1.

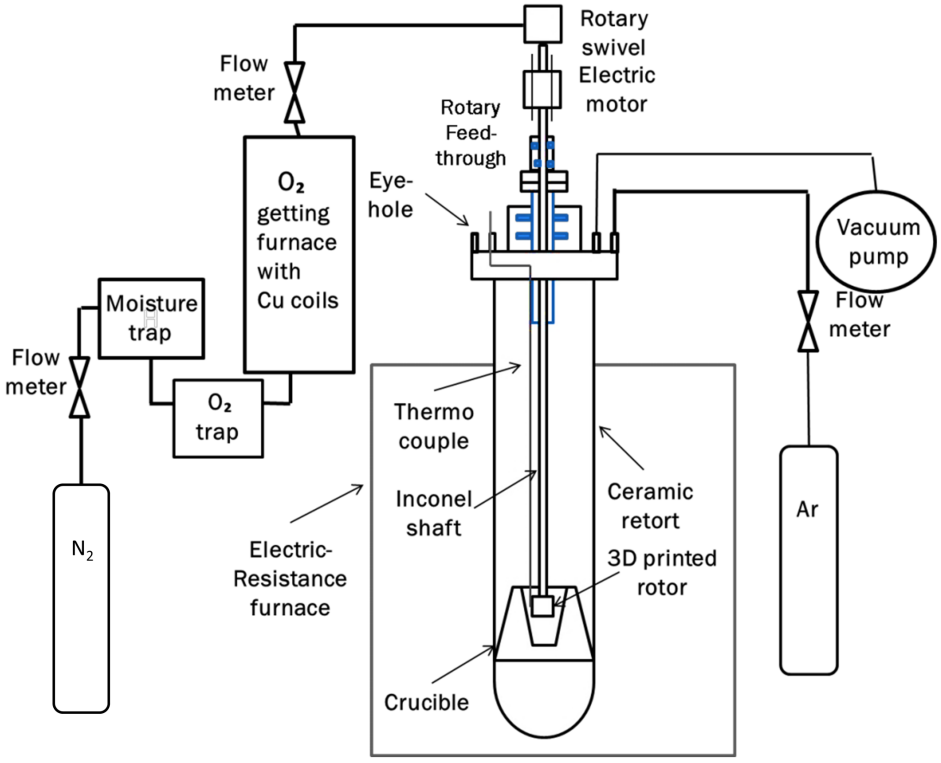

Figure 3.1. Schematic of the *in situ* gas-liquid reaction (ISGR) setup developed at Worcester Polytechnic Institute. In the ISGR process, purified nitrogen-bearing gas flows through a rotating impeller and reacts with an Al-based melt to form AlN. Setup schematic adapted from [13].

Table 3.1. Summary of processing parameters used to create the best Al-AlN small-scale master alloys *via* ISGR.

Sample ID	N_2 flow rate [sccm/min]	Impeller speed [RPM]	Nitridation time [min]	Process temperature [°C]
ISGR-1	1000	450	90	1050

3.2.2 ISGR master alloys: Characterization and data processing methods

Metallographic specimens were prepared from Al-AlN master alloys by sectioning as-cast ingots and cold mounting in non-conductive epoxy (Mager Scientific). Several ingot locations were prepared from each master alloy batch to check for microstructure homogeneity. Mounted

samples were ground and polished using an ATM Saphir 530 dual wheel auto-grinder/polisher. Mounted samples were wet-ground using 320, 400, 600, and 1200 grit SiC papers (Pace Technologies), with contra head/platter rotation at 150 RPM and 15 N of downward force per sample. Samples were polished to a "mirror finish" using 9 μm, 3 μm, and 1 μm polycrystalline diamond suspensions (Mager Scientific), with complimentary head/platter rotation at 150 RPM and 15 N of downward force per sample. After polishing, samples were bath sonicated for 30 s in ethanol to remove polishing particles embedded in the surface. As a final preparation step for Al-AlN samples, polished samples were etched for 10-15 s using a solution of 10vol% NaOH and de-ionized (DI) water, followed by DI water rinsing and immediate submersion in a 65 °C stirred DI water bath for 1 min.

Scanning electron microscopy (SEM) was used for characterization of the MMNC microstructure and particle characteristics. SEM was performed using either a Tescan MIRA3 field emission gun (FEG) SEM typically operating at an accelerating voltage of 10 kV and a beam intensity of 10 – 12, or a FEI Nova 200 Nanolab SEM/FIB operating at an accelerating voltage of 10 kV and 0.54 – 1.6 nA (both microscopes were operating in secondary electron (SE) imaging mode). An EDAX energy dispersive spectroscopy (EDS) system integrated with both SEMs was used for localized chemical identification of particles and secondary phase precipitates.

X-ray diffraction (XRD) was used as a complimentary technique to identify the presence of AlN in the bulk. XRD scans were taken using a Rigaku Rotating Anode X-ray Diffractometer operating at 100 kV and 40 mA. Due to the height limitations of the Rigaku sample state, the metallographic epoxy mounting step was omitted for XRD samples. Instead, new specimens < 10 mm in height were sectioned and hand-ground with 400, 600, and 1200 grit SiC grinding paper (a level surface is more important than the specific surface finish). Due to the small volume of AlN present in the master alloys, scanning parameters of 1.5 °/min scan rate and a 0.2° step size were used in order to ensure sufficient count collection.

Volume fractions and dimensions of AlN particles produced *via* ISGR were estimated based on SEM micrographs using ImageJ (version 1.49) image processing software. Particle length and width dimensions were manually measured using the straight-line tool and used to identify an approximately range of values. To calculate particle volume fractions, SEM images were adjusted to maximize contrast and then segmented by using the auto-thresholding tool to remove the matrix

background. Volume fractions were taken to be the total area of the remaining area elements after thresholding divided by the total micrograph area.

3.2.3 ISGR master alloys: Microstructural characterization and discussion

The ISGR master alloy microstructures generally consisted of elongated and faceted micrometer-scale AlN particles embedded in the Al matrix. The matrix itself appeared fairly porous, with a large amount of surface cracking present. A representative SEM micrograph of the ISGR samples is shown in Figure 3.2(a) and a representative XRD spectra confirming the presence of AlN in the bulk is shown in Figure 3.2(b). In Figure 3.2(c), a higher magnification image of the particles (left) and corresponding EDS spectra (right) are shown, suggesting a particle chemistry corresponding to AlN. Typical particle dimensions were approximately 1 μm long and <500 nm wide. Particles commonly appeared to be agglomerated and roughly aligned "end-to-end" in a pseudo-chain configuration, possibly suggestive of fracturing of long particles. Volume fractions of the small master alloys were estimated to be approximately 2-3 vol% AlN and observed to be relatively homogeneous between multiple ingot locations.

The presence of elongated AlN particles is generally expected to be undesirable for enhanced MMNC mechanical properties, as previous studies have observed them to be strongly dependent on particle shape [135, 144, 145]. Interestingly, the results of the present small-scale ISGR experiments were unexpected as compared with the previous WPI work that served as the basis for this study. Most notably, the AlN particles in the previous work were equiaxed in shape, even with similar processing parameters [13]. The key differences between processing conditions used in this study and the previous work was the use of a 6-blade impeller (this work [31]) versus a 4-blade impeller (previous work [13]). Unfortunately, due to time constraints and unforeseen experimental setbacks, further explorations of the ISGR processing space using the current lab-scale setup was not possible [31]. However, it is clear that the ISGR process is highly sensitive to slight variations in the processing parameters.

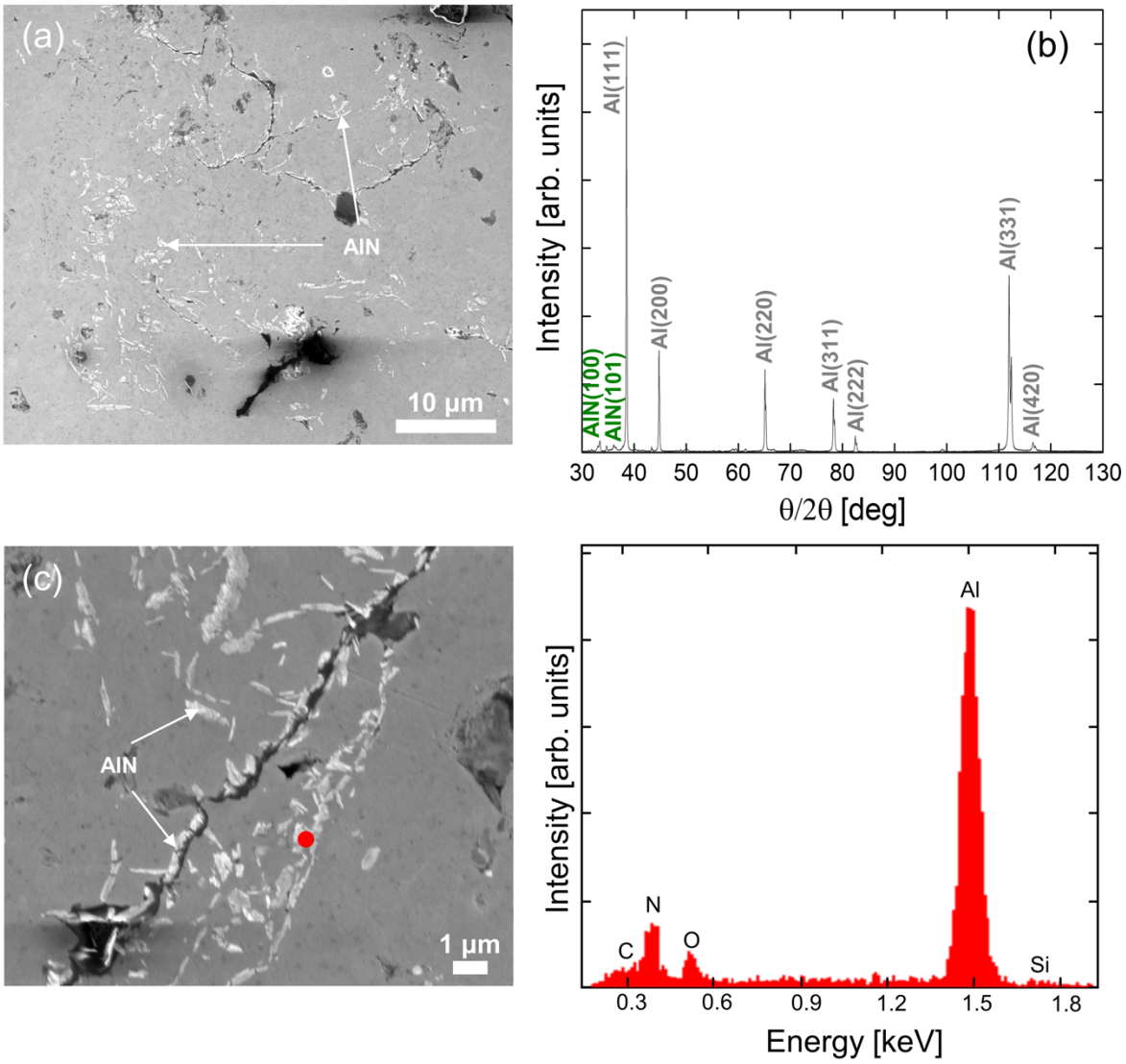

Figure 3.2. (a) SE SEM image of Al-AlN small-scale master alloy showing the presence of elongated AlN particles in Al after processing *via* ISGR. (b) XRD spectra of Al-AlN small-scale master alloy showing the presence of peaks corresponding to AlN. (c) Higher magnification SE SEM image showing the elongated AlN particles in more detail (left). EDS spectra corresponding to the elongated AlN particles (collected from red dot), where the N peak suggests AlN (right).

To better understand the differing particle morphologies, it is useful to consider the proposed formation mechanisms of AlN *via* ISGR. To date, several empirical models have been developed considering direct nitridation of Al melts, which are commonly based on the idea of the two-film model [146, 147, 148]. Originally developed by Zheng *et al*. [148] and based on bubbling N-bearing NH_3 into Al melts for AlN formation, the two-film model proposes that particles form *via* reaction at the gas/liquid melt boundary layer as the bubble travels upwards in the melt. The bubble subsequently bursts, breaking up the AlN reaction layer and dispersing particles outward

(See Figure 3.3). In the context of these proposed formation mechanisms, it is possible that the elongated particle morphologies originate as an AlN layer forms parallel to the bubble/melt interface and then do not break up completely from impeller rotation or bubble collapse. Similar elongated morphologies have been observed for the ISGR process without any stirring action [149]. Consequently, it is likely that the differences in particle morphologies may be related to differences in the impeller geometries, highlighting the necessity of controlling the fluid dynamics of the melt in addition to the nitridation/nitrogen flow parameters [13, 31].

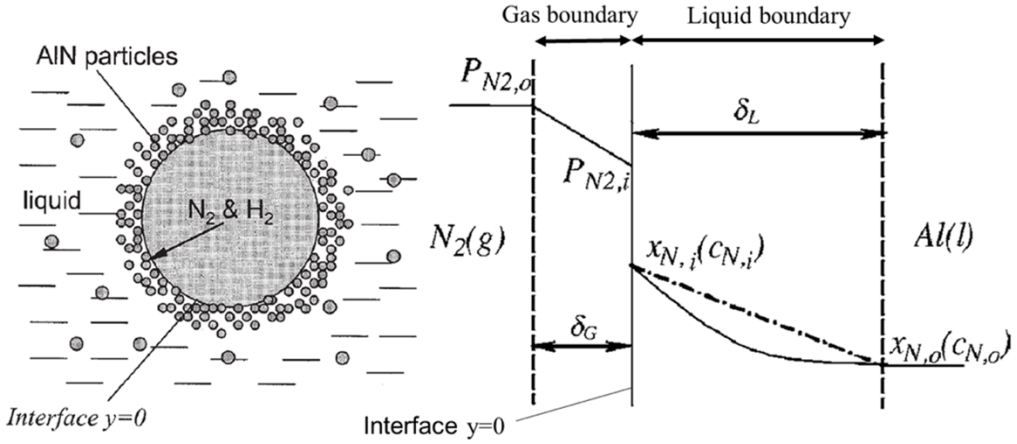

Figure 3.3. Illustration of the two-film model for the formation of AlN particles during direct nitridation of an Al-based melt. δ_G and δ_L are the thickness of the gas and liquid boundary layer respectively, P_{N2} is the partial pressure of N_2, x_N is the concentration of N in the liquid boundary layer. Adapted from [147, 148].

3.3 *In situ* gas-liquid reaction (ISGR): Scale-up approach

3.3.1 Scale-up of ISGR experiments: Experimental methods

Efforts to scale-up the ISGR process involved the design of a custom setup based on the original ISGR equipment (details on the specific design and equipment available in [31]). For large-scale experiments, N_2 flow rate and reaction/processing time were increased to account for the larger melt volume and the impeller design was modified to a 4-blade configuration rotating at 250 RPM to prevent blade breakage observed in the small-scale experiments [31]. To create large-scale master alloys, equal parts high purity Al (99.99% purity) and Al-5wt%Li were melted together at 1313 K (1040 °C), approximately 5 kg each. Subsequently, a 4-blade ceramic impeller rotating at 250 RPM was lowered into the melt and Ar gas was flowed through for 5 min to purge

the system and ensure homogenization. High purity N_2 was subsequently injected through the rotating impeller (after flowing through the O_2 traps) at a flow rate of 4000 sccm/min for 100 – 150 min. After nitridation, the impeller was purged again with Ar before removal from the melt, the furnace was shut off, and the master alloy was allowed to solidify inside the furnace under continual Ar flow to prevent oxidation. A summary of the different process conditions used for large-scale alloy production are shown in Table 3.2.

Table 3.2. Summary of processing parameters used to create Al-AlN large-scale master alloys *via* ISGR.

Sample ID	N_2 flow rate [sccm/min]	Impeller speed [RPM]	Nitridation time [min]	Process temperature, T_{proc} [°C]
ISGR-2	4000	250	150	1040
ISGR-3	4000	250	100	1040

3.3.2 Scale-up of ISGR experiments: Results and discussion

ISGR samples produced *via* the scaled-up setup were prepared for metallography and characterized using the same techniques described in Section 3.2.2. The observed ISGR microstructures in samples produced *via* the large-scale setup contained faceted, anisotropic AlN particles similar to the small-scale master alloys (See Figure 3.4). However, while the particle morphologies were similar, the particles here were generally longer. AlN particle dimensions were approximately 5-10 μm in length and <500 nm wide for both large-scale processing conditions. Similar to the small-scale master alloys, particles commonly appeared to be roughly aligned end-to-end in a pseudo-chain configuration, possibly suggestive of fracturing of long particles. Interestingly, the particle chains in the large-scale batches appear to exhibit some level of curvature, possibly more apparent due to the overall longer particle lengths. As compared with the small-scale master alloys, particle distributions here were relatively inhomogeneous, being largely concentrated in the bottom half of the ingot for both processing conditions. Estimates of particle volume fractions in the bottom half were calculated as 5-6 vol% AlN for the batch processed for 150 min and 2-3 vol% for the batch processed for 100 min. However, these are likely overestimates of the overall volume fraction due to ingot inhomogeneity.

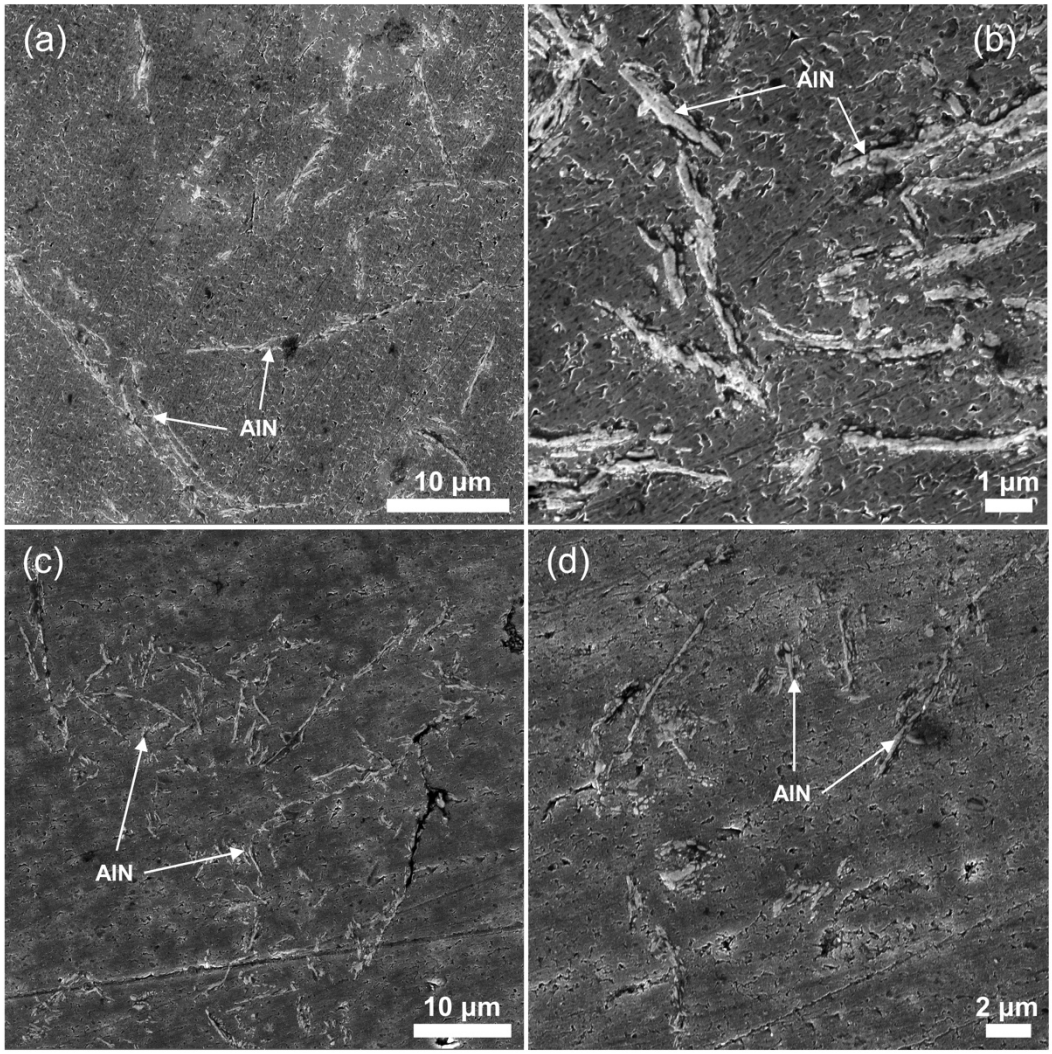

Figure 3.4. (a) SE SEM image showing the presence of elongated AlN particles in Al after processing for 150 min *via* the large-scale ISGR setup. (b) Higher magnification SE SEM image detailing the morphologies of AlN particles processed for 150 min *via* the large-scale ISGR setup. (c) SE SEM image showing the presence of elongated AlN particles in Al after processing for 100 min *via* the large-scale ISGR setup. (d) Higher magnification SE SEM image detailing the morphologies of AlN particles processed for 100 min *via* the large-scale ISGR setup.

The elongated AlN particles present in the large-scale Al-AlN alloys were considered to be undesirable for mechanical properties. Similar to the small laboratory-scale master alloys produced in this study, the anisotropic shape may arise due to ineffective breakage of particles by the impeller after formation at the N_2 bubble/Al melt interface. This theory may be further supported by the observation of longer particles for the lower impeller rotational speeds used here (250 RPM for large-scale versus 450 RPM for small-scale), and Borogonovo [13] also observed decreased AlN particle sizes for higher rotation speeds owing to increased mixing shear forces.

The observed curvature of the AlN particle chains in the large-scale master alloys may also be related to the impeller rotational speed, as Borgonovo [13] estimated speeds above 450 RPM are necessary to minimize bubble diameter assuming an Al melt viscosity at 1000 °C [13]. The difference in observed volume fractions of AlN between the large-scale batches batches is likely due to the difference in nitridation time, where increased nitridation time produces increased amounts of AlN material [13]. The observation of AlN particles concentrated in the bottom half of the melt may also be due to impeller setup sensitivities, as bubble densities, and consequently sites for AlN nucleation, are highly dependent on impeller depth in the melt [13, 31].

Overall, the ISGR process was deemed not ready for scale-up MMNC processing. Although the ability to create Al-AlN material in relatively large amounts (*i.e.,* approximately 10 kg here) is promising, further work needs to be conducted on optimization of processing parameters using the scaled-up approach. The differences in AlN morphology highlights the sensitivity of the ISGR process to not only nitridation parameters, but also processing parameters more closely tied to the mixing aspect of the approach.

3.4 Self-propagating high-temperature synthesis (SHS): Laboratory-scale

3.4.1 SHS master alloys: Processing methods

In situ Al-TiC composites were prepared at Worcester Polytechnic Institute (Worcester, MA) [31] *via* a modified thermite-assisted self-propagating high-temperature synthesis (SHS) process developed by Cho *et al.* [38]. To create the pellets for SHS experiments, powders of Al (~30 μm, 99.5% purity), Ti (~20 μm or ~44 μm, 99.7% purity), C (100nm or 9 μm, 99% purity), and CuO (<10 μm, 98%, purity) were mixed in composition ratios of 1.5 mol Al, 1 mol Ti, 1 mol C, and 0.1 mol CuO (with "high" C and CuO compositions corresponding to 1.1 mol and 0.155 mol, respectively). Two different mixing methods were used: in the first, Al, Ti, and C powders were ball milled together for 24 hrs and then combined with CuO *via* manual mechanical mixing (to avoid reaction inside the ball mill); and in the other, Al, Ti, C, and CuO were thoroughly mixed *via* a resonant acoustic mixing (RAM) technique. The powder mixture was subsequently pressed into a 30 mm die at 200 MPa to create pressed pellets (~20 g per packed pellet), or loosely packed and wrapped in Al-foil (~2.4 g per loose pellet, ~15 mm diameter). All pellets were pre-heated in a resistance furnace at 373 K (100 °C) for 2 hrs prior to each SHS experiment, in order to dry the powders and bake-off organic contaminants.

To create Al-TiC master alloys, approximately 500 g of Al ingot (99.99% purity) were melted in an induction furnace and pellets were inserted and pushed beneath the surface of the melt using a BN-coated submersion tool (constructed of a flat meshed steel plate and handle). The average bulk processing temperature during each experiment ranged from 1043 K (770 °C) to 1133 K (860 °C). Pellet additions in the melt were staggered by ~1-2 min to allow for the temperature to settle between each pellet. The specific number of pellets added in each batch varied depending on the target reinforcement volume percentages of 10 vol% TiC or 2 vol% TiC, which corresponded to raw powder/melt mass ratios ($r_{p/m}$) of approximately 0.32 and 0.07 respectively. The $r_{p/m}$ ratios were calculated assuming approximately 100% conversion of Ti and C. After pellet addition was completed, all batches were manually stirred and subsequently cast into molds at room temperature then allowed to solidify in ambient conditions. To assess the feasibility of SHS reaction directly in commercially relevant structural alloys (*i.e.*, Al alloys containing Si and Mg), several trials using Al-7Mg and A356 (composition: Al – 7Si – 0.3Mg) were also tested using the same processing method. A schematic depicting the general SHS experimental procedure is shown in Figure 3.5. A summary of all the process conditions used is shown below in Table 3.3.

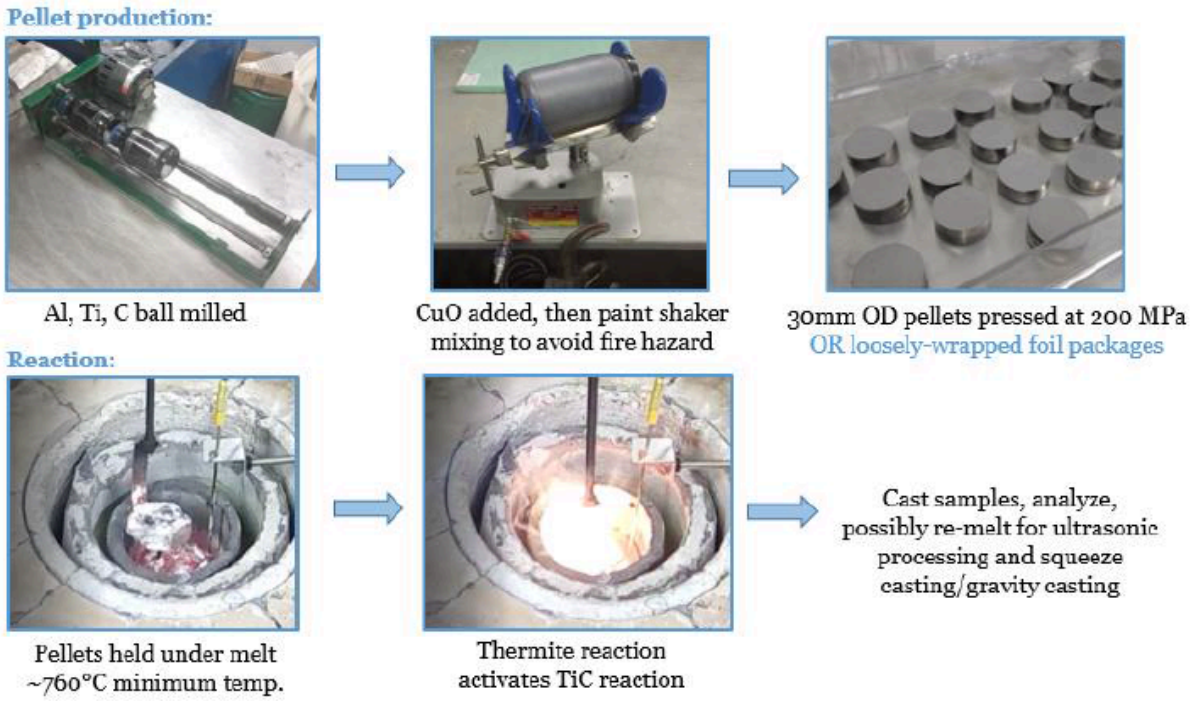

Figure 3.5. Schematic of the *in situ* self-propagating high-temperature synthesis (SHS) work flow developed at Worcester Polytechnic Institute (Worcester, MA), based upon the modified approach developed by Y.-H. Cho *et. al.* [38]. In the SHS process, compact pellets composed of Al, Ti, C, and CuO constituent powders are reacted by inserting into an Al melt. Adapted from [31].

Table 3.3. Summary of processing parameters used to create Al-TiC small-scale master alloys *via* SHS.

Sample ID	Base alloy	C amount, n_C [mol]	C size, d_C [µm]	CuO amount, n_{CuO} [mol]	Ti size, d_{Ti} [µm]	Pellet packing method [-]	Powder mixing method [-]	Powder/ melt ratio, $r_{p/m}$ [g/g Al]	Process temperature, T_{proc} [°C]
SHS-1	Pure Al	1	9	0.1	44	Pressed	Ball mill+mechanical	0.32	842
SHS-2	Pure Al	1	9	0.1	44	Pressed	Resonant acoustic	0.32	860
SHS-3	Pure Al	1	9	0.155	44	Pressed	Resonant acoustic	0.32	838
SHS-4	Pure Al	1.1	9	0.1	44	Pressed	Resonant acoustic	0.32	851
SHS-5	Pure Al	1.1	9	0.155	44	Pressed	Resonant acoustic	0.32	843
SHS-6	Pure Al	1.1	9	0.1	44	Pressed	Ball mill+mechanical	0.32	840
SHS-7	Pure Al	1.1	9	0.155	20	Pressed	Ball mill+mechanical	0.32	823
SHS-8	Pure Al	1.1	9	0.155	20	Loose	Ball mill+mechanical	0.07	780
SHS-9	Pure Al	1.1	9	0.155	20	Pressed	Ball mill+mechanical	0.07	770
SHS-10	Pure Al	1.1	0.1	0.155	20	Loose	Ball mill+mechanical	0.07	780
SHS-11	Al-7Mg	1.1	9	0.155	20	Pressed	Ball mill+mechanical	0.07	793
SHS-12	A356	1.1	9	0.155	20	Pressed	Ball mill+mechanical	0.07	800

3.4.2 SHS master alloys: Characterization and data processing methods

Metallographic specimens were prepared from Al-TiC master alloys by sectioning as-cast ingots and cold mounting in non-conductive epoxy (Mager Scientific). Several ingot locations were prepared from each master alloy batch to check for microstructure homogeneity. Mounted samples were ground and polished using an ATM Saphir 530 dual wheel auto-grinder/polisher. Mounted samples were hand ground with the platter rotating at 200 RPM using succesive 320, 400, 600, and 1200 grit SiC papers (Pace Technologies). Samples were polished to a "mirror finish" using 9 μm, 3 μm, and 1 μm polycrystalline diamond suspensions (Mager Scientific), with complimentary head/platter rotation at 150 RPM and 17 N of downward force per sample. After polishing, samples were bath sonicated for 30 s in ethanol to remove polishing particles embedded in the soft Al surface.

Al-TiC MMNC microstructures were characterized using either a Tescan MIRA3 FEG SEM operating at an accelerating voltage of 15 kV and a beam intensity of 12 – 15, or a FEI Nova 200 Nanolab SEM/FIB operating at an accelerating voltage of 15 kV and 1.6 – 2.1 nA (both microscopes were typically operated in backscatter electron (BSE) imaging mode to leverage the inherent high contrast difference TiC and Al [150]). An EDAX energy dispersive spectroscopy (EDS) system integrated with both SEMs was used for localized chemical identification of particles and secondary phase precipitates.

XRD scans of Al-TiC material were used to identify phases in bulk specimens as a complimentary technique to SEM. XRD scans were taken using a Rigaku Rotating Anode X-ray Diffractometer operating at 100 kV and 40 mA. Unmounted samples were hand ground using 400, 600, and 1200 grit SiC grinding paper to obtain a level and relatively smooth surface. XRD scans were taken using a 1.5 °/min scan rate and a 0.2° step size.

Relevant particle characteristics (*e.g.*, volume fraction, particle diameter) were determined from SEM micrographs. Micrographs were adjusted to maximize contrast using ImageJ (version 1.49) software prior to analysis as necessary. Segmentation or partitioning of phases into different classes and additional post-processing were carried out using the Image Processing toolbox in MATLAB 2018b. In general, the data processing workflow consisted of multi-level thresholding followed by median filtering to reduce background noise. From the segmented and processed images, the effective particle area fractions were calculated, and the effective particle diameters were determined based on the sizes of individual connected components within an area element.

3.4.3 SHS master alloys: Microstructural characterization and discussion

Representative SEM micrographs corresponding to the various SHS processing conditions are shown in Figure 3.6. From the wide variety of SHS microstructures it is apparent, speaking qualitatively, that a wide range of TiC reinforcement volume fractions, secondary phase precipitates, and reinforcement dispersions are capable of being produced. SHS runs generally appeared successful in producing the desired TiC reinforcement and the master alloy microstructures consisted of primarily spherical, sub-micrometer TiC particles embedded in the Al matrix (a summary of the key particle characteristics is shown in Table 3.4). In addition to TiC, a small amount of Al_3Ti intermetallics and of C-rich regions presumably corresponding to unreacted carbon were observed. A small amount of rod-like precipitates likely corresponding to Al_2O_3 were also observed. XRD was used to confirm the presence of TiC in bulk specimens. Spectra appeared similar between master alloy samples, but with variations in TiC peak intensity likely corresponding to variations in TiC volume fractions [151]. Representative XRD spectra of SHS batches containing approximately 2 vol % (Sample ID 1) and 1 vol % (Sample ID 7) are shown in Figure 3.7. The presence of only TiC and Al peaks is suggestive of TiC particles as the predominant phase after Al in the SHS MMNCs. Higher magnification micrographs, and corresponding EDS maps, identifying the chemistry of the specific microstructural features (*e.g.*, particles, intermetallics, excess C, and oxides) are shown in Figure 3.8.

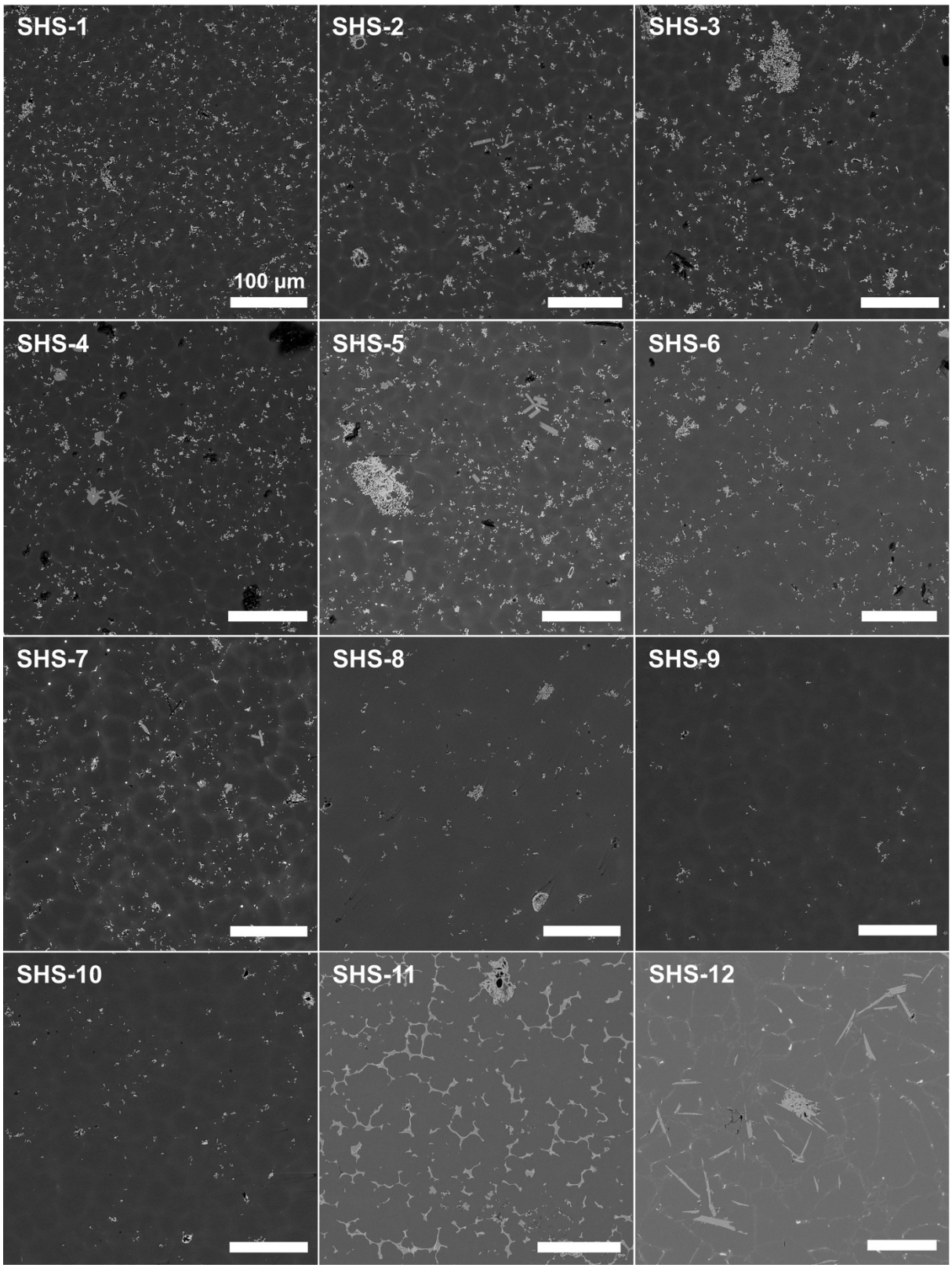

Figure 3.6. Representative BSE SEM images showing the microstructure of Al-TiC composites processed *via in situ* SHS (corresponding to the processing conditions and sample IDs shown in Table 3.3). Scale bar is 100 µm in all instances.

Table 3.4. Key particle characteristics (volume fraction TiC and average particle diameter) of Al-TiC composites produced *via in situ* SHS.

Sample ID	TiC particle volume fraction, v_{TiC} [%]	Average TiC particle diameter, d_{TiC} [nm]
SHS-1	2.0 ± 0.32	638 ± 42.6
SHS-2	2.1 ± 0.38	767 ± 30.2
SHS-3	2.1± 0.33	388 ± 50.6
SHS-4	1.8 ± 0.38	578 ± 51.3
SHS-5	2.1 ± 0.33	908 ± 22.8
SHS-6	0.8 ± 0.14	384 ± 12.9
SHS-7	0.9 ± 0.15	651 ± 25.0
SHS-8	0.1 ± 0.13	571 ± 40.2
SHS-9	0.3 ± 0.18	569 ± 45.5
SHS-10	0.4 ± 0.14	637 ± 32.5
SHS-11	<0.1	655 ± 53.0
SHS-12	<0.1	592 ± 14.0

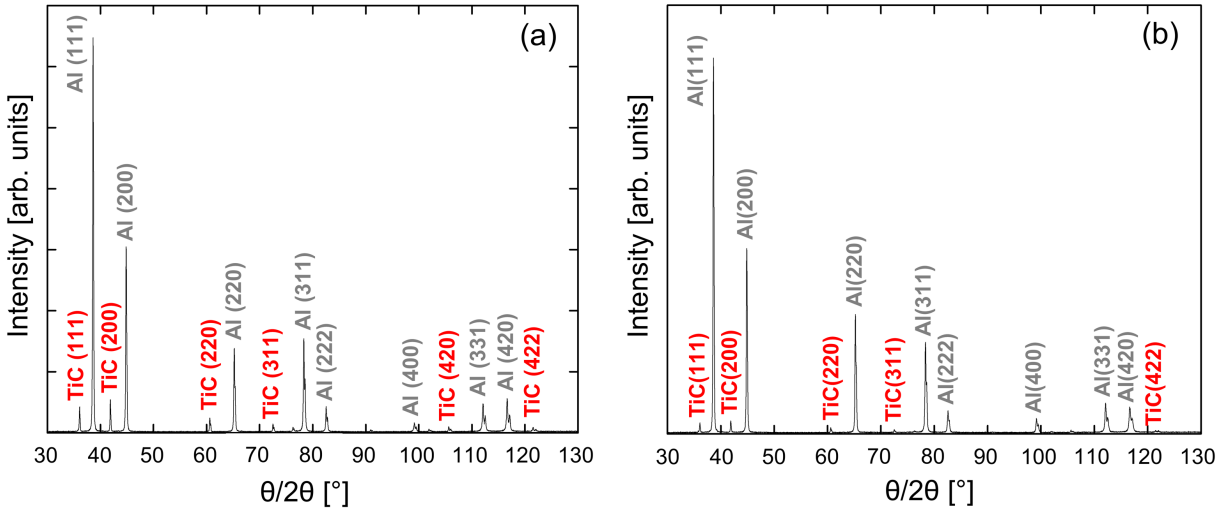

Figure 3.7. Representative XRD spectra of Al-TiC composites processed *via in situ* SHS. XRD spectra correspond to (a) 2vol% TiC reinforcement (Sample SHS-1) and (b) 0.9vol% TiC reinforcement (Sample SHS-7).

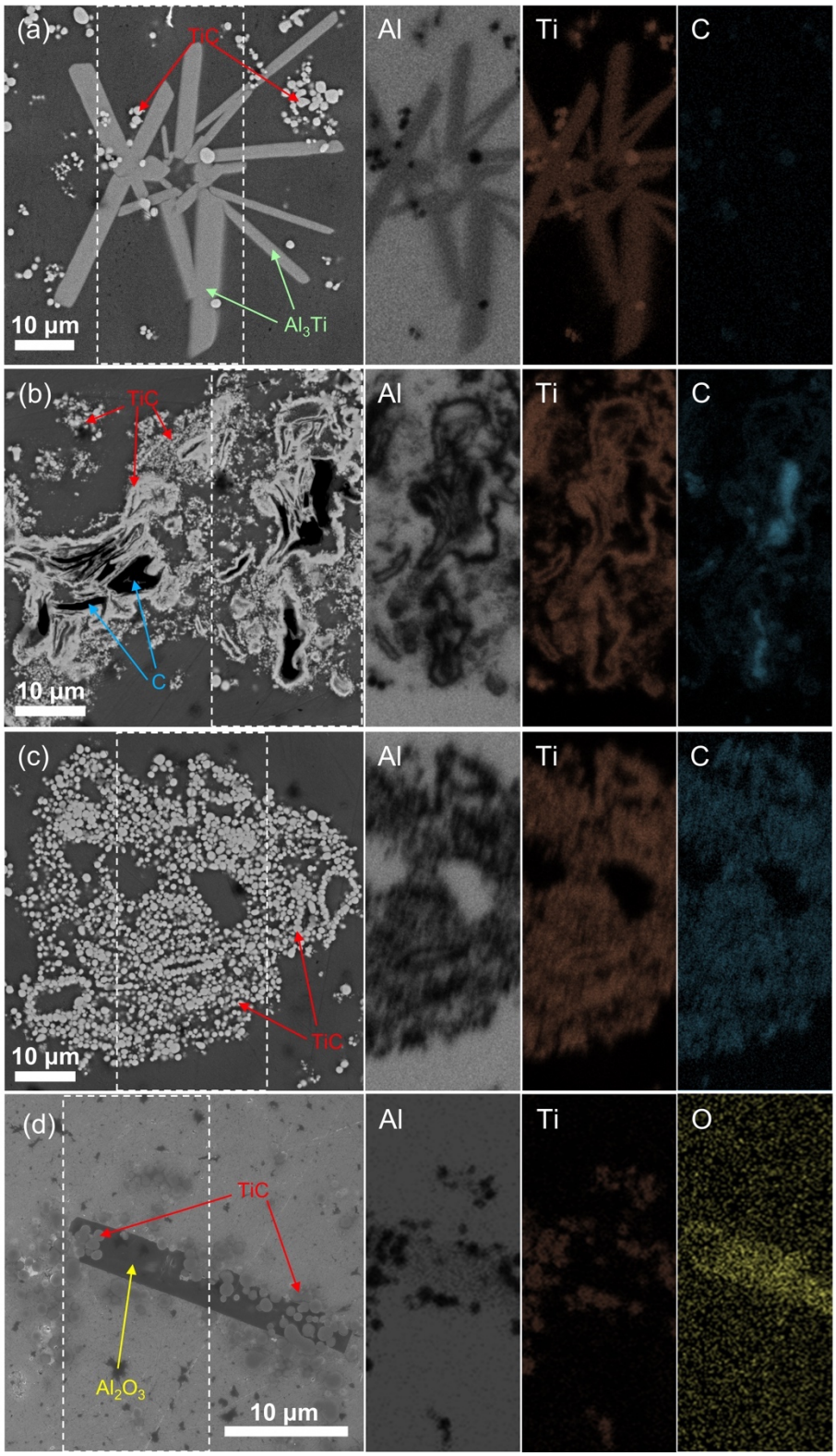

Figure 3.8. SEM observations and corresponding EDS maps (EDS spectra taken from area enclosed by the dashed box): (a) Al_3Ti intermetallics with surrounding TiC particles; (b) C-rich regions with surrounding TiC particles; (c) clustered and individual TiC particles; (d) Al_2O_3 oxides. (a)-(c) are BSE images and (d) is a SE image.

In SHS samples reacted in pure Al, the observed microstructural features were generally similar from batch to batch. The Al_3Ti precipitates exhibit an anisotropic and faceted structure with dimensions approximately 10-50 μm long and 5-15 μm wide. C-rich regions commonly exhibited a layer of TiC or cluster of particles surrounding them (on the order of tens of nm between C-rich regions and the surrounding TiC). Individual TiC particles, as well as solid and ring-like clusters, were also identified. The particles were largely spheroidal in shape, with some more ellipsoidal shapes also being present. The average TiC particle sizes ranged from approximately 380 to 910 nm, with a wide range of vol% from approximately 0.1 up to 2.1 vol%. Finally, a small amount of rod-like Al_2O_3 was observed, generally 10-30 μm in length and 3-5 μm wide. These microstructural features are consistent with the phases observed in other Al-TiC-C-based SHS processes, where excess C and Al_3Ti have been observed as byproducts of the SHS reaction [33, 152, 153]. The Al_2O_3 has been observed to be a byproduct of the CuO-assisted process specifically, resulting from the reduction of CuO by liquid Al [38, 154].

In contrast to pure Al melts, SHS samples reacted in Al-7Mg and A356 exhibited significantly less TiC particles, calculated to be <0.1 vol% for both batches (Sample SHS-11 and SHS-12 respectively). The observed secondary phases included anisotropic Al_3Ti, unreacted C, and Al_2O_3, similar to pure Al melts. However, the A356-based master alloy also exhibited phases corresponding to elongated Al-Ti-Si-based platelets (*e.g.*, $TiAl_xSi_y$) and faceted Al_4C_3 with clustered TiC particles attached (See Figure 3.9). The observation of these additional phases solely in the A356 material is suggestive of reaction or modification *via* Si.

In general, TiC is thermodynamically unstable in Al melts at temperatures below approximately 800 °C when Ti concentration is low (<0.2 wt% Ti), which leads to decomposition of TiC and the formation of Al_4C_3 at the particle melt interface [155, 156]. However, the onset of TiC dissolution under these conditions has been observed to occur at relatively long melt holding times (>1 hr at 800 °C) [157]. Despite a processing temperature of approximately 800 °C being used for Sample SHS-12, it is expected that the other processing conditions (*i.e.,* holding times under 1 hr and >0.2 wt% Ti) would render TiC stable. However, Si has been observed to alter the kinetics of TiC decomposition in Al-Si-TiC melts, leading to the formation of ternary $TiAl_xSi_y$ phases and Al_4C_3 at melt holding times are short as 10 min and temperatures below approximately 880 to 890 °C [158, 159, 160]. Consequently, even if TiC is formed *via* initial SHS reaction,

presumably the Si content in A356 may cause conversion into Al_4C_3 and $TiAl_xSi_y$ before the final microstructure is formed.

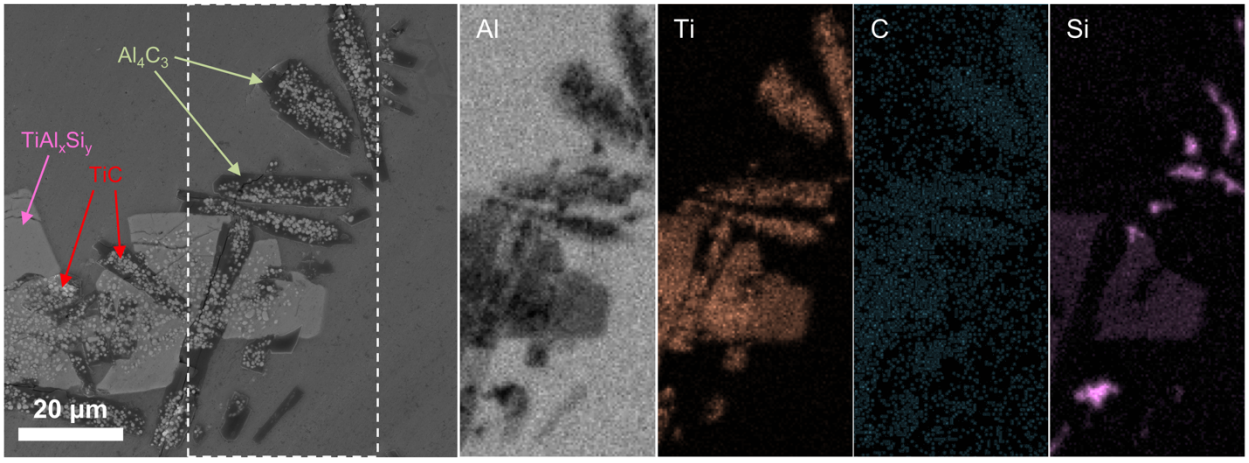

Figure 3.9. SEM observations and corresponding EDS maps (EDS spectra taken from area enclosed by the dashed box) of TiC particles, Al_4C_3 carbides, and $TiAl_xSi_y$ intermetallics formed in A356-TiC samples processed *via in situ* SHS.

Given the presence of spherical, sub-micrometer TiC particles, the SHS process provides a promising approach to producing reinforcement compatible with enhanced MMNC mechanical properties. To maximize TiC yield and minimize the presence of undesirable secondary phases, use of pure Al as the matrix material appeared to have the most potential. Consequently, two scale-up efforts were attempted: large-scale dilution of Al-TiC master alloys in A356 and direct SHS reaction in large-scale batches of pure Al.

3.5 Self-propagating high-temperature synthesis (SHS): Dilution scale-up approach

3.5.1 Dilution of SHS master alloys in A356: Experimental methods

In addition to conducting direct SHS reaction in Al-Si and Al-Mg based alloys, Al-TiC master alloys were diluted in A356 as an alternative approach to scale-up. Dilution of SHS master alloys in A356 was conducted at WPI. Diluted A356-TiC samples were processed by melting Al-TiC master alloys (See Table 3.3, Sample SHS-2 for specific master alloy processing parameters) with A356 in an induction furnace at approximately 760 °C. An appropriate amount of master alloy was added to target ~1 vol% reinforcement. Diluted melts were ultrasonically processed using a Southwire SRC Technologies Ultra-D ultrasonic degasser for 30 minutes, to encourage particle dispersion, and subsequently gravity cast into plates and allowed to cool under ambient

conditions. Plain/unreinforced A356 plates were melted and cast using the same conditions, sans ultrasonic dispersion, to be used as a reference.

As-cast A356-TiC and A356 plates were milled down approximately 1 mm on both faces to remove surface defects and ensure tensile specimen thickness uniformity. Subsequently, tensile specimens were cut from several locations of the milled plates *via* electric discharge machining (EDM) and were designed with a 25 mm gauge section length. Tensile tests were conducted using an MTS 810 static-hydraulic tensile tester under ambient conditions. Force and crosshead displacement, as measured by the MTS unit, were used to calculate engineering stress and strain according to Eqn. (3.1) and (3.2). Modulus of elasticity was calculated according to Eqn. (3.3), using stress and strain values from the linear portion of the stress-strain curves. Total elongation was calculated using equation 2.4.

$$\sigma = \frac{F}{A} \tag{3.1}$$

$$\varepsilon = \frac{\Delta L}{L_0} \tag{3.2}$$

$$E = \frac{\sigma}{\varepsilon} \tag{3.3}$$

$$EL = \frac{L_f - L_0}{L_0} \tag{3.4}$$

Yield strength (YS) was determined from the linear portion of the curves using the 0.2% offset method [161]. Polished cross sections of the tensile specimens were prepared according to the metallographic techniques detailed in Section 3.4.1, but with the addition of post-polish etch. Cross sectional samples were etched for 10 s in a 10 vol% NaOH-DI water mixture, followed by immediate DI water rinsing and submersion in a 65 °C stirred DI water bath for 1 min. Both polished cross sections and fracture surfaces of *post mortem* tensile specimens were analyzed using SEM and EDS, equipment and operating parameters detailed in Section 3.4.2.

3.5.2 Dilution of SHS master alloys in A356: Results and discussion

Stress-strain curves for selected A356-TiC and reference A356 tensile specimens are shown in Figure 3.10 and the mechanical properties are summarized in Table 3.5. The A356-TiC exhibited slightly enhanced mechanical properties, with an approximately 19% increase in yield strength (YS) and 26% increase in ultimate tensile strength (UTS) as compared with the base A356 material. There is a relatively wide variance in ductility, even among A356 and A356-TiC samples, ranging from approximately 2 – 6% elongation for A356 and approximately 3 – 8% for reinforced

material. In general, the addition of particulate reinforcement is associated with a ductility decrease as compared with unreinforced material [89, 90, 162], but increases in MMNC ductility have also been attributed to grain refinement in TiC reinforced Al alloys [96, 109]. However, no apparent grain refinement was observed here and elongation variances are likely largely due to defect and porosity density variances in the castings, which have been observed to have a larger effect on ductility versus other tensile properties [163, 164, 165].

It is interesting to note the serrated appearance of several of the A356-TiC curves, and in the plain A356 to a lesser extent. Stress-strain curve serrations may be due to the Portevin-Le Chatelier (PLC) effect, in which inclusions of reinforcement particles in the matrix induce inhomogeneous plastic deformation as dislocations become repeatedly pinned and break free from obstacles in the material. In the case of MMNCs, the reinforcement particles are able to act as pinning points and dislocations break free during interfacial fracture [166]. However, it is also possible that inhomogeneous deformation is brought on by porosity or a high density of casting defects in the material and the PLC effect has also been observed to be a strongly dependent on specimen porosity [167]. Presumably, a combination of both effects contributes to inhomogeneous deformation here considering the presence of large serrations in the reinforced material and small serrations in the unreinforced material.

Fracture surfaces of A356-TiC were observed to contain a mix of ductile and brittle fracture surfaces, which is consistent with commercial Al-Si alloys [168, 169] (See Figure 3.11(a)). TiC particles were observed to be clustered on the fracture surface in smooth pockets or regions (See Figure 3.11(b-c)). Clustering may be indicative of particle agglomeration during processing or particle drag during re-solidification. Further EDS analysis suggests that the regions where particles are clustered or embedded may be composed of a $TiAl_xSi_y$-based phase, which was not present in the initial master alloy (See Figure 3.12). The appearance of a new Ti- and Si-containing ternary phase is suggestive of a reaction occurring between the TiC particles and Si in the A356 alloy during master alloy re-melting and dilution. Presumably, $TiAl_xSi_y$ forms as a result of the inherent instability of TiC in Si-containing Al melts, similar to our observations in direct A356 SHS reaction [155, 157, 158, 159, 160]. The grouping of particles on $TiAl_xSi_y$-based phases may also be suggestive of nucleation stemming from TiC particles as the Ti source.

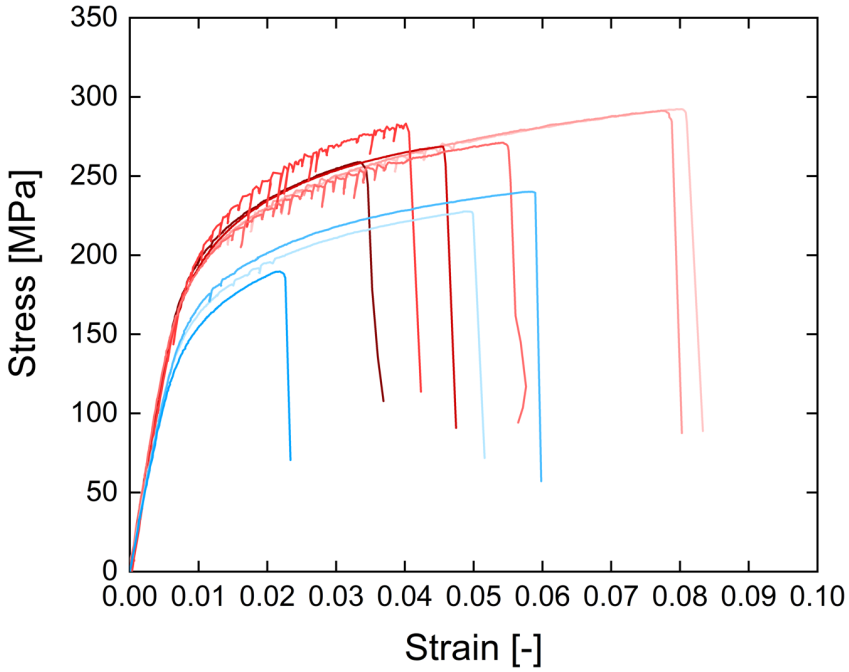

Figure 3.10. Engineering stress-strain curves of A356-TiC (red) and A356 (blue) tensile specimens tested at room temperature.

Table 3.5. Summary of the mechanical properties of A356-TiC and A356 tensile specimens tested at room temperature. Corresponding stress-strain curves shown in Figure 3.10.

Sample ID	Ultimate Tensile Strength [MPa]	Yield Strength [MPa]	Modulus of Elasticity [GPa]	Elongation [%]
A356/TiC-1	269	184	92	4.7
A356/TiC-2	283	199	99.5	4.2
A356/TiC-3	271	186	93	5.7
A356/TiC-4	292	187	93.5	8.2
A356/TiC-5	291	187	93.5	7.9
A356/TiC-6	259	193	96.5	3.5
A356-1	228	158	79	5.1
A356-2	240	165	82.5	6.0
A356-3	190	152	76	2.3

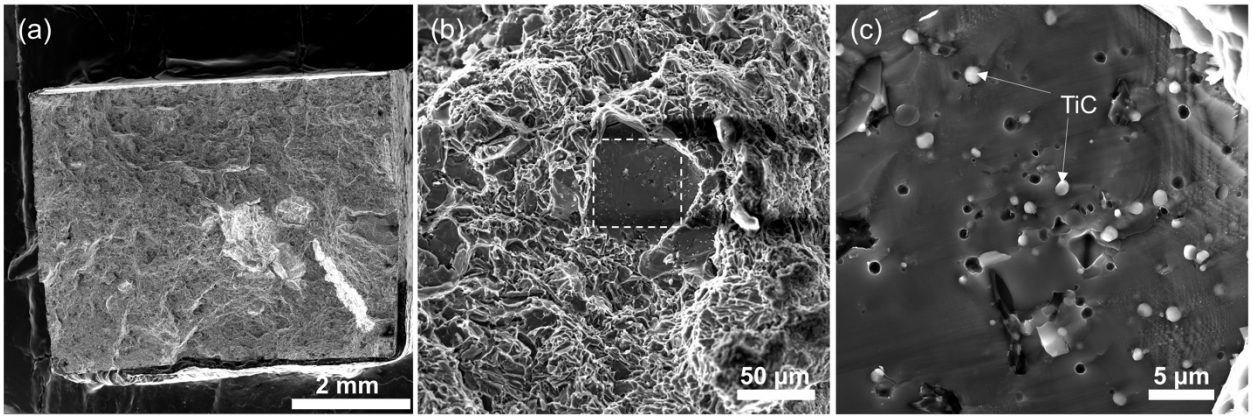

Figure 3.11. SEM images of a fracture surface of A356-TiC tensile specimen showing (a) macroscopic fracture surface; (b) smooth regions containing TiC particles; (c) higher magnification image of TiC particles.

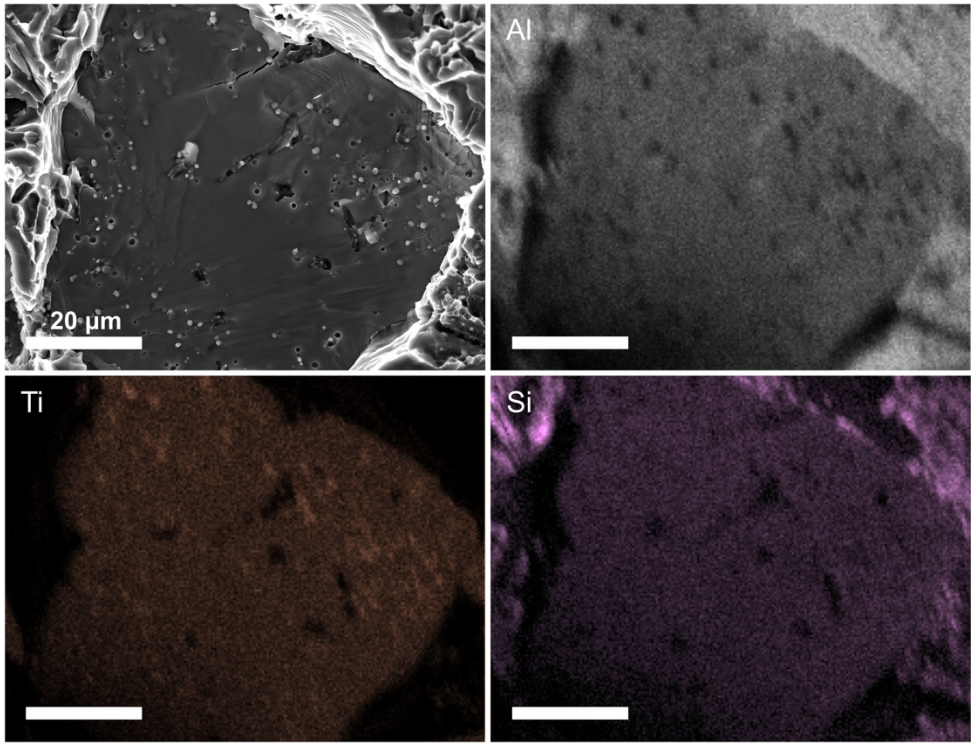

Figure 3.12. Representative SEM image and corresponding EDS spectra of $TiAl_xSi_y$ precipitate and embedded TiC particles observed on A356-TiC fracture surfaces.

Although no apparent Al_4C_3 was observed in the fracture surfaces, as was expected from the direct A356 SHS reaction experiments, precipitates corresponding to Al_4C_3 and $TiAl_xSi_y$ phases were observed in the polished tensile specimen cross sections (See Figure 3.13). TiC particles appear attached to both types of precipitates, possibly indicating that groups of particles may act as nucleation sites. EDS maps identifying the chemistry of $TiAl_xSi_y$ and Al_4C_3 are shown

in Figure 3.14 and Figure 3.15 respectively. Interestingly, a strong oxygen signal is also observed in the EDS maps for the potential Al_4C_3 that corresponds well with the precipitate shape and was not observed in other samples containing Al_4C_3. The oxygen signal may suggest a partial oxidation reaction of the Al_4C_3 precipitates during metallographic preparation, either due to the NaOH-based etchant or warm water rinse, which have been reported to be highly sensitive to moisture and oxygen content leading to Al_2O_3 or various aluminum oxycarbide based byproducts (*e.g.*, AlO_xC_y) [170, 171, 172, 173]. The appearance of both Al_4C_3 and $TiAl_xSi_y$ in the diluted specimens suggests that both phases arise during holding TiC particles in the melt rather than Si modification of the reaction and initial TiC formation, in agreement with the direct SHS A356 reaction sample observations. The dissolution of TiC and formation of larger effective precipitate phases may explain the relatively low mechanical property enhancement of A356 by SHS master alloy dilution and rule out A356 as a viable base alloy for SHS MMNC scale-up.

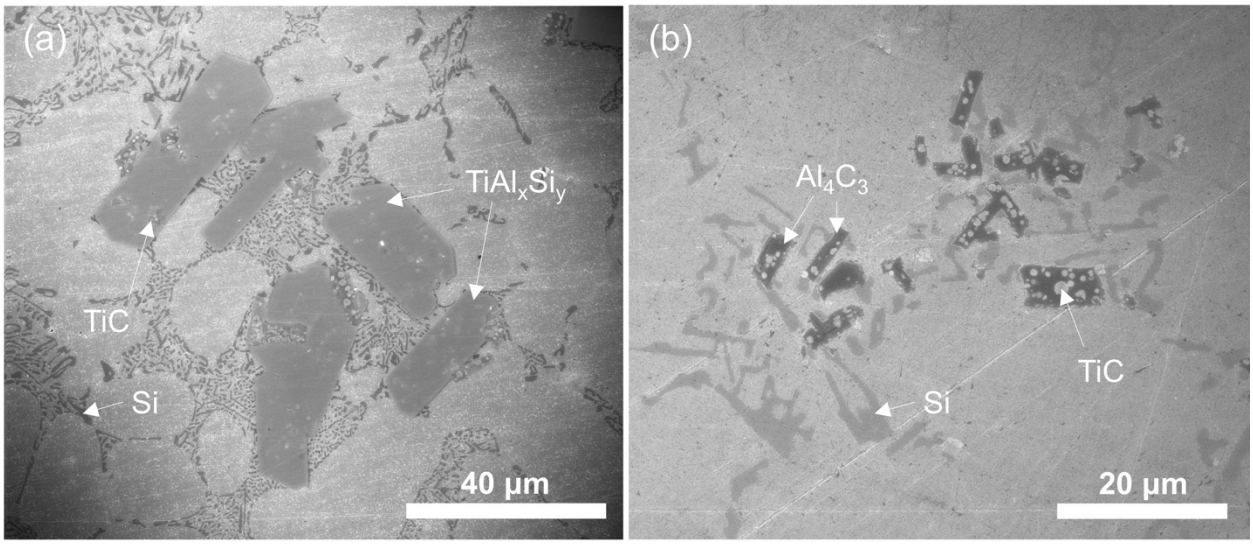

Figure 3.13. Representative SEM images showing the presence of (a) $TiAl_xSi_y$ precipitates and (b) Al_4C_3 precipitates in A356-TiC tensile specimens.

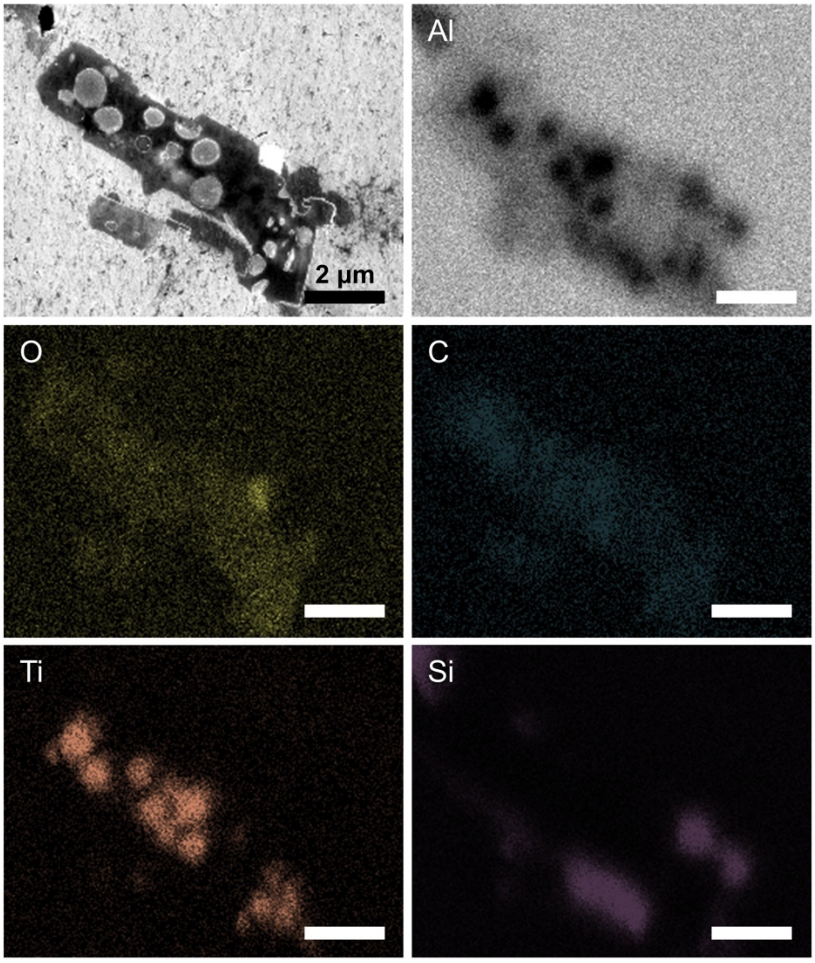

Figure 3.14. Representative SEM image and EDS spectra of Al_4C_3 precipitate in A356-TiC.

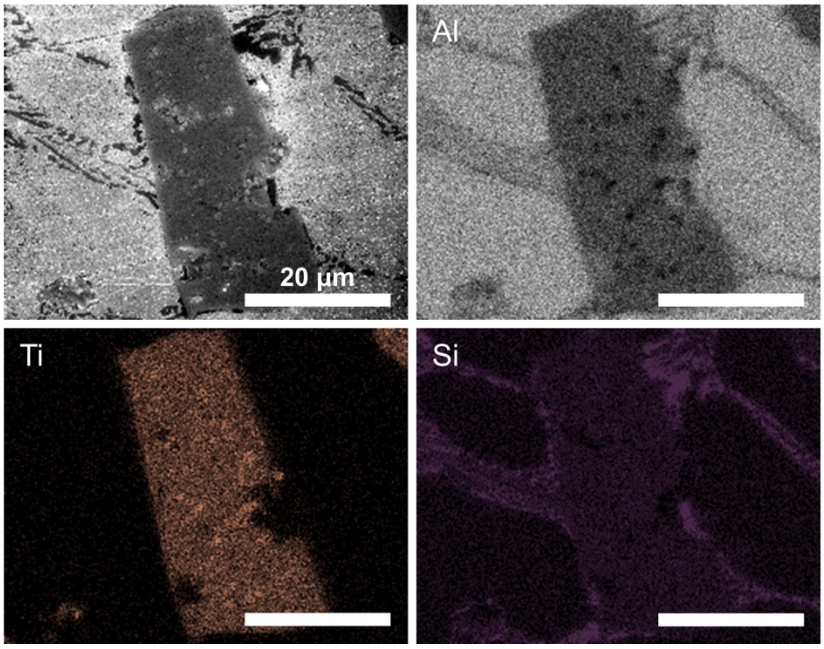

Figure 3.15. Representative SEM image and EDS spectra of $TiAl_xSi_y$ precipitate in A356-TiC.

3.6 Self-propagating high-temperature synthesis (SHS): Direct reaction scale-up approach

3.6.1 Scale-up of SHS experiments: Experimental methods

Based on the relative success of the small-scale SHS experiments in pure Al, and the results of direct SHS reaction in A356 and Al-7Mg and A356 dilution, a production-scale experiment was conducted at Eck Industries (Manitowoc, WI) involving reaction in commercial purity Al. The method used for pellet creation was identical to the small-scale experiments (See Section 3.4.1), with an increased number of pellets being used to target the desired vol % of TiC reinforcement. To create large-scale Al-TiC alloys, approximately 30 lbs (~13.6 kg) of commercial purity Al alloy (P1020, 99.7% Al) were melted in an induction furnace at 760 °C. Pellets were added to the melt using the same method as the small-scale master alloys, with a target reinforcement volume percentage of 2 vol% TiC ($r_{p/m}$ of 0.07). After pellet addition was finalized, the melt was processed using a Southwire SRC Technologies Ultra-D ultrasonic degasser for 30 minutes, to encourage particle dispersion in the larger melt volume, and subsequently gravity cast into bars and allowed to solidify at ambient temperature. The experimental processing conditions are shown in Table 3.6.

Table 3.6. Summary of processing parameters used to create large-scale Al-TiC MMNC *via* SHS.

Sample ID	Base alloy	C amount, n_C [mol]	C size, d_C [µm]	CuO amount, n_{CuO} [mol]	Ti size, d_{Ti} [µm]	Pellet packing method [-]	Powder mixing method [-]	Powder/ melt ratio, $r_{p/m}$ [g/g Al]	Process temperature, T_{proc} [°C]
SHS-13	P1020 (99.7% Al)	1.1	9	0.155	20	Pressed	Ball mill+mechanical	0.07	760

Tensile specimens of 50 mm gauge length were prepared *via* milling and machining and subsequently pulled, all at Eck Industries. Stress-strain plots and relevent mechanical properties were determined using force and crosshead displacement, as measured by the testing machine, and the methods outlined in Section 3.5.1. Polished cross sections of the tensile specimens were prepared according to the metallographic techniques detailed in Section 3.4.2. Both polished cross sections and fracture surfaces of *post mortem* tensile specimens were analyzed using SEM, equipment and operating parameters detailed in Section 3.4.2.

3.6.2 Scale-up of SHS experiments: Results and discussion

Stress-strain curves for TiC-reinforced P1020 and plain P1020 samples are shown in Figure 3.16 and the associated mechanical properties are summarized in Table 3.7. It is worth noting that in both reinforced and unreinforced P1020, there is an exponential increase in the stress-strain curves immediately at the beginning of testing. However, this is likely an artifact due to delayed seating of the grips on the samples. Consequently, the YS and modulus of elasticity were calculated based on the linear region of the curves after the grips are fully seated.

The P1020-TiC exhibited a clear enhancement in mechanical properties, with an approximately 26% increase in YS and a 50% increase in UTS as compared with the base P1020 material. Similar to the diluted A356-TiC material, a relatively wide variance in ductility ranging from 13 – 38% elongation for P1020-TiC and 20 – 46% elongation for P1020, is observed with no clear trend. Based on visual inspection of the tensile specimen cross sections, it is likely that these variances are largely due to ductility dependence on material porosity and defect density [163, 164, 165]. Serrated behavior is seen in the TiC-P1020 stress-strain curves, possibly suggestive of the PLC effect, as observed in the A356-TiC material.

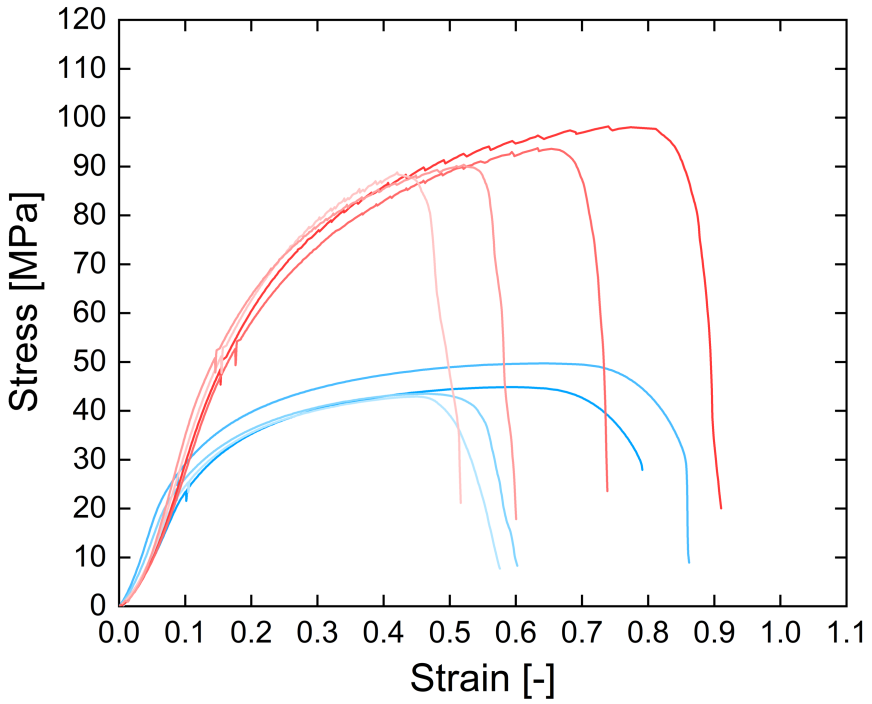

Figure 3.16 Engineering stress-strain curves of P1020-TiC (red) and P1020 (blue) tensile specimens tested at room temperature.

Table 3.7. Summary of the mechanical properties of P1020-TiC and P1020 tensile specimens tested at room temperature. Corresponding stress-strain curves shown in Figure 3.16.

Sample ID	Ultimate Tensile Strength [MPa]	Yield Strength [MPa]	Modulus of Elasticity [GPa]	Elongation [%]
P1020/TiC-1	110	40.0	44.0	38
P1020/TiC-2	99.3	44.8	33.8	13
P1020/TiC-3	95.8	41.4	62.7	22
P1020/TiC-4	104	47.6	30.7	24
P1020-1	70.3	34.5	5.57	46
P1020-2	70.3	31.7	42.0	24
P1020-3	66.2	33.8	23.5	20
P1020-4	66.2	37.9	0.858	33

TiC-P1020 fracture surfaces were observed to be suggestive of ductile fracture, with apparent casting defects in some cases (See Figure 3.17(a)). Individual TiC particles and particle clusters were found in fracture surface pockets and were generally uniformly in all surface regions (See Figure 3.17(b)). Polished tensile specimen cross sections revealed a relatively uniform TiC particle dispersion, with some excess C, elongated Al_3Ti, and Al_2O_3 consistent with the observed phases in the small-scale Al-TiC master alloys (See Figure 3.17(c-d)). In contrast to the SHS master alloys, a small amount of Fe was observed in the grain boundaries, likely owing to the composition of commercial purity P1020 (99.7% Al, 0.2% Fe) versus high purity Al (99.99% Al) (See Figure 3.17(d)).

In general, the results of the scaled-up P1020-TiC alloy produced *via* SHS are promising, exhibiting enhanced mechanical properties in terms of YS and UTS, as well as successful production of dispersed sub-micrometer TiC particles in a commercial-scale batch of material. However, further work needs to be done to understand the influence of the processing parameters on the particle and microstructural characteristics to enable fine tuning of SHS MMNCs.

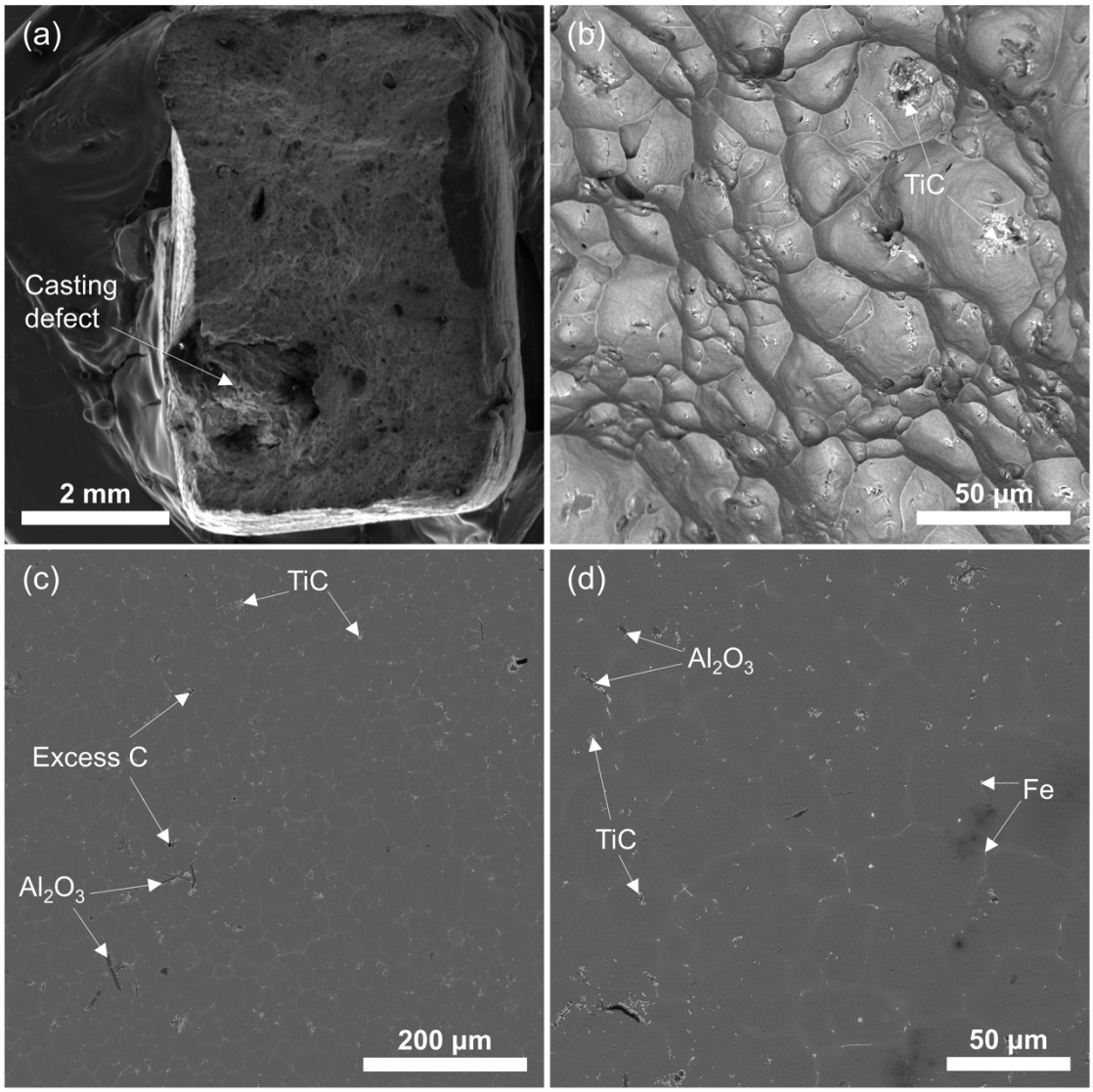

Figure 3.17. Representative SEM images of (a) low mag P1020-TiC fracture surface; (b) higher mag P1020-TiC fracture surface, showing clusters of TiC particles; (c) low mag polished cross section of a P1020-TiC tensile specimen; (d) high mag polished cross section of a P1020-TiC tensile specimen.

3.7 Conclusions

In this chapter, we have investigated *in situ* Al-AlN and Al-TiC MMNCs processed *via* ISGR and SHS routes respectively and assessed their potential for commercial-scale MMNC production. ISGR Al-AlN MMNCs generally consisted of elongated particles that were considered undesirable for mechanical properties. The anisotropic particle shape was attributed to insufficient shear force from the impeller, where the particles are intended to be broken into smaller lengths during mixing. The scale-up of the ISGR setup was assumed to be highly sensitive to parameters

relating to the impeller and mixing aspects of the process and requires further optimization before it can be adapted to large-scale production of *in situ* MMNCs. In contrast, the SHS process was found to be promising for the scaled-up production of material, and Al-TiC MMNCs with sub-micrometer, well dispersed particles were produced successfully in commercial pilot-scale quantities. The SHS Al-TiC MMNCs exhibited enhanced mechanical properties (26% increase in YS and 50% increase in UTS for 0.7 vol %TiC addition) at room temperature.

CHAPTER 4

In Situ Al-TiC Composites Fabricated by Self-Propagating High-Temperature Reaction: Insights on Reaction Pathways and Their Microstructural Signatures

Note: The work presented in the following chapter is adapted from C.W. Reese, *et. al.* published in *Metallurgical and Materials Transactions A* [143].

4.1 Introduction

Based on the results of the LIFT project investigating scale-up processing of *in situ* MMNCs, the SHS process proved to be the most promising (See Chapter 2). In particular, the SHS approach under investigation utilizes a small amount of thermite (2.7 mol% CuO) to aid the reaction and allow for the SHS processing of TiC/Al MMNCs at relatively low bulk temperatures (750-920 °C) [38, 80]. However, the underlying mechanisms of the particle formation are not well understood which limits the ability to further optimize the process for large-scale production. The SHS reaction pathways for TiC formation have been theorized to be complex and several different direct and indirect mechanisms have been hypothesized, each impacting the final microstructure in different ways [38, 41, 80, 81, 174].

The investigation outlined in this chapter seeks to better understand the SHS process and is aimed at answering two main questions: First, what are the governing mechanisms of particle formation? Secondly, how are the reaction mechanisms impacted by the processing variables? To this end, we present an integrated approach to understanding the production of *in situ* TiC/Al MMNCs *via* SHS. Focusing on the CuO-assisted method, we analyze a variety of microstructures from different SHS processing conditions and characterize key particle characteristics (*e.g.*, particle diameter, particle volume fraction, dispersion/agglomeration, and secondary phase volume fractions) using 2D and 3D techniques. While traditional 2D methods like SEM offer the possibility of relatively large area and bulk sample imaging, they may fail to be representative of the true 3D microstructure or capture material inhomogeneities; this is particularly important for accurate assessments of characteristics such as particle dispersion. Thus, we utilize transmission

X-ray microscopy (TXM) to visualize the microstructure in 3D with nano-scale resolution and supplement our 2D characterization methods. We combine our 2D and 3D microstructural observations to elucidate the TiC and secondary phase formation mechanisms and reaction pathways. To link these microstructural observations to the processing variables in a quantitative manner, we conduct a canonical correlation analysis (CCA). This multivariate statistical technique sheds light on the processing parameters that are maximally correlated to the agglomeration and dispersion of the TiC particles, among other microstructural descriptors.

It is important to note that the SHS experiments carried out in this chapter are part of a subset of the experiments discussed in Chapter 3 (Section 2.4). However, some experiments discussed in Chapter 3 (*i.e.*, Sample SHS-10, 11, and 12) are omitted here due to insufficient data needed for the multivariate statistical analysis described in Section 4.4. Thus, for consistency throughout the chapter, only samples utilized in Section 4.4 are considered in the discussion of experimental methods.

4.2 Experimental methods

4.2.1 SHS experiments

In situ Al-TiC composites were prepared at Worcester Polytechnic Institute (Worcester, MA) *via* a modified SHS process developed by Cho *et al.*, wherein pellets containing various ratios of raw elemental powders (Al, Ti, C) and copper thermite (CuO) are directly reacted in an Al melt [31, 38]. The experimental procedure to create the corresponding SHS pellets and melts is described in detail in Chapter 3, Section 3.4.1. In this study, several processing parameters were varied as shown in Table 4.1.

Table 4.1. Summary table of experimental conditions varied between SHS processing batches.

Sample ID	C amount, n_C [mol]	CuO amount, n_{CuO} [mol]	Ti size, d_{Ti} [µm]	Pellet packing method [-]	Powder mixing method [-]	Powder/melt ratio, $r_{p/m}$ [g/g Al]	Process temperature, T_{proc} [°C]
1	1	0.1	44	Pressed	Ball mill + mechanical mix	0.32	842
2	1	0.1	44	Pressed	Resonant acoustic mix	0.32	860
3	1	0.155	44	Pressed	Resonant acoustic mix	0.32	838
4	1.1	0.1	44	Pressed	Resonant acoustic mix	0.32	851
5	1.1	0.155	44	Pressed	Resonant acoustic mix	0.32	843
6	1.1	0.1	44	Pressed	Ball mill + mechanical mix	0.32	840
7	1.1	0.155	20	Pressed	Ball mill + mechanical mix	0.32	823
8	1.1	0.155	20	Loose	Ball mill + mechanical mix	0.07	780
9	1.1	0.155	20	Pressed	Ball mill + mechanical mix	0.07	770

4.2.2 Characterization techniques

Metallographic specimens were prepared from SHS Al-TiC master alloys and polished to a 1 μm polycrystalline diamond surface finish using the standard metallographic preparation techniques outlined in Chapter 3, Section 3.4.2. After polishing, samples were bath sonicated for 30 s in ethanol to remove residual polishing particles embedded in the soft Al surface.

Bulk microstructural characterization was performed using a Tescan MIRA3 field emission gun (FEG) SEM operating in backscatter electron (BSE) mode at 15 kV and a beam intensity of 12-15, while an integrated EDAX energy dispersive spectroscopy (EDS) system was utilized for chemical identification of particles and secondary precipitates. 184 images across 18 samples (2 separate ingot locations per Sample ID condition) were analyzed in order to provide statistically significant correlations (See Section 4.4).

To supplement our 2D microstructural characterization, the cast samples were also visualized in 3D at nanoscale resolution. Micropillar specimens for TXM characterization were prepared by taking as-cast ingots and cutting out 1 mm diameter rods (10-15 mm in length) *via* electrical discharge machining (EDM). Rods were subsequently sharpened on one end to approximately 100 μm diameter tips *via* electropolishing. To electropolish samples, a beaker containing a solution of 25 vol% NHO_3 and 75 vol% CH_3OH was first cooled for 10 min in liquid N_2. Subsequently, one end of a EDM cut sample (*i.e.*, the workpiece or anode) and a steel plate (*i.e.*, the cathode) were submerged in the electrolyte at opposite ends of the beaker for the electropolishing procedure. 10 V was used for bulk material removal (approximately 1-2 min) and a final polish at 5-7.5 V was used to minimize surface roughness and better control taper and the onset of pitting. Electropolished tips were shaped into final micropillars ≤40 μm in diameter and 80-100 μm in height using a FEI Nova 200 Nanolab SEM/FIB equipped with a Ga^+ ion beam. A FIB accelerating voltage of 30 keV was used in conjunction with various milling currents, starting with 20 nA for coarse milling and stepping down to sequential 5 nA and 1 nA milling steps to minimize taper and surface roughness. A schematic depicting the TXM sample preparation process is shown in Figure 4.1.

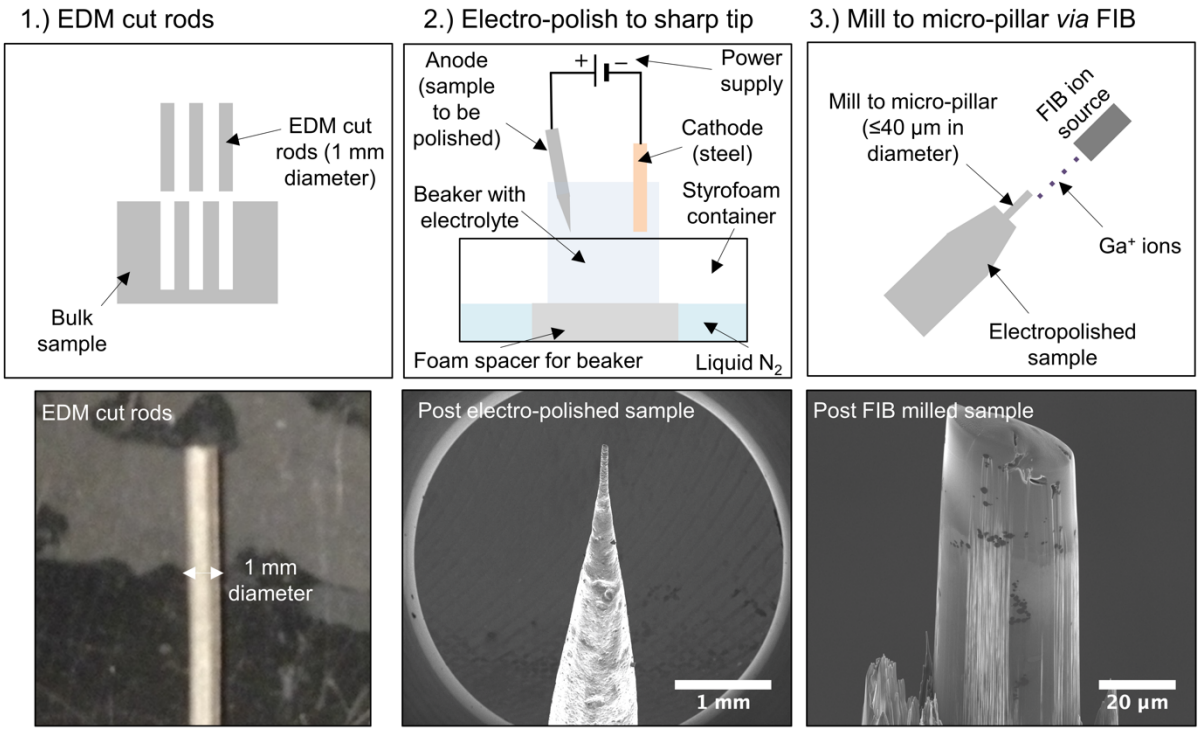

Figure 4.1. (top row) Schematic illustration of TXM sample preparation steps. (bottom row) Photographs and SEM micrographs of samples after the corresponding preparation step above it is performed.

Absorption full-field hard X-ray nanotomography experiments were conducted *via* TXM at Sector 32-ID at the Advanced Photon Source in Argonne National Laboratory (Lemont, IL) [175]. The un-milled end of each sample was clamped to a stainless-steel needle to ensure correct micropillar height in the TXM, and samples were subsequently placed on a high precision air-bearing rotary stage capable of 360° rotation. A monochromatic X-ray beam operating at 8 keV was focused onto the samples using a monocapillary condenser and a Fresnel zone plate with 50 nm outermost-zone-width served as an objective lens to magnify the images. Projections were acquired using a detector assembly comprising a LuAG scintillator, a Mitutoyo long working distance objective lens, and a CCD. A more detailed description of the TXM setup is available elsewhere [175, 176]. Using this configuration, a spatial resolution of 50 nm for a pixel size of 22.3 nm with a field-of-view of 2448 × 2048 pixels (or approximately 54 × 45 μm^2) on the detector plane was achieved. For each scan, projections were taken at 0.15° angular increments from 0° to 180° with an exposure time of 1 s or 0.5 s (contrast between sample elements was large enough that there was minimal difference between exposure times). In total, we captured 16 scans (tomograms) from 9 different samples *via* TXM to augment our SEM observations (Section 4.4).

4.2.3 Data processing and visualization methods

SEM micrographs were adjusted to maximize contrast using ImageJ (version 1.49) software prior to analysis. A representative micrograph after contrast adjustment is shown in Figure 4.2(a). The differences in backscattering contrast easily reveal the Al_3Ti intermetallic precipitates (medium grey) and TiC particles (bright) against the Al matrix (dark) [150]. Segmentation or partitioning of phases into different classes and additional post-processing were carried out using the Image Processing toolbox in MATLAB 2018b. In general, the data processing workflow consisted of multi-level thresholding followed by median filtering to reduce background noise. From the segmented and processed images, we calculated the particle (and intermetallic) areas (and hence, effective particle diameters) based on the sizes of individual connected components. The spacing between centroids of connected components (corresponding to the interparticle distance) was calculated *via* a *k*-nearest neighbors algorithm [177, 178, 179].

The TXM projection data was reconstructed into 3D using TomoPy, a Python-based open source framework for tomographic data processing [180]. Projections were first normalized using dark- and white-field images (*i.e.*, flat field correction) and subsequently the data were reconstructed *via* the Gridrec algorithm with Parzen filtering [181, 182]. A representative reconstruction slice along the axis of rotation is shown in Figure 4.2(b), where the Al matrix (dark grey), Al_3Ti (medium grey), and TiC (bright) are easily distinguishable due to differences in absorption contrast. The greyscale intensities of the individual slices were normalized using the Beer-Lambert law to account for small differences in slice diameter. Subsequently, the 2D slices were segmented using the same approach as for the SEM images. The segmented 2D slices were combined into a 3D volume and post-processed using the same methods as for the SEM images (*i.e.* median filtering, connected component labeling, and a *k*-nearest neighbor search). Interfaces between the phases were meshed in 3D to facilitate 3D visualization. A representative mesh is shown in Figure 4.2(c), with the TiC colored in red and Al_3Ti intermetallics shown in green. Several rotated views of the 3D mesh are shown for clarity.

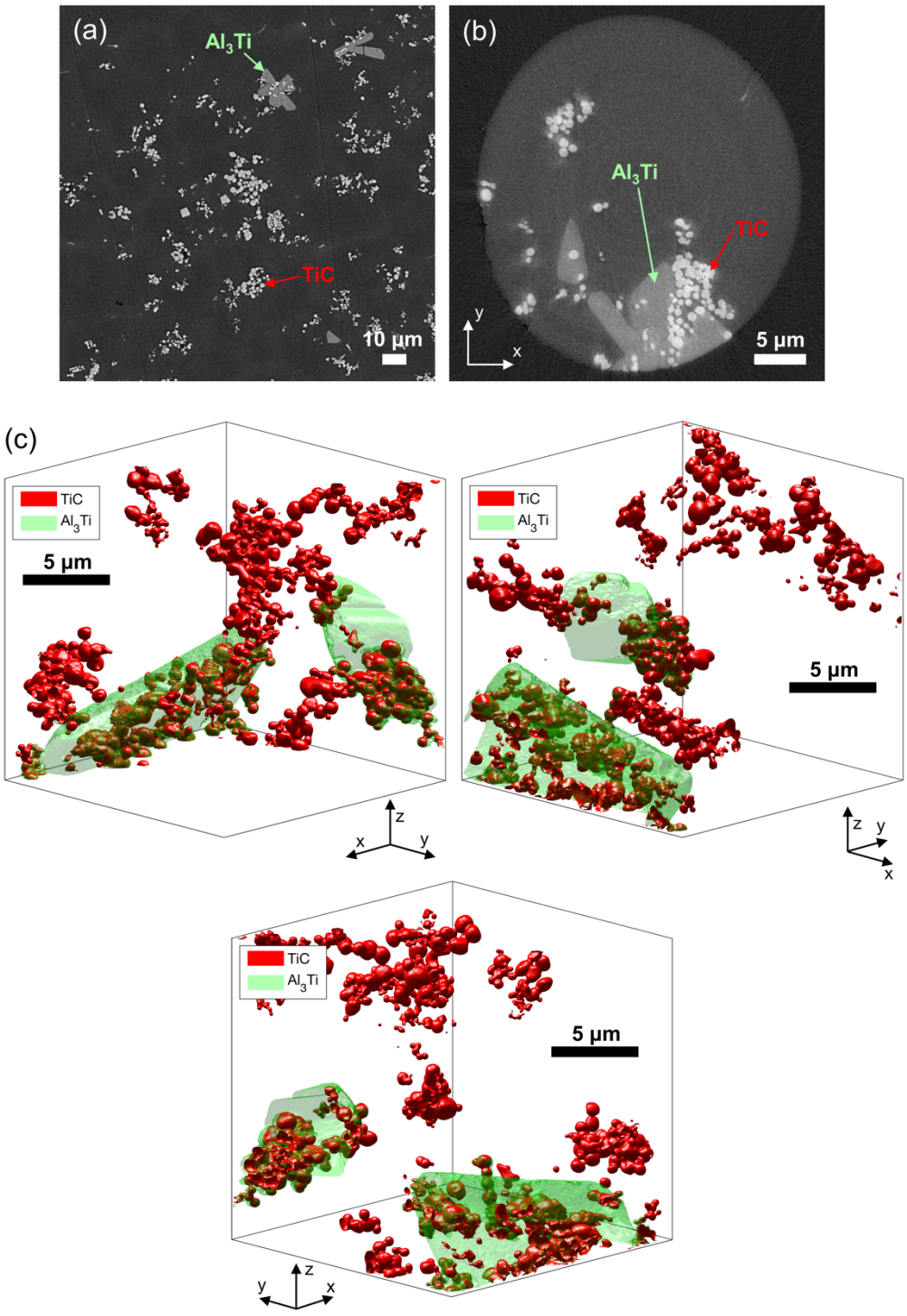

Figure 4.2. Microstructural observations: (a) Representative contrast-adjusted SEM micrograph used for image analysis of particles and secondary phases. Both TiC and Al_3Ti intermetallics are present. (b) Representative reconstructed slice (taken along the tomographic axis-of-rotation, $\hat{z}$) of a micropillar showing both TiC and Al_3Ti phases. The round slice shape corresponds to the diameter of the micropillar, ~35 μm. (c) Volume renderings of a cubic field-of-view within stacked TXM slices. Elongated Al_3Ti (transparent green) is present along with clusters of TiC particles (solid red). Several rotated views are shown for clarity.

4.3 Results and discussion

4.3.1 Microstructural observations

The observed microstructures were discussed in Chapter 3 (Section 3.4.3), but are reiterated here as they are relevant for the discussion in this chapter. SHS microstructures consisted primarily of sub-micrometer TiC particles, with small amounts of Al_3Ti and C-rich regions containing unreacted carbon. Micrographs of representative Al_3Ti, C-rich regions, and TiC particles and their corresponding EDS spectra are shown in Chapter 3, see Figure 3.8(a-c). A small amount of Al_2O_3 (Figure 3.8(d)) was also observed in the bulk. Since this is a byproduct of the reduction of CuO by liquid Al during thermite reaction and not directly related to the Al-Ti-C system under investigation, we do not focus on the Al_2O_3 phase hereafter [154, 183, 184].

The Al_3Ti precipitates (Figure 4.2 and Figure 3.8(a)) exhibit an elongated and faceted structure with dimensions approximately 10-40 μm long and 5-10 μm wide. Small clusters of TiC particles were observed to surround the Al_3Ti in many cases, which becomes more apparent when looking at the reconstructed 3D volumes (Figure 4.2(c)) where TiC particles appear to be attached to the surface of the Al_3Ti (at the spatial resolution of the TXM, 50 nm). The overall volume fraction of Al_3Ti was generally low, with <0.5 vol% per batch (as averaged from all SEM and TXM datasets for a given batch). In a similar sense, the C-rich regions (Figure 3.8(b)) exhibit a layer of TiC or cluster of particles surrounding them (on the order of tens of nm between C-rich regions and the surrounding TiC). Amounts of excess C were difficult to identify reliably *via* image recognition methods due to contrast similarities with pores and any contamination, but in general we observe <0.02 vol% per batch (as averaged from all SEM and TXM datasets for a given batch). We also detected individual TiC particles as well as solid and ring-like clusters, as shown in Figure 3.8(b-c). The particles were largely spheroidal in shape, as confirmed by both SEM and the TXM observations, with some more ellipsoidal shapes also being present. The average TiC yield from SHS was estimated to be in the range of 1-2 vol%, with particle sizes ranging from approximately 380 to 910 nm (as averaged from all SEM and TXM datasets for a given batch). It is also worth noting that although C/TiC and Al_3Ti/TiC features were observed, we did not see instances of C-rich regions in close proximity with Al_3Ti precipitates. Excess C and Al_3Ti were separated by distances on the order of tens of microns.

4.3.2 Thermodynamics of TiC formation

In the CuO-assisted SHS process, the highly exothermic thermite reaction is thought to facilitate the high local temperatures typically needed for TiC formation but estimates as to the peak reaction temperature vary. Theoretical calculations by Fischer and Grubelich [185] report an adiabatic peak reaction temperature of ~2800 K (2527 °C) accounting for phase change of the reaction products, while Lee *et. al.* [183] used a Gibbs formulation model [186] to predict a peak temperature of ~4500 K (4227 °C) in liquid aluminum. Experimental measurements indicate that peak reaction temperatures are dependent on bulk melt temperature, with a peak temperature of 1300 K (1027 °C) for a bulk temperature of 1023 K (750°C) and 2000 K (1727°C) for a bulk temperature of 1193 K (920°C) [38]. Discrepancies in the experimental values are likely due to difficulties in measuring highly localized and transient thermal fields, as well as local variations in thermal conductivity in the pellet/melt system. Therefore, it is worth considering the thermodynamics of the SHS process over a relatively large temperature range to adequately account for bulk and peak temperatures.

TiC can form *via* SHS reaction according to indirect or direct reaction pathways [38]. *Indirect* formation of TiC can occur by reaction between solutes and intermediate compounds, as given by

$$3[Ti] + Al_4C_3(s) = 3TiC(s) + 4Al(l), \tag{4.1}$$

$$[C] + Al_3Ti(s) = TiC(s) + 3Al(l), \tag{4.2}$$

or by solid-solid reactions between Ti- and C-based intermediate compounds,

$$C(s) + Al_3Ti(s) = TiC(s) + 3Al(l), \tag{4.3}$$

$$3Al_3Ti(s) + Al_4C_3(s) = 3TiC(s) + 13Al(s). \tag{4.4}$$

Alternatively, TiC can also be formed *directly via* solute-solute reaction or solute-precursor C reaction,

$$[Ti] + [C] = TiC(s), \tag{4.5}$$

$$[Ti] + C(s) = TiC(s). \tag{4.6}$$

Following Rapp and Zheng [187], we plot the Gibbs free energies of the various chemical reactions as well as solute generation from Ti and C sources for comparison in Figure 4.3(a-b). Several of the energy lines have been truncated based on the stable temperature ranges of the compounds involved in indirect reaction processes (*e.g.* the lines involving $Al_3Ti(s)$ are truncated approximately at its melting temperature). All reactions appear thermodynamically favorable over

the range of relevant temperatures, offering the possibility of multiple pathways in the formation of TiC (Figure 4.3(a)). However, the generation of [C] solutes necessary for Eqns. (4.2 and (4.5) requires temperatures in excess of ~1500 K (1227 °C).

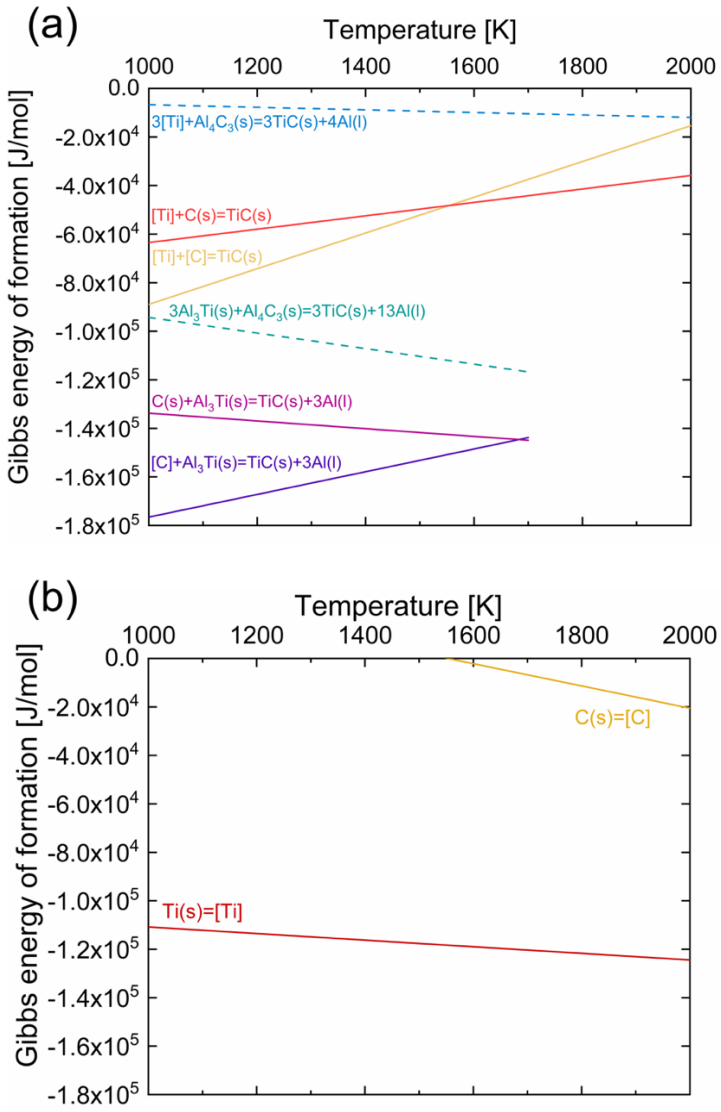

Figure 4.3. Thermodynamic analysis based on equations from Rapp and Zheng [187]: (a) Gibbs energies of formation for the various SHS reaction pathways over an operating temperature range covering bulk melt temperature and peak thermite reaction temperature. "Direct" reaction pathways are warm colored lines, "indirect" reaction pathways are cool colored lines. Dotted lines represent those reaction pathways that are ruled out as unlikely (see text for details). Some lines have been truncated based on maximum limits of phase stability. (b) Gibbs energies of formation for C and Ti solutes ([C] and [Ti]).

4.3.3 Discussion of TiC formation pathways

The observed microstructural signatures and thermodynamics allow us to infer the dominant reaction pathways for TiC formation. The presence of Al_3Ti and the aforementioned TiC clustering around Al_3Ti (Figure 4.2(c)) are suggestive of reaction by Eqns. (4.2) and (4.3). It is possible that the close proximity is due to both particles and intermetallics being pushed during solidification, but it may also be indicative of particle growth from the intermetallics themselves. Similar clustering behavior has been observed previously and attributed to both Al_3Ti-based reaction pathways [38, 39, 41, 188]. However, reaction *via* Eqn. (4.2) may be more favorable than Eqn. (4.3), as the solid-solid reaction has been observed to occur over relatively long time scales (on the order of hours for TiC formation from C and Al-Ti intermetallics) [189]. Furthermore, solid-solid reaction processes are expected to be heavily dependent on the surface contact area between the two solid phases [190], which may be impacted by factors such as localized turbulence in the melt during the self-propagating reaction. The lack of observed Al_3Ti and C in contact with each other, or any indication of partial reaction, would also agree with Eqn. (4.3) either not occurring here or else occurring in a limited capacity.

The observation of TiC particles forming around C-rich regions (Figure 3.8(b)) may be indicative of partial reaction or nucleation sites, thus suggesting that Eqn. (4.6) is also plausible. Numerous observations have been made of TiC surrounding excess C after SHS reaction, and they are often attributed to dissolution of Al_3Ti and subsequent [Ti]-C(s) reaction [38, 152, 174].

Reactions involving Al_4C_3 (Eqns. (4.1 and (4.4)) may be unlikely here, given that it is absent in any of the batches in either a partially reacted or standalone state. Banerji and Reif [191] proposed that Al_4C_3 may be more stable than TiC below temperatures of 1500 K (1227 °C), in which case we would expect residual Al_4C_3, but this was disputed [187, 192] and found to be valid only for very low levels of dissolved Ti. It is likely that the concentration of dissolved Ti is higher than the concentration of dissolved C in the melt during processing, considering the more favorable dissolution of Ti (Figure 4.3(b)) over the operative temperature range. Additionally, the highest thermite reaction temperatures (>1500 K) are required to initiate any C dissolution and, despite discrepancies in the peak reaction temperature, the heat around a CuO reaction site dissipates rapidly (~ 1 ms) [183, 184]. Furthermore, on the Al-rich side of the phase diagram and at concentrations of high Ti relative to C, the Al_4C_3 phase does not co-exist with TiC, Al_3Ti, and

liquid Al [156]. Therefore, reaction pathways involving Al_4C_3 are improbable or limited as compared with other mechanisms.

The direct reaction of [Ti] and [C] in Eqn. (4.5), is difficult to confirm or rule out directly, as no residual evidence of the reaction would be expected or observed. However, Eqn. (4.5) becomes thermodynamically favorable at high temperatures where the dissolution of C is facilitated [38]. It is possible that the particle clusters observed (Figure 3.8(c)), without C-rich regions present, are suggestive of the direct [Ti]-[C] mechanism occurring with a higher frequency in localized regions around thermite reaction sites. Additionally, individual TiC particles observed separate from other solid phases or clusters may also be the result of reaction *via* Eqn. (4.5), occurring when isolated solutes interact after diffusing away from reaction sites.

Figure 4.4 is a schematic that surveys the dominant formation mechanisms of TiC. In the process, the compacted pellet consisting of Al-Ti-C-CuO powders is plunged directly into an Al melt between 1043 K (770 °C) and 1133 K (860 °C). Subsequently, Al powders will begin to melt and react with the solid Ti particles and begin to form Al_3Ti, which is expected at these temperatures even in the absence of thermite [193, 194, 195]. The liquid Al will then reduce the CuO thermite, quickly increasing the local temperature upwards of 1500 K (1227 °C). Al_3Ti (s) and C (s) will subsequently break down and form dissolved [Ti] and [C] in the melt near the thermite reaction sites. At this point [C], [Ti], Al_3Ti(s), and C(s) co-exist in the melt and three reaction pathways can take place in series or in parallel according to Eqns. (4.2), (4.5) and (4.6). Consequently, we expect to see a final microstructure consisting of TiC particles (both individual and clustered), Al_3Ti intermetallics, and excess C-rich regions.

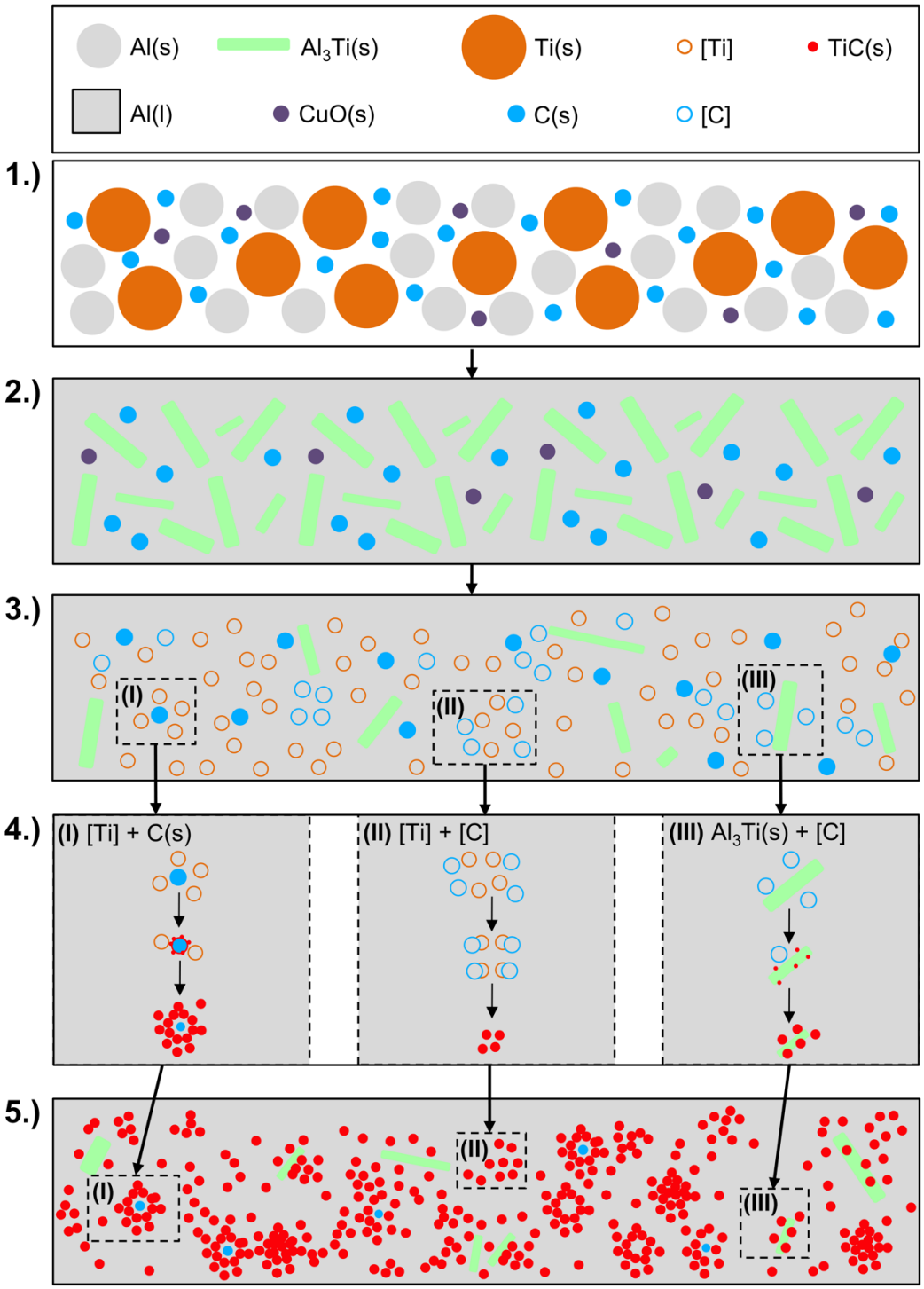

Figure 4.4. Schematic depicting formation mechanisms of TiC via thermite-assisted SHS reactions. Upon insertion of a pellet to the melt (1), Al melts and forms intermediate Al3Ti precipitates (2). The CuO thermite subsequently reacts with liquid Al and a sharp temperature increase (>1500 K) causes dissolution of solid C particles and Al_3Ti precipitates (3). TiC formation then occurs via one of three parallel reaction pathways (4), yielding distinct microstructural signatures (5). All suggested pathways are consistent with experimental observations (*cf.* Figures 3.8(a-c) and 4.2(c)).

4.4 Canonical correlation analysis (CCA)

4.4.1 Motivation

To assist in reconciling the wide variety of processing conditions (Table 4.1), microstructural observations (Figure 3.8(a-c), 4.2), and potential formation pathways (Figure 4.4), we conducted a canonical correlation analysis (CCA). Broadly, CCA is a multivariate statistical model used to study linear associations between two sets of variables *via* analysis of the cross-covariance matrices [196]. As compared with multiple regression, CCA has the advantage of being able to handle multiple dependent variables simultaneously [196, 197]. The methodology of CCA has been discussed in detail elsewhere [196, 197, 198, 199, 200, 201, 202], but will be briefly described here for the purpose of defining key terms.

CCA assumes a set of x_i input and y_j output variables,

$$\vec{X} = \{x_1, x_2, x_3, \dots x_i\}, \tag{4.7}$$

$$\vec{Y} = \{y_1, y_2, y_3, \dots y_j\}, \tag{4.8}$$

where subscripts i and j correspond to the number of input and output variables respectively. Ultimately, CCA seeks to identify linear combinations (up to a maximum of $i = j$) of artificial variables, otherwise known as *canonical variates*, that exhibit maximum correlations (*canonical correlations*). Canonical variates are denoted as

$$V = \sum_i \alpha_i x_i, \tag{4.9}$$

$$W = \sum_j \beta_j y_j, \tag{4.10}$$

where V and W are the canonical variates and α and β are weighted coefficients, known as canonical weights. Effectively, the *weights* used in the canonical variates represent the relative contributions of each independent variable to the dependent variables, at a maximized canonical correlation. Additional quantities of interest for our analysis include the canonical loadings (or cross-loadings), and the redundancy indices [196]. The canonical *loadings* and *cross-loadings* are a measure of the correlation between the original variables used in the analysis and the canonical variates [203]. *Redundancy indices* provide a means of interpreting the shared variance of the canonical variates (*i.e.*, r^2). Thus, to assess the overall "goodness" of the analysis and interpret the results, all of these factors must be considered holistically. Standard statistical significance testing can also be used to aid in interpretation and evaluation of robustness of the CCA results (such as the Wilks-Lambda significance test) [196, 197, 198].

4.4.2 Parameters and definitions

Setting up the CCA requires addressing several assumptions and limitations of the model, such as sample size, variable co-linearity, and canonical variate linearity. Requirements for minimum number of observations (sample size) vary, with guidelines ranging from 10 times the number of model variables [196, 204], >200 observations [205, 206], and >500 observations [203]. Here we use a sample size of 200 observations (20 times the number of variables) corresponding to both SEM and TXM datasets (where one observation represents complete particle and intermetallic statistics for a single SEM image or TXM volume, taken from different locations of ingots from each batch). CCA also assumes that input and output model variables are not co-linear within their respective sets [196]. This is an important consideration when choosing the output metrics, since dispersion and agglomeration can be used to calculate average particle diameter and volume percentage. Thus, these two sets of metrics were kept as separate groups during evaluation. Finally, it is worth noting that CCA is designed to highlight *linear* relationships between combinations of independent and dependent variables [196, 197, 199]. If the relationships are not linear, CCA may not accurately capture them and supplementing with additional techniques like Monte Carlo analysis may be required [202]. However, the information obtained from CCA can still be quite valuable if care is taken during interpretation of the results [196].

Taking the assumptions and limitations of CCA into account, below we define our input and output variables. For input metrics $\vec{X}$, we use the processing parameters (from Table 4.1): bulk melt temperature (T_{proc}), C and CuO pellet composition (n_C, n_{CuO}), Ti precursor size (d_{Ti}), pellet packing method, powder mixing method, and powder/melt mass ratio ($r_{p/m}$). For the output metrics, we define two separate canonical variates (denoted as $\vec{Y}_1$ and $\vec{Y}_2$) in order to avoid the problem of multicollinearity [196] between the dependent variables. For $\vec{Y}_1$, we choose volume percentage of TiC (v_{TiC}), average diameter of TiC particles (d_{TiC}), and volume percentage of Al_3Ti intermetallic phases (v_{Al_3Ti}). The choice of output metrics here is based on our microstructural observations (Figure 3.8(a-c)) with the goal of informing process parameters in tuning TiC characteristics. Although volume percentage of excess C (Figure 3.8(b)) was also an observed microstructural feature, it was not included here due to the very low volumes relative to TiC and Al_3Ti (<0.02 vol% based on an average of all SEM and TXM datasets for a given batch). The second grouping of relevant output metrics, $\vec{Y}_2$, consisted of dispersion (D), agglomeration (A),

and Al_3Ti volume percentage (υ_{Al_3Ti}). The rationale behind this particular set of variables was to provide some indication as to whether different processing conditions lead to different reaction pathways (*e.g.*, TiC formed *via* [Ti]-[C] may be more dispersed, whereas agglomerated TiC or high Al_3Ti vol% may indicate more solid-solute mediated reaction mechanisms). Additionally, dispersion and agglomeration are microstructural features of interest due to their strong influence on the overall mechanical performance of MMNCs [122, 124, 207, 208, 209].

Dispersion, D, and agglomeration, A, were calculated for each 2D/3D dataset using the approach developed by Tyson *et al.* [210]. First probability density functions (PDFs, denoted as f in the equations that follow) were created from the distributions of particle diameters and interparticle spacings in the image [211]. Then, D and A were calculated as,

$$\mathrm{D} = \int_{0.8\mu}^{1.2\mu} \mathrm{f}(\mathrm{r_{TiC\text{-}TiC}})\mathrm{dr}, \tag{4.11}$$

$$\mathrm{A} = 1\text{-} \int_{0.7\mu}^{1.3\mu} \mathrm{f}(\mathrm{d_{TiC}})\mathrm{dd}, \tag{4.12}$$

where $r_{TiC-TiC}$ is the nearest-neighbor interparticle spacing, d_{TiC} is the particle diameter, and μ is the mean value of each corresponding PDF. In the limit the particles are perfectly disperse and not clustered, $D = 1$ and $A = 0$ (and *vice versa* in the opposite limit). A graphical representation of how dispersion and agglomeration are calculated is shown in Figure 4.5(a-b), for a representative high-magnification SEM image.

CCA was carried out using the *CCA* package developed by González *et. al.* [212] for the R statistical computing environment (version 3.6.0). We used a sample size of 200 observations (*i.e.*, 20 times the number of variables) corresponding to both SEM and TXM datasets (where one observation represents complete particle and intermetallic statistics for a single SEM image or TXM volume, taken from different locations of ingots from each batch). The CCA input data (*e.g.* particle diameter, volume percentage, *etc.*) was compiled from calculations using the image processing methods described in Section 4.2.2.

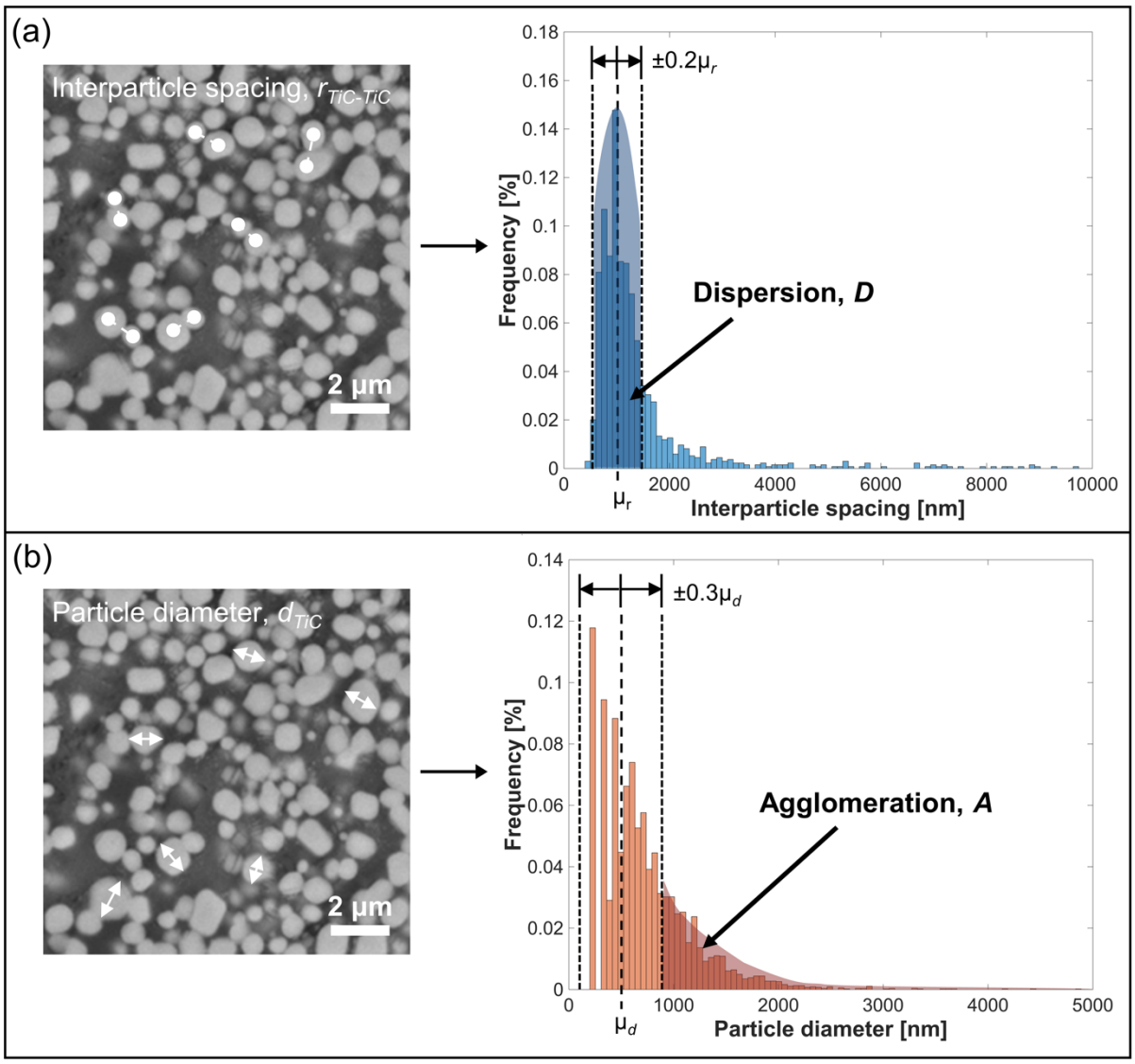

Figure 4.5. (a) Example calculation of particle dispersion, *D*, based on a corresponding probability distribution function of interparticle spacings. (b) Example calculation of particle agglomeration, *A*, based on a corresponding probability distribution function of particle diameters. SEM images at left are high-magnification representations to more clearly show the definitions of interparticle spacing and diameter (lower magnification images are used to construct the PDFs so that a sufficient number of particles can be captured). In general, >1200 particles are considered in constructing the probability distributions. See text for computational details.

4.4.3 CCA results and discussion

CCA evaluation of the first group of variables $\vec{Y}_1$ using ν_{TiC}, d_{TiC}, and ν_{Al_3Ti} as the dependent variables yield linear combinations with correlation coefficients of 0.74, 0.18, and 0.11. The relative differences between the coefficients, as well as a redundancy index analysis, suggest that the first pair of canonical variates is sufficient to describe the data. A table of the relevant

results for the first canonical variate pair is shown in Table 4.2 and the variates are plotted together in Figure 4.6 (SEM data in blue and TXM data in red). A least-squares fit to the data and the relatively high correlation coefficient suggest that the behavior of the dependent variate, W, is reasonably well described by the independent variate, V. A Wilks-Lambda test yields $p < 0.001$, indicating the results are statistically significant. A graphical representation of the absolute value of the loadings and weights for each variable is shown in Figure 4.7, where the relative diameters of the circles correspond to the variance (squared loadings). Variables with high weights and significant loadings (≥ 0.40 for sample sizes of at least 200 [196, 203]) are considered to dominate the behavior of the variate. Thus, the dominant variables for further consideration can be reduced to the independent variables n_C, $r_{p/m}$, and the dependent variable ν_{TiC}.

Table 4.2. Summary of the CCA analysis using TiC particle volume percentage (v_{TiC}) , TiC particle diameter (d_{TiC}), and Al_3Ti intermetallic volume percentage (v_{Al_3Ti}) (metric set $\vec{Y}_1$) as the dependent variables for the output metrics. The input variable metrics are bulk melt temperature (T_{proc}), C and CuO pellet composition (n_C, n_{CuO}), Ti precursor size (d_{Ti}), pellet packing method, powder mixing method, and powder/melt mass ratio ($r_{p/m}$). Note that the redundancy indices apply to all the inputs (for 0.401) and outputs (for 0.275).

Variable	Weight	Loading	Cross-loading	Redundancy Index
T_{proc}	0.032	0.888	0.761	
n_C	−5.290	−0.651	−0.558	
n_{CuO}	16.152	−0.386	−0.331	
d_{Ti}	0.031	0.869	0.745	0.401
$r_{p/m}$	−3.839	0.811	0.696	
Pellet packing	0.622	0.643	0.551	
Mixing method	−0.138	−0.794	−0.680	
V_{TiC}	1.133	0.999	0.857	
d_{TiC}	−0.0001	0.336	0.288	0.275
V_{Al_3Ti}	−0.068	0.096	0.083	

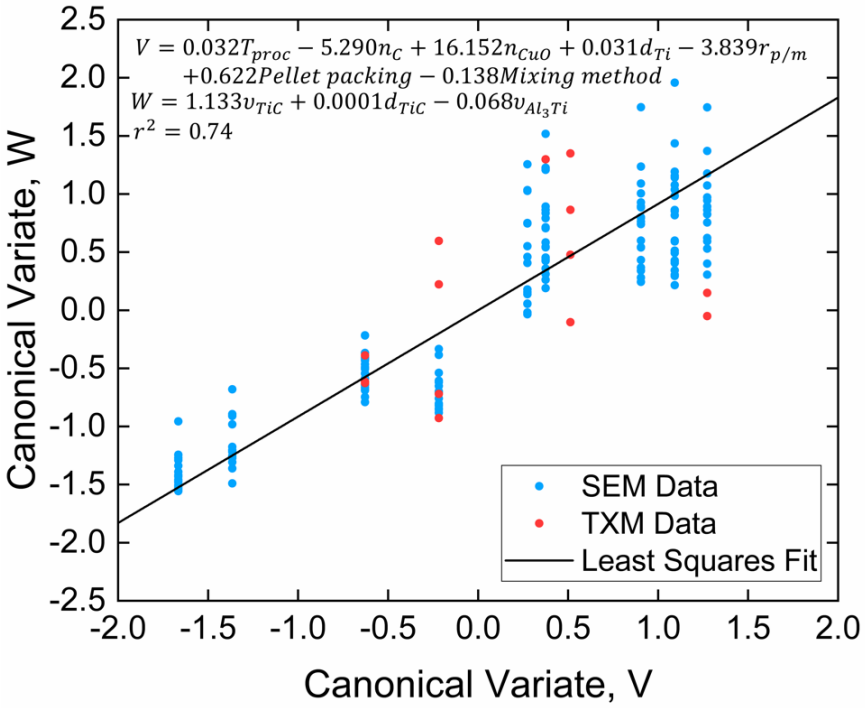

Figure 4.6. Correlation of the canonical variates using the output metrics v_{TiC} , d_{TiC}, and v_{Al_3Ti} (metric set $\vec{Y}_1$) in canonical variate W. Data points are colored according to the experimental probe used to capture the microstructure (either SEM or TXM, see Figure 3.8 and Figure 4.1). The associated canonical weights of each variate and the canonical correlation coefficient are shown at the top left.

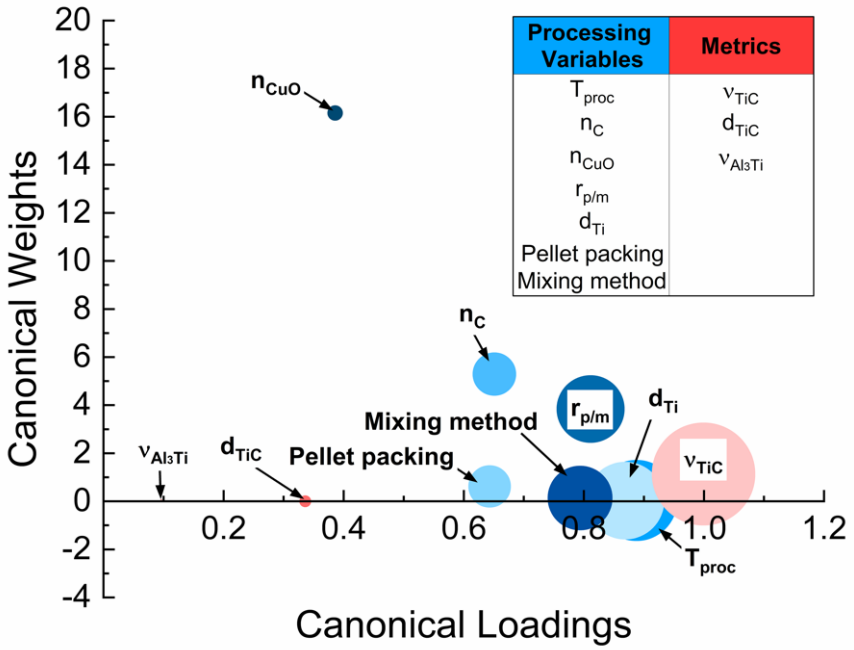

Figure 4.7. Graphical representation of the CCA-determined weights and loadings (of the first canonical variate pair) using ν_{TiC} , d_{TiC}, and υ_{Al_3Ti} (metric set $\vec{Y}_1$) as the output metrics. The diameter of each circle corresponds to the fraction of the variance associated with each variable (squared loadings). Relatively higher weights and loadings for n_C and $r_{p/m}$ indicate that they explain a larger fraction of the canonical variate of processing variables, V. The relatively higher loading for ν_{TiC} indicates that it explains a large fraction of the canonical variate of output metrics, W. A more detailed list of the CCA outputs is found in Table 4.2.

CCA evaluation of the second group of variables $\vec{Y}_2$ with D, A, and ν_{Al_3Ti} as dependent variables yield linear combinations with correlation coefficients of 0.82, 0.42, and 0.15 for the first, second, and third canonical variate pairs respectively. Similar to the first group of metrics, we assume the first canonical variate pair is sufficient for interpretation of the CCA based on the relative magnitudes of r^2 and a redundancy index analysis. A Wilks-Lambda test suggests the first canonical correlation is statistically significant, yielding $p < 0.001$. A summary of the relevant results for the first variate pair is shown in Table 4.3 and a least-squares fit and the correlation coefficient suggest that W is well described by V (Figure 4.8). A graphical representation of the absolute value of the loadings and weights for each variable is shown in Figure 4.9. Based on the significant weights and loadings, the independent variables n_{CuO}, n_C, and $r_{p/m}$ dominate the behavior of V, while the behavior of W is not observed to be dominated by a specific variable (although D exhibits the highest weight and loading).

Table 4.3. Summary of the CCA analysis using particle dispersion (D), particle agglomeration (A), and volume percentage of Al_3Ti intermetallics (v_{Al_3Ti}) (metric set $\vec{Y}_2$) as the dependent variables for the output metrics. The input variable metrics are bulk melt temperature (T_{proc}), C and CuO pellet composition (n_C, n_{CuO}), Ti precursor size (d_{Ti}), pellet packing method, powder mixing method, and powder/melt mass ratio ($r_{p/m}$). Note that the redundancy indices apply to all the inputs (for 0.445) and outputs (for 0.180).

Variable	Weight	Loading	Cross-loading	Redundancy Index
T_{proc}	−0.012	0.902	0.816	
n_C	1.066	−0.488	−0.441	
n_{CuO}	−19.547	−0.855	−0.773	
d_{Ti}	0.044	0.931	0.842	0.445
$r_{p/m}$	4.920	0.787	0.711	
Pellet packing	−0.218	0.563	0.509	
Mixing method	−0.233	−0.475	−0.430	
D	0.103	0.639	0.577	
A	0.092	0.461	0.416	0.180
v_{Al_3Ti}	0.174	0.198	0.179	

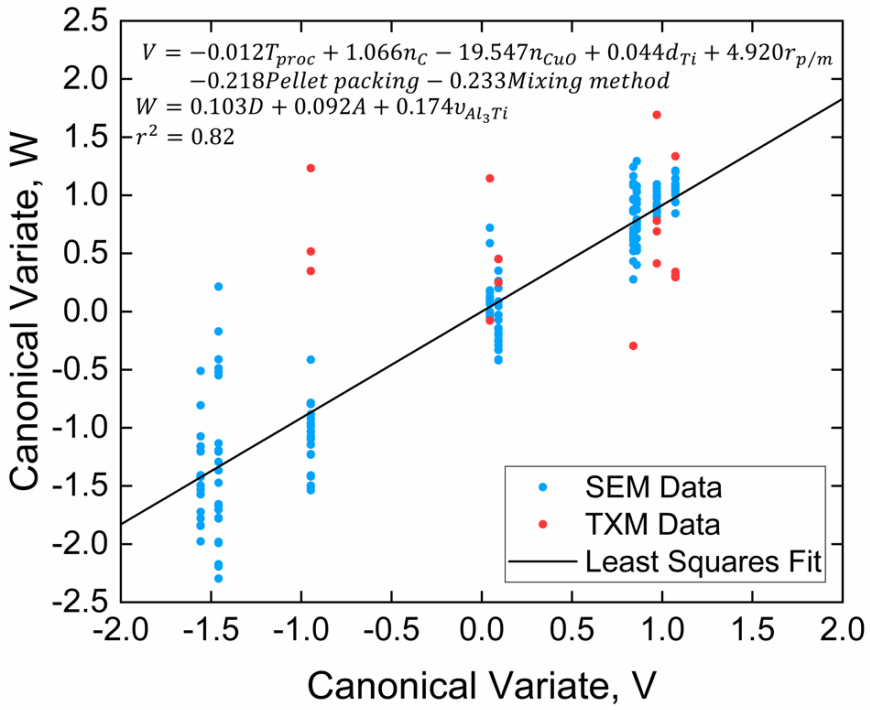

Figure 4.8. Correlation plot of the canonical variates using the output metrics D, A, and v_{Al_3Ti} (metric set $\vec{Y}_2$) in canonical variate W. Data points are colored according to the experimental probe used to capture the microstructure (either SEM or TXM, see Figure 3.8 and Figure 4.1). The associated canonical weights of each variate and the correlation coefficient are shown at top left.

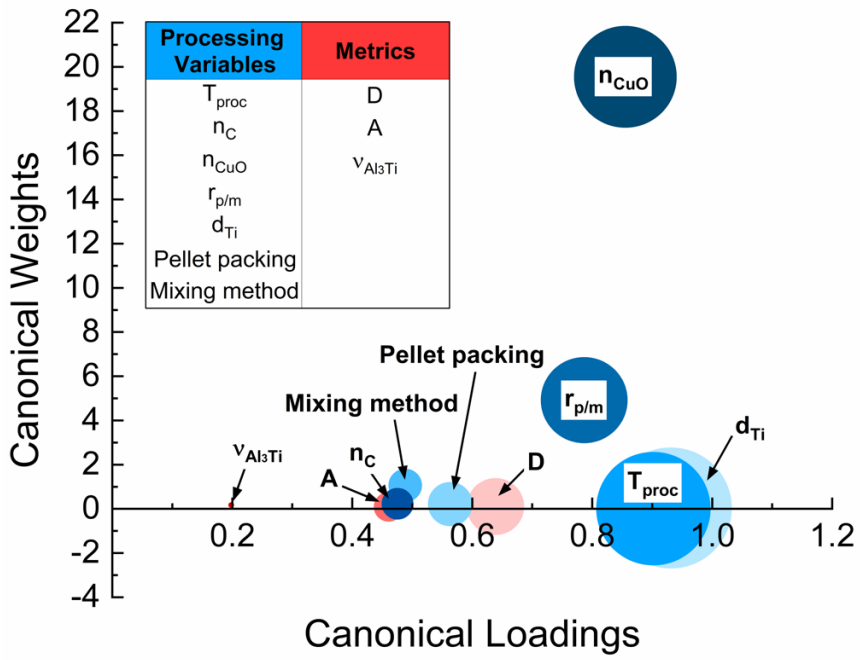

Figure 4.9. Graphical representation of the CCA determined weights and loadings (of the second canonical variate pair) using D, A, and v_{Al_3Ti} (metric set $\vec{Y}_2$) as the output metrics. The diameter of each circle corresponds to the fraction of the variance associated with each variable (squared loadings). Relatively higher weights and loadings for n_{CuO}, n_C and $r_{p/m}$ indicate that they explain a large fraction of the canonical variate of processing variables, V, in agreement with results obtained from the other canonical variate pair (Fig. 4.7). The relatively similar weights and sufficiently high loadings of dispersion and agglomeration indicate that they explain roughly equal fractions of the canonical variate of output metrics, W. A more detailed list of the CCA outputs is found in Table 4.3.

The results of both CCAs suggest that the amount of precursor powder (n_C and $r_{p/m}$) and the amount of thermite, n_{CuO}, have the largest impact on the final microstructure (*e.g.*, TiC characteristics and distribution). Several of the variables in the independent variate $\vec{X}$ (T_{proc}, d_{Ti}, pellet packing method, and powder mixing method) exhibit a high loading, but low weight (relative to the dominant variables). This suggests that these variables are accurately captured by the independent variates and that the dependent variates $\vec{Y}_1$ and $\vec{Y}_2$ are weakly sensitive to variations in these inputs. The relatively low weights calculated for the dependent variates in both CCAs may stem from non-linear relationships between the outputs and the inputs that may be more accurately captured by supplementary methods such as a Monte Carlo analysis [202]. Nevertheless, the high correlation coefficients between the variates in both CCAs suggest a measure of sensitivity in the output variables to the dominant input variables.

The results of the CCA are in agreement with our microstructural observations and the thermodynamics of TiC formation (Section 4.3.3), suggesting that the amount of C and CuO have the largest impact (relative to the other processing variables) on the final microstructure. In our schematic (Figure 4.4) of formation mechanisms, we proposed three dominant reaction pathways (all requiring C) consisting of TiC formation *via* direct mechanisms (*i.e.*, [Ti] and [C] or solid C interactions, Figure 3.8b-c) and an indirect mechanism (*i.e.*, [C] with Al_3Ti, Figure 3.8(a) and Figure 4.2(c)). However, based on the thermodynamics (Figure 4.3(a-b)), it is expected that only the reaction pathway involving [Ti] and solid C will be favorable below temperatures of ~1500 K (1227 °C). Thus, the amount of CuO will play a dominant role in TiC formation as the high temperatures required for [C] dissolution and initiation of the other two formation pathways (*i*.e., [Ti]-[C] and [C]-Al_3Ti) are dependent on the availability of thermite reaction sites. Given that the three pathways exhibit distinct microstructural signatures, tuning the characteristics of the CuO (*e.g.*, amount, particle size, distribution within the pellet) may provide a more effective measure of microstructural control.

4.4.4 Considerations of morphological evolution

The combined CCA and microstructural data shown above provide a holistic view of the key processing variables and hypothetical reaction pathways for the formation of TiC. We have not yet considered on a more local scale the morphological evolution of individual phases *via* each pathway, which can also have a significant impact on physical properties. In particular, the shape of the reinforcing and secondary phases (*e.g.*, the TiC particles and Al_3Ti intermetallic here) have been found to strongly affect the mechanical performance of the material [135, 144, 145].

The TiC particles observed here (See Figure 3.8 and Figure 4.2) are typically spheroidal or nearly spheroidal (*e.g.*, ellipsoidal) in shape. Jin *et. al.* [213, 214], Dong *et. al.* [215], and Zhang *et. al.* [216] have demonstrated that the shape of TiC is heavily influenced by the stoichiometric ratio of C/Ti, where a perfect sphere corresponds to C/Ti ~1.0 and sub-stoichiometric ratios of C/Ti can lead to cubic (C/Ti > 1.0), ellipsoidal (C/Ti < 1.0), or octahedral (C/Ti $\ll$ 1.0) morphologies. Particles corresponding to C/Ti stoichiometry close to 1.0 would be in good agreement with the morphologies observed here (See Figure 3.8(c)). The presence of some ellipsoidal particles corresponding to C/Ti < 1.0 (*i.e.,* $TiC_{x<1}$) may be due to instances of particle formation that are C limited (*e.g.*, reaction *via* Eqn. (4.5)). However, it is also possible that some

of these ellipsoidal particles may change to spherical over time. Previous studies of TiC formation in Al *via* SHS reaction have observed particle evolution from octahedral to ellipsoidal and spherical, owing to a thermodynamic roughening transition from (111) stable particle surfaces to (100) stable surfaces [213, 215].

Similarly, the Al_3Ti morphology has been shown to be highly sensitive to processing conditions, with primarily either the blocky/platelet-like (both elongated and equiaxed) or needle-like flakey morphologies forming based on melt processing temperature, cooling rate, and Ti concentration [217, 218, 219, 220, 221]. The Al_3Ti intermetallics in this study exhibit an elongated shape with some degree of faceting at the ends (See Figure 3.8(a) and Figure 4.2(c)). Faceting is likely a characteristic of platelet-type Al_3Ti, which has been observed to form at relatively low processing temperatures (as low as ~730 °C) [193, 217, 222]. Observed platelets may be consistent with formation by reaction between the surrounding liquid Al, melting Al powders, and solid Ti powders when the pellets are introduced into the melt (between 770-860 °C in this study). Alternatively, Zhao *et. al*. [223] and Arnberg *et. al.* [217] have attributed the blocky faceted formation to a local supersaturation of Ti. This explanation may also be feasible, given that high local Ti concentrations arise following CuO reaction and melting of nearby Ti powders. In general, elongated faceted intermetallics are suggestive of anisotropic growth, which has been hypothesized to occur preferentially in the <110> direction due to nucleation on lowest density atomic planes [218, 224, 225].

For both TiC particles and Al_3Ti intermetallics, different morphological evolution pathways may still lead to the same morphologies in the final microstructure (*e.g.*, direct formation of spherical TiC particles *versus* roughening transitioning from octahedral to spherical particles). However, each pathway may be sensitive to the processing conditions and occur at different or competing rates; such intermediate steps cannot be accessed using the present analysis. To supplement our investigation, a complimentary approach such as phase field modeling [226, 227] or reaction-diffusion modeling [228] of SHS reaction would be illuminating. *In situ* studies of microstructure formation (through, *e.g.*, TXM [229]) would also help validate and refine these models. The time-resolved experiments and models would provide a more complete picture of the morphological evolution underlying complex reactive processes.

4.5 Conclusions

In this chapter, we have performed a more detailed investigation of formation mechanisms and processing-property relationships for *in situ* Al-TiC MMNCs produced *via* CuO-assisted SHS. A variety of SHS processing conditions were studied and the microstructures were characterized by both SEM and TXM (2D and 3D) to better understand TiC particle formation. By corroborating the microstructural data with thermodynamic analyses, we have proposed a formation mechanism for SHS TiC consisting of three reaction pathways (*i.e.*, [Ti] + [C], [Ti] + C(s), and [C] + Al_3Ti(s)) that lead to distinct microstructural signatures. We have also conducted CCA on the data collected in our study and demonstrated its potential as a means of guiding processing parameter choice for production of SHS MMNCs. In particular, for the CuO-assisted SHS process, we find that the amount of CuO thermite has the largest impact on final microstructural characteristics, likely due to the fact that two of three proposed reaction pathways require the high local temperatures generated by the thermite reduction. The results of this study on the formation mechanisms and processing input/output relationships will inform future SHS experiments and the rational design of *in situ* SHS MMNCs.

CHAPTER 5

Summary, Preliminary Flux-Assisted Reaction Experiments, and Suggestions for Future Work

5.1 Dissertation summary

Metal matrix nanocomposites (MMNCs) are a promising route for achieving improved ambient and elevated temperature mechanical performance of lightweight metals, such as Al. Typical *ex situ* MMNC processing methods, where the reinforcing particles are added to the matrix after manufacturing elsewhere, can suffer from incorporation difficulties due to contamination and undesirable particle/matrix interfacial reactions, reducing their viability for commercial scale-up. Alternatively, *in situ* processing methods, where particles are created directly in the melt *via* reactive pathways, exhibit improved particle/matrix interface stability and easier potential scalability. However, as the particles are created *in situ*, process control over critical particle characteristics (*e.g.*, diameter, volume fraction, dispersion) are not well understood and remain a barrier to scale-up efforts. Consequently, this dissertation work sought to investigate processing-microstructure-mechanical property relationships and formation mechanisms for *in situ* MMNCs, with the purpose of informing efforts to process commercial pilot-scale amounts of material.

In Chapter 2, we discussed the necessary literature and background for better understanding processing control of MMNCs, including pros and cons of various processing approaches, the strengthening mechanisms underlying their improved mechanical performance, and key particle characteristics to be controlled. This review provides a framework for the work studied in Chapter 3 and Chapter 4 of this dissertation.

In Chapter 3, we studied microstructural and mechanical properties of MMNCs processed *via* two *in situ* methods, namely, *in situ* gas-liquid reaction (ISGR) and self-propagating high-temperature synthesis (SHS). We found that a modified CuO thermite-assisted SHS process in particular is capable of readily producing sub-micrometer TiC particles in a wide variety of volume fractions and dispersions depending on processing conditions. Working jointly with a team as part of the Lightweight Innovations for Tomorrow (LIFT) Institute, we report successful SHS

processing of commercial pilot-scale quantities of *in situ* Al-TiC MMNCs (~30 lbs), which exhibit a 26% increase in yield strength and 50% increase in ultimate tensile strength for relatively low amounts of reinforcement addition (0.7 vol% TiC). These results are a promising indication of the SHS process as a commercial-friendly method for large-scale production of *in situ* MMNCs.

The work conducted in Chapter 3 laid the groundwork for our study in Chapter 4, where we performed a more detailed investigation into understanding the particle formation mechanisms and processing-property relationships for the SHS process. By combining 2D and 3D microstructural characterization (*i.e.*, SEM and TXM) with a thermodynamic-based analysis, we identified three probable reaction pathways leading to TiC formation, namely direct reaction between [Ti] and [C] solutes, [Ti] solutes and solid C(s) sources, and [C] solutes with solid Al_3Ti(s) intermetallics. We also demonstrate an approach for correlating processing-property relationships *via* quantitative microstructural analysis and canonical correlation analysis (CCA), where we report that the amount of CuO thermite is the key processing variable affecting final MMNC characteristics of interest (*e.g.*, TiC volume fraction and dispersion). The results presented in this chapter are expected to inform a more rational approach to process control of *in situ* SHS MMNCs.

5.2 Suggestions for future work and research directions

The remainder of this dissertation will focus on suggestions for future work and directions based on the results presented in Chapter 3 and Chapter 4. We also present some preliminary experiments on an alternative MMNC processing method (*i.e.,* flux-assisted reaction synthesis) that were not able to be completed over the course the work presented here, and some suggestions for additional future directions.

5.2.1 Elevated temperature mechanical properties of SHS MMNCs

As discussed in Chapter 1, MMNCs are expected to exhibit improved mechanical properties in the elevated temperature regime (*i.e.*, 250 °C – 350 °C) as compared with other alloy strengthening mechanisms like precipitation strengthening. Consequently, although our reported results in Chapter 3 demonstrated improved ambient temperature mechanical properties of Al-TiC MMNCs, further mechanical testing at these elevated temperatures is necessary to better confirm their potential for commercial structural applications. Improved elevated temperature properties are expected for the MMNCs studied in this dissertation [77, 80, 138], but additional high

temperature tensile testing or hot hardness testing would provide valuable data on the mechanical performance of Al-TiC MMNCs produced *via* SHS.

5.2.2 Influence of Si on SHS MMNCs

Based on the results of the SHS experiments presented in Chapter 3, it is clear that the addition of secondary elements like Si can have a drastic effect on the final MMNC microstructure. During both direct SHS reaction and SHS master alloy dilution in Si-containing A356 (composition: Al-7Si-0.3Mg), we reported on formation of undesirable $TiAl_xSi_y$ intermetallics and Al_4C_3 carbides, which are presumably due to decreased TiC stability in the presence of Si. However, Si-containing Al-alloys such as A356 are of high interest for matrix materials in commercial applications owing to their improved castability [230, 231]. TiC instability and the subsequent formation of $TiAl_xSi_y$ and Al_4C_3 in Si-containing Al alloys have been previously reported [158, 160], but the governing mechanisms are not fully understood. Furthermore, in addition to issues with TiC instability, the formation of these secondary $TiAl_xSi_y$ phases may have negative effects on the general bulk material properties in terms of castability and wear resistance [232, 233]. Consequently, a more detailed study on the influence of Si on the stability and formation of TiC in Al-Si melts would be beneficial for informing scale-up of commercially relevant Al-Si-based alloys.

5.2.3 CCA: Accounting for non-linear variable relationships

In Chapter 4, we demonstrated an approach combining microstructural quantification and CCA to better understand the relationship between processing parameters and final microstructural characteristics. Although our CCA analysis identified some key processing parameters (*i.e.*, amount of CuO) and confirmed the sensitivity of key output characteristics (*i.e.*, dispersion and volume reinforcement percentage) to these processing variables, further work needs to be done to better quantify the relationship between the two. One of the limitations of CCA is the assumption of linear relationships between variables, which may not be the case. To better capture non-linearities in the data, CCA can be supplemented with complimentary techniques such as Monte-Carlo analysis [202] or optimiztation *via* genetic algorithms [234]. Similar techniques may be applied to the SHS microstructural data discussed in Chapter 4, as well as future *in situ* MMNC data sets, which may uncover new processing-property relationships.

5.2.4 Exploration of alternative thermite materials for SHS process

In Chapter 4, our multi-faceted approach utilizing microstructural quantification and CCA identified the CuO thermite as the key processing parameter influencing the reaction pathways and subsequent microstructural signature of thermite-assisted SHS Al-TiC MMNCs. This is likely due to a high localized temperature increase in the constitutent precursor powders, owing to the exothermic reaction after reduction of CuO by the Al melt. The high localized temperature then enables generation of [Ti] and [C] solutes, which can form solid TiC *via* several direct and indirect pathways (See Chapter 4). Given the apparent importance of the localized temperature increase from the thermite, a useful future study would be to explore alternative thermite materials in addition to CuO. For example, titanium dioxide (*i.e.*, TiO_2) has been demonstrated as a viable thermite for TiC production and allowing for the exclusion of pure Ti precursor powders from the SHS pellets [37, 235, 236].

5.2.5 An alternative approach to in situ Al-TiC MMNCs: Flux-assisted reaction synthesis

Based on the results of the CCA analysis in Chapter 4, it is clear that the amount of thermite is a significant processing parameter in controlling the microstructure and particle characteristics of CuO-assisted SHS MMNCs. However, we also find interest in alternative methods of producing *in situ* Al-TiC MMNCs. Based on the analysis of the thermodynamics, reaction pathways, and formation mechanisms in the Al-TiC system presented in Chapter 3, one possible approach involves leveraging the reaction pathway that does not require the high temperatures provided by the CuO reduction, given as Eqn. 5.1,

$$[Ti] + C(s) = TiC(s). \tag{5.1}$$

A promising *in situ* processing method presumed to be based on Eqn. 5.1 involves the use of flux-assisted reaction synthesis, where a Ti-based flux (*i.e.*, dipotassium titanium hexafluoride, K_2TiF_6) acts as a source of [Ti] solute atoms upon decomposition in Al melts [49, 50, 51, 53, 54]. In the flux-assisted process, it is thought that when the K_2TiF_6 is reduced by the Al melt, it releases [Ti] solute atoms, potassium tetrafluoroaluminate and potassium hexafluoroaluminate byproducts according to Eqn. 5.2,

$$3K_2TiF_6(l) + 4Al(l) = 3[Ti] + 3KAlF_4(l) + K_3AlF_6(l). \tag{5.2}$$

The solutal Ti can then either react with the solid C sources, forming a thin layer of TiC at the C/melt interface [49], or induce Al_3Ti intermetallic precipitation when the Ti content exceeds the

melt solubility limit [50]. TiC formation and growth then proceeds owing to the improved wetting of C particles [54] and increased amounts of [Ti] can be supplied to the melt through the dissolution of Al_3Ti [50].

It is hypothesized that as the flux-assisted reaction synthesis approach relies on TiC formation *via* Eqn. (5.1), that the final particle size can be somewhat controlled by the size of the C precursor particles, possibly enabling a more straightforward way for *in situ* reinforcement particle size control. For example, Cao *et. al.* [49] have demonstrated Al-TiC MMNCs with sub-10 nm particles, based on 3-10 nm diamond C, at processing temperatures as low as 820 °C. Consequently, the flux-assisted reaction synthesis process has potential as an alternative scalable, commercial friendly process.

Preliminary experiments on bulk synthesis of Al-TiC MMNCs *via* flux-assisted reaction were conducted. To create flux-powder mixtures, K_2TiF_6 flux (Sigma Aldrich) and ≤10 nm diamond C (SkySpring Nanomaterials) were mixed *via* planetary ball milling for 2-3 hrs at a speed of 300 RPM. To create Al-TiC MMNCs, approximately 350 g of commercial purity Al (P1020 alloy, 99.7% Al) were placed in a graphite crucible and melted at 950 °C in a resistance furnace under Ar atmosphere. After holding the melt at the target temperature for 1 hr to ensure homogenization, flux-C powder mixture was manually loaded onto the melt surface until completely covered. The powder mixture was allowed to dwell and react on the melt surface for 10 min, followed by manual stirring with a BN-coated graphite rod for approximately 1 min and an additional 10 minutes holding time. Subsequently, the melt was removed from the furnace and allowed to solidify under ambient conditions. Metallographic specimens were prepared using standard preparation techniques with a 1 μm diamond finishing step and examined using a Tescan MIRA3 FEG SEM at 15 kV and a beam intensity of 15 (see Section 3.4.2 for more details).

The microstructure of Al-TiC composites processed *via* flux-assisted reaction synthesis consisted of particles approximately 50-60 nm in diameter (See Figure 5.1). Particles were typically clustered at the grain boundaries, possibly due to particle pushing during solidification, which is predicted to require high cooling rates and fast solidification front velocities to ensure effective engulfment as particle sizes approach the sub-500 nm scale [237, 238, 239, 240, 241]. In addition to TiC particles, some amount of Al_3Ti intermetallics and K- or F-based oxides remain as byproducts, which may be undesirable from a mechanical property standpoint.

From these preliminary experiments, it is apparent that sub-100 nm TiC particles are able to be produced from a relatively simple process. Further work on better understanding the processing-property relationships, and a systematic study of C precursor size as a means to control TiC particle size in particular, would be useful to inform scale-up efforts for the flux-assisted reaction synthesis process.

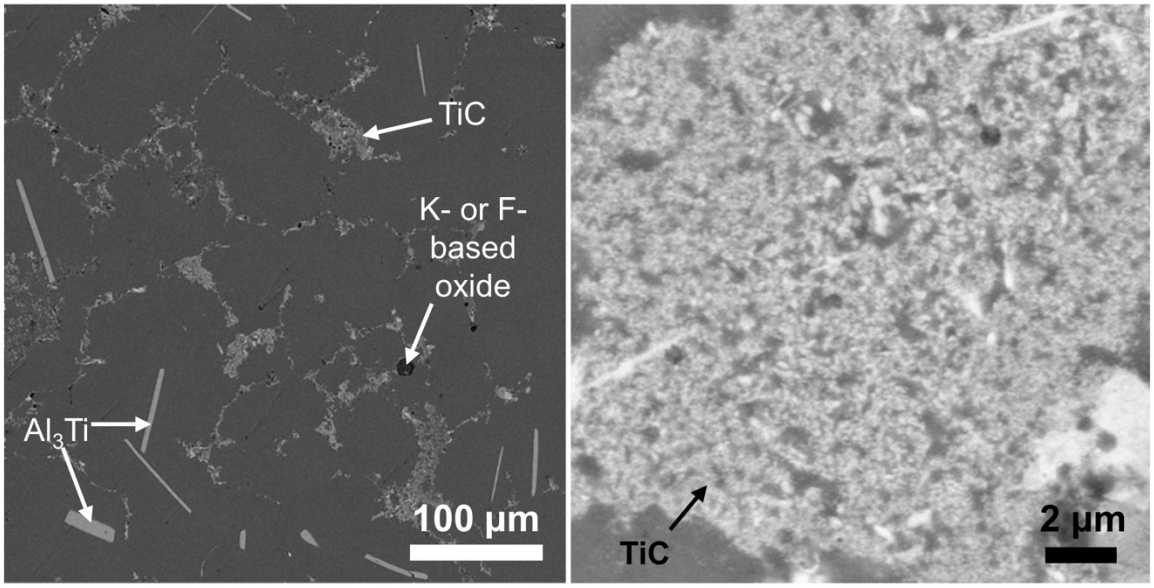

Figure 5.1. (left) SEM micrograph showing microstructure of Al-TiC nanocomposite processed *via* flux-assisted reaction synthesis using K_2TiF_6 and ≤10 nm diamond C precursors. TiC nanoparticles, Al_3Ti intermetallics, and K- and F-based oxides are visible in the microstructure. (right) Higher magnification SEM micrograph showing the TiC nanoparticles with an average diameter of 50-60 nm.

5.2.6 Real-time visualization of in situ MMNC processing: Preliminary experiments on flux-assisted reaction synthesis

To better understand the particle formation mechanisms underlying *in situ* processing approaches, we also seek to explore real-time visualization techniques to supplement *post mortem* sample characterization and thermodynamic analyses (*e.g.*, as used to investigate the SHS reaction in Chapter 4). One such technique is synchrotron X-ray radiography (XRR), a 2D imaging technique where projections are collected for a single sample orientation (*i.e.*, no sample rotation). XRR is advantageous versus 3D synchrotron imaging techniques (*e.g.*, TXM) as the lack of sample rotation allows for improved temporal resolution, which makes it particularly attractive for capturing fast dynamic processes. XRR has been successfully demonstrated for a wide variety of

fast processes, such as solidification studies [242, 243, 244, 245], battery lithiation during cycling [246], and spray dynamics [247, 248]. but not yet applied to *in situ* reactive MMNC processing. Here, we present some preliminary work on real-time visualization of flux-assisted reaction synthesis performed at the Advanced Photon Source at Argonne National Laboratory (Lemont, IL).

Samples for XRR were prepared using Al (~30 μm, 99.5% purity), K_2TiF_6 flux (> 100 μm), and spherical graphite C (~10 μm, 99.95% purity) powders in composition ratios corresponding to 2 mol Al, 1 mol K_2TiF_6 flux, and 1 mol C. Powder mixtures were blended together *via* manual mixing in an agate mortar and pestle and then cold pressed at 200 MPa into thin chips 200-250 μm thick. To assemble samples for XRR, pellet pieces were sandwiched between two square quartz (SiO_2) coverslips each 100 μm thick, with an additional rectangular 250 μm thick quartz coverslip was placed at the bottom of the assembly to prevent the sample from falling through the bottom during melting. The edges of the sandwich assembly were coated in high temperature-resistant Al_2O_3-based thermal paste to ensure a robust assembly during reaction. Dimensions of the sample sandwich assemblies varied but were required to be less than 8 mm in width to fit inside the furnace assembly available at the beamline.

Preliminary synchrotron X-ray radiography (XRR) experiments were conducted at Sector 2-BM at the Advanced Photon Source (APS) at Argonne National Laboratory (Lemont, IL) to visualize the flux-assisted reaction process in real-time. Sandwich assemblies were held in place by a tungsten wire clip and Al_2O_3 rod assembly to ensure the samples would be at the correct height in the beam. A monochromatic X-ray beam operating at 20 keV was focused onto the samples and X-rays were converted to visible light using a 25 μm thick LuAg scintillator. Images were collected using a FLIR Oryx CCD with a 5× magnifying objective lens, yielding pixel sizes of 0.69 μm × 0.69 μm with the field-of-view set as 2448 × 2048 pixels (or approximately 1689 × 1413 μm^2). To conduct an XRR experiment, samples were introduced into the furnace at temperature to better simulate the process of flux-assisted reaction synthesis in a melt. The furnace temperature was increased to 950 °C and held for 10 minutes to equilibrate. Subsequently, imaging of the sample was started and then rapidly introduced into the furnace. For each experiment, images were recorded for 30 min after samples were introduced into the furnace in order to ensure capture of the complete reaction process. An exposure time of 200 ms was used for all experiments.

A sequence of radiographs, after performing flat-field correction, taken during *in situ* flux-assisted reaction are shown in Figure 5.2. In the first panel (top left) at $t = 0$ s, the sample has not yet reacted immediately after entering the furnace and dark K_2TiF_6 flux particles, owing to the contrast between more heavily attenuating Ti and lighter Al and C, are observed. Within the first few seconds, the Al begins to melt and presumably react with K_2TiF_6, releasing bubbles and causing some apparent shrinkage of flux particles (top right panel). In the subsequent panels, presumably dark regions correspond to Ti rich regions after dissolution of the K_2TiF_6, which gradually become coarser over time (bottom right panel, after 15 min reaction time). The coarsening of the Ti-rich regions may be indicative of formation and growth of TiC particles.

To better identify features observed in the radiography experiments, post-reacted samples were also characterized *ex situ* for comparison. SEM and EDS were performed on the sample shown in Figure 5.3 using a Tescan MIRA3 FEG SEM, with integrated EDAX system, operating at 15 kV and a beam intensity of 15 (see Section 3.4.2 for more details). No metallographic sample preparation was used prior to SEM imaging so as not to disrupt the microstructure from the radiography experiments. An SEM micrograph showing the region recorded during the radiography experiment (Figure 5.2) is shown in Figure 5.3(a) (denoted by the dotted red box), where surface oxides (dark grey regions) and TiC or $TiSi_xC_y$ particles (bright regions on the sample surface) are observed. A representative higher magnification micrograph of the particles is shown in Figure 5.3(b), with corresponding EDS spectra shown in Figure 5.3(c) (taken from the particle denoted with the red cross). Interestingly, particles appeared to exhibit hexagonal 6-fold symmetry, possibly corresponding to the (111) basal plane of TiC, and were 4-5 μm in diameter as measured from facet-to-facet. EDS spectra from a particle cluster suggest approximately stoichiometric amounts of Ti and C, as well as a small amount of Si. It is possible that Si appears in the samples due to reaction between the K_2TiF_6 flux and quartz slides used in sample construction. Similar TiC hexagonal platelet structures have been reported in the presence of Si [249, 250] or B [251] trace impurities, where the hexagonal morphology is attributed to slowed growth of the {111} facets. However, it is also possible that the hexagonal particle shape is induced by C/Ti off-stoichiometric ratios [214, 215], where TiC transitions from octahedral, to hexagonal, to spherical as the C/Ti ratio increases.

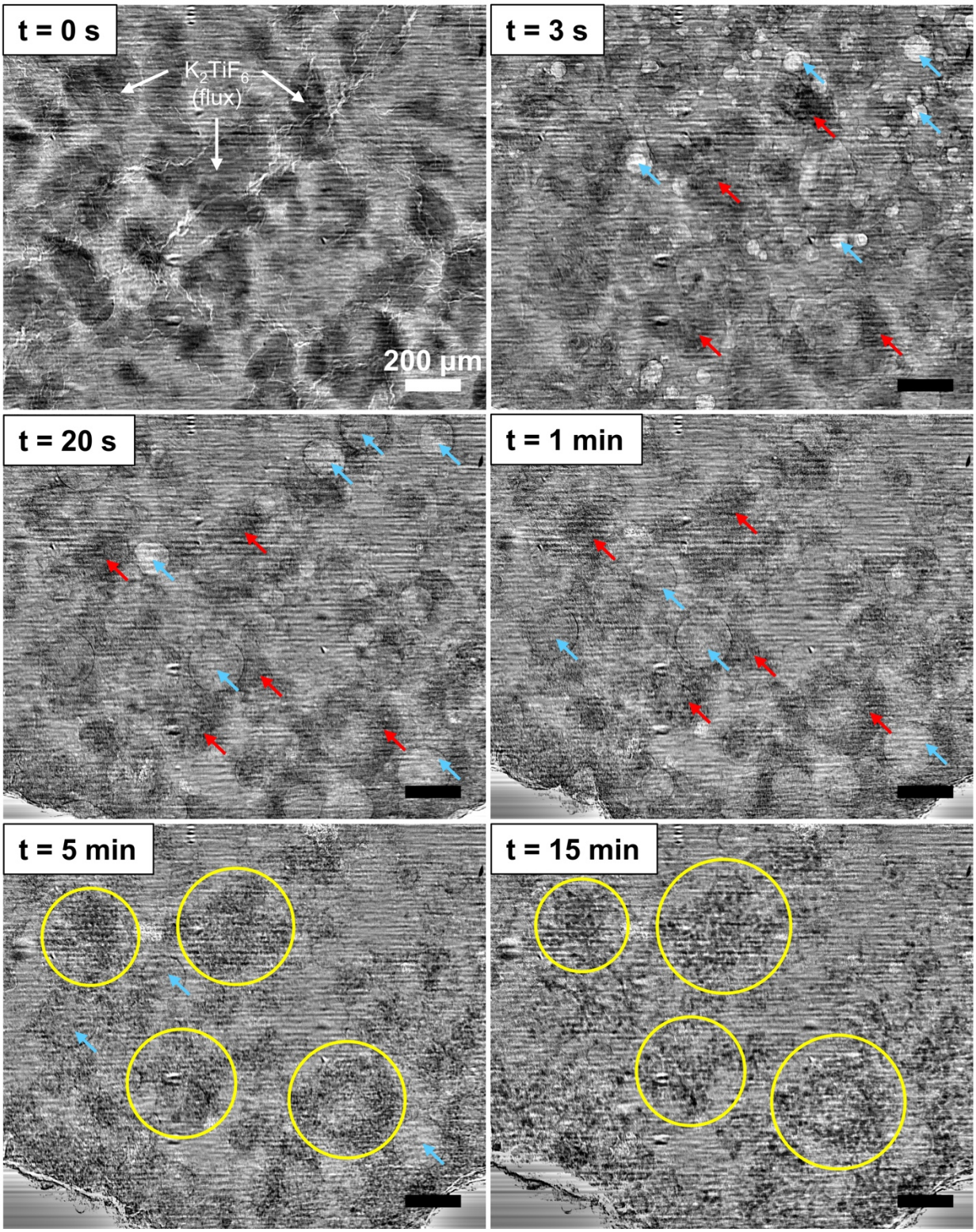

Figure 5.2. Flat-field corrected radiographs depicting various time steps during flux-assisted reaction synthesis at 950 °C. Dark particles in the initial frame correspond to K_2TiF_6. Blue arrows in subsequent frames indicate bubbles after initial sample reaction, red arrows indicate Ti-rich regions, and yellow circles indicate clusters of particles (presumably TiC).

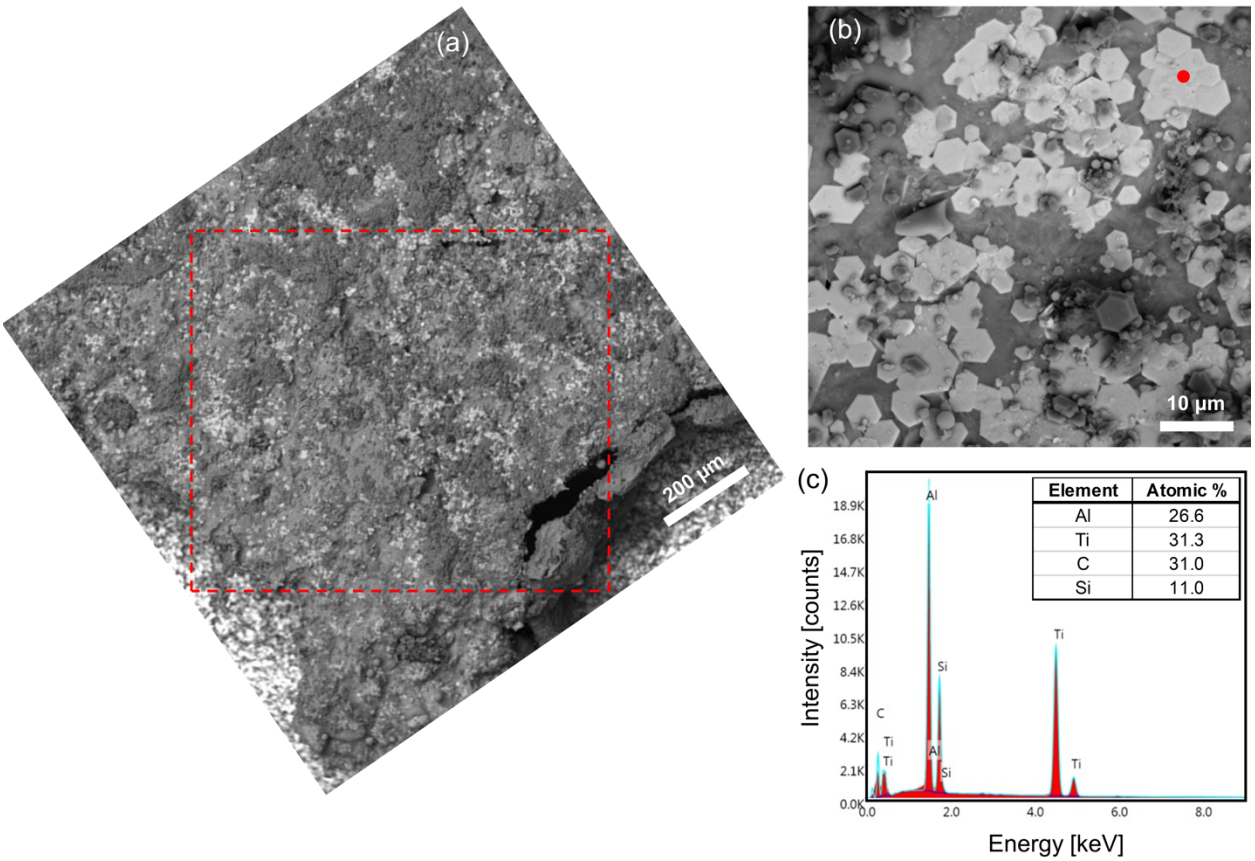

Figure 5.3. *Ex situ* characterization of the radiography sample shown in Figure 5.2. (a) SEM micrograph of sample after reaction. Radiography scans imaged in area indicated by red box. (b) Higher magnification SEM micrograph of hexagonal TiC particles. (c) EDS spectra of hexagonal TiC particles taken from red spot in (b).

Further work is required to better interpret the results of these preliminary radiography experiments specifically, such as confirming the Si-content of the hexagonal platelets and whether they are TiC particles. However, these experiments are a promising demonstration of the use of synchrotron X-ray radiography for real-time visualization of *in situ* MMNC processing methods, which may be extended to other approaches such as SHS.

5.2.7 Particle/melt interactions during solidification

While much of the work in this dissertation has focused on the relationship between processing parameters and final particle and microstructural characteristics of *in situ* MMNCs, a key step inherent to all processing methods that was not discussed is solidification. For MMNCs in particular, the specifics of how the nanoparticles affect the solidification behavior of the matrix

and their interactions with the solidification front is an important area of investigation relevant to both *in situ* and *ex situ* methods. As discussed briefly in Chapter 2, achieving a homogeneous dispersion of particles is critical to exploiting the improved mechanical properties of these composite materials and issues such as particle segregation and agglomeration during solidification have remained unsolved issues [16, 252]. Several models have been proposed over the years to try and predict melt front/particle interactions, but a large gap between the models and experimental observations remains, largely due to the complexity of the process.

In general, when the solid-liquid interface approaches a pre-existing second-phase particle during solidification it can be captured/engulfed or rejected/pushed, wherein the latter leads to segregation and dispersion inhomogeneities as the particles are moved along by the solidification front. To elucidate this behavior, several attempts have been made to model the particle/solid-liquid front interaction and extract the relevant parameters [253, 254]. However, these models have traditionally relied on several simplifying assumptions, such as spherical particles and a macroscopically planar interface, which do not always reflect the corresponding experimental observations [255]. More recent work has incorporated additional layers of complexity to explain particle capture behavior, such as melt front velocity and shape evolution [256], particle shape effects [257], particle/melt front solutal diffusion [258], particle/melt interfacial surface energies [259, 238], thermal conductivity differences [260], melt viscosity [261], and van der Waals and Brownian potential considerations [125, 238].

In addition to considerations of particle engulfment by the advancing melt front, nanoparticles may also modify the matrix solidification behavior. For example, as discussed in Chapter 2, nanoparticles have previously been demonstrated to be effective grain refiners by acting as grain nucleation sites through the induction of localized nucleation undercooling [71, 72, 73, 74]. Similarly, grain refinement can be achieved through grain growth pinning or restriction, rather than nucleation promotion. Nanoparticles have been theorized to restrict matrix grain growth *via* several potential mechanisms, such as inducing localized temperature and solute concentration differences at the particle matrix interface [262, 263, 264], acting as solutal diffusion barriers at the melt front [265], and growth front pinning *via* the Gibbs-Thomson effect [262]. Both grain growth nucleation promotion and grain growth restriction may both lead to smaller grains, and sometimes have been observed to occur simultaneously [266], which is beneficial to the overall MMNC mechanical properties.

Although a study on the solidification behavior of MMNCs was outside the scope of this dissertation, it is apparent that the interactions between the particles and the melt during solidification are highly complex processes with many interlinking factors. Thus, a future research direction focusing on this topic is promising and critical to move towards a complete understanding of controlling MMNC characteristics such as particle dispersion and matrix grain size. Presumably a combination of the techniques demonstrated in this thesis, such as 3D microstructural visualization *via* TXM, real-time solidification *via* X-ray radiography, and processing-microstructure correlation *via* CCA, could be utilized to better understand these highly complex, interlinked processes.

REFERENCES

[1] "Lightweight Materials for Cars and Trucks." Vehicle Technologies Office, Office of Energy Efficiency & Renewable Energy. Available: https://www.energy.gov/eere/vehicles/lightweight-materials-cars-and-trucks

[2] A.I. Taub, E. De Moor, A. Luo, D.K. Matlock, J.G. Speer, U. Vaidya. Materials for automotive lightweighting. *Annu. Rev. Mater. Res.* **49**, 327-59 (2019).

[3] D. Weiss. Improved high-temperature aluminum alloys containing cerium. *J. Mater. Eng. Perform.* **28**, 1903-1908 (2019).

[4] Ø. Ryen, O. Nijs, E. Sjölander, B. Holmedal , H.-E. Ekström, E. Nes. Strengthening mechanisms in solid solution aluminum alloys. *Metall. Mater. Trans. A* **37A**, 1999-2006 (2006).

[5] C.B. Fuller, D.N. Seidman, D.C. Dunand. Mechanical properties of Al(Sc,Zr) alloys at ambient and elevated temperatures. *Acta. Mater.* **51(16)**, 4803-4814 (2003).

[6] J.K. Kim, H.K. Kim, J.W. Park, W.J. Kim. Large enhancement in mechanical properties of the 6061 Al alloys after a single pressing by ECAP. *Scr. Mater.* **53(10)**, 1207-1211 (2005).

[7] I. Anza. *Synthesis of Aluminum-Titanium Carbide Nanocomposites by the Rotating Impeller Gas-Liquid In-Situ Method.* PhD Thesis. Worcester Polytechnic Institute (2016).

[8] Z. Guo, W. Sha. Quantification of precipitation hardening and evolution of precipitates. *Mater. Trans.* **43(6)**, 1273-1282 (2002).

[9] L. Ceschini, A. Dahle, M. Gupta, A.E. Wollmar, J.S. Jayalakshmi, A. Morri, F. Rotundo, S. Toschi, R.A Singh. *Aluminum and Magnesium Metal Matrix Nanocomposites*. 1st Ed. Springer (2017).

[10] T.W. Clyne. *An Introduction to Metal Matrix Composites*. 1st Ed. Cambridge University Press (1993).

[11] I.A. Ibrahim, F.A. Mohamed, E.J. Lavernia. Particulate reinforced metal matrix composites – A review. *J. Mater. Sci.* **26**, 1137 (1991).

[12] R. Casati, M. Vdani. Metal matrix composites reinforced by nano-particles – A review. *Metals* **4**, 65 (2014).

[13] C. Borgonovo. *Synthesis of Aluminum-Aluminum Nitride Nanocomposites by Gas-Liquid Reactions*. PhD thesis. Worcester Polytechnic Institute (2013).

[14] F. Delannay, L. Froyen, A. Deruyttere. The wetting of solids by molten metals and its relation to the preparation of metal-matrix composites. *J. Mater. Sci.* **22**, 1-16 (1987).

[15] D. Zhao, F. Qiu, H. Wang, Q. Jiang. Manufacture of nano-sized particle-reinforced metal matrix composites: A review. *Acta. Metall. Sin. (Engl. Lett.)* **27**, 798 (2014).

[16] Y. Yang, J. Lan, X. Li. Study on bulk aluminum matrix nano-composite fabricated by ultrasonic dispersion of nano-sized SiC particles in molten aluminum alloy. *Mater. Sci. Eng. A* **380**, 378 (2004).

[17] A. Manoylov, V. Bojarevics, K. Pericelous. Modeling the break-up of nano-particle clusters in aluminum- and magnesium-based metal matrix nano-composites. *Metall. Mater. Trans. A* **46A**, 2893-2907 (2015).

[18] X.-H. Chen, H. Yan. Solid-liquid interface dynamics during solidification of Al 7075-Al2O3np based metal matrix composites. *Mater. Des.* **94**, 148-158 (2016).

[19] A.D. Hamedan, M. Shahmiri. A new model for the solidification of metal matrix nanocomposites: Wet cluster engulfment of nanoparticles by the solidification front. *J. Compos. Mater.* **51(20)**, 2913-2932 (2017).

[20] M. Karbalaei Akbari, H.R. Baharvandi, K. Shirvanimoghaddam. Tensile and fracture behavior of nano/micro TiB2 particle reinforced casting A356 aluminum alloy composites. *Mater. Des.* **66(A)**, 150 (1980-2015).

[21] J. Hashim, L. Looney, M.S.J. Hashmi. The wettability of SiC particles by molten aluminum alloy. *J. Mater. Process. Technol.* **68**, 324 (2001).

[22] S.Y. Oh, J.A. Cornie, K.C. Russell. Wetting of ceramic particulates with liquid aluminum alloys: Part II. Study of wettability. *Metall. Trans. A* **20(3)**, 533 (1989).

[23] B.S.S. Daniel, V.S.R. Murthy, G.S. Murty. Metal-ceramic composites via in-situ methods. *J. Mater. Process. Technol.* **68**, 132 (1997).

[24] S.C. Tjong, Z.Y. Ma. Microstructural and mechanical characteristics of in situ metal matrix composites. *Mater. Sci. Eng.* **29**, 49 (2000).

[25] N. Chawla and Y.-L. Shen. Mechanical behavior of particle reinforced metal matrix composites. *Adv. Eng. Mater.* **3**, 357-370 (2001).

[26] R.F. Shyu, F.T. Weng, C.T. Ho. In situ reacted titanium nitride-reinforced aluminum alloy composite. *J. Mater. Process. Technol.* **122**, 301 (2002).

[27] R.F. Shyu, C.T. Ho. In situ reacted titanium carbide-reinforced aluminum alloy composite. *J. Mater. Process. Technol.* **171**, 411 (2006).

[28] C. Wang, H. Gao, Y. Dai, X. Ruan, J. Shen, J. Wang, B. Sun. In-situ technique for synthesizing Fe-TiN composites. *J. Alloys Compd.* **490**, 9 (2010).

[29] C. Borgonovo, M.M. Makhlouf. Synthesis of aluminum-aluminum nitride nanocomposites by gas-liquid reactions I. Thermodynamic and kinetic considerations. *Metall. Mater. Trans. A* **47A**, 5125-5135 (2016).

[30] I. Anza, M.M. Makhlouf. Synthesis of aluminum-titanium carbide micro and nanocomposites by the rotating impeller in-situ gas-liquid reaction method. *Metall. Mater. Trans. B* **49B**, 466-480 (2018).

[31] J. Fedors. *Innovations on In-Situ Processes for Production of Aluminum-Matrix Nanocomposites*. MS thesis. Worcester Polytechnic Institute (2018).

[32] C. Wang, H. Gao, Y. Dai, X. Ruan, J. Shen, J. Wang, B. Sun. In-situ technique for synthesizing Fe-TiN composites. *J. Alloys and Compd.* **490**, L9-L11 (2010).

[33] H.C. Yi and J.J. Moore. Self-propagating high-temperature (combustion) synthesis (SHS) of powder-compacted materials. *J. Mater. Sci.* **25**, 1159-1168 (1990).

[34] J.J. Moore, H.J. Feng. Combustion synthesis of advanced materials: Part I. Reaction parameters. *Prog. Mater. Sci.* **39**, 243-273 (1995).

[35] J.J. Moore, H.J. Feng. Combustion synthesis of advanced materials: Part II. Classification, applications and modelling. *Prog. Mater. Sci.* **39**, 275-316 (1995).

[36] W. Garrett. *Control of Self-Propagating High-Temperature Synthesis of Derived Aluminum-Titanium Carbide Metal Matrix Composites*. PhD thesis. Colorado School of Mines (2012).

[37] J Nuechterlein. *Production of Ceramic Nanoparticles Through Self-Propagating High-Temperature Synthesis (SHS) and Their Introduction Into a Metallic Matrix to Form Metal Matrix Composites (MMC)*. PhD thesis. Colorado School of Mines (2013).

[38] Y.H. Cho, J.M. Lee, S.H. Kim. Al-TiC composites fabricated by a thermally activated reaction process in an Al melt using Al-Ti-C-CuO powder mixtures. Part I: Microstructural evolution and reaction mechanism *Metall. Mater. Trans. A* **45**, 5667-5678 (2014).

[39] H.Y. Wang, Q.C. Jiang, X.L. Li, F. Zhao. Effect of Al content on the self-propagating high-temperature synthesis reaction of Al-Ti-C system in molten magnesium. *J. Alloys and Compd.* **366(1-2)**, L9-L12 (2004).

[40] I.P. Borovinskaya, T.I. Ignat'eva, O.M. Emel'yanova, V.I. Vershinnikov, V.N. Semenova. Self-propagating high-temperature synthesis of ultrafine and nanometer-sized TiC particles. *Inorg. Mater.* **43**, 1206-1214 (2007).

[41] I. Gotman, M.J. Koczak, E. Shtessel. Fabrication of Al matrix in situ composites via self-propagating synthesis. *Mater. Sci. Eng. A* **187**, 189-199 (1994).

[42] Q.C. Jiang, X.L. Li, H.Y. Wang. Fabrication of TiC particulate reinforced magnesium matrix composites. *Scr. Mater.* **48(6)**, 713-717 (2003).

[43] N. Zarrinfar, P.H. Shipway, A.R. Kennedy, A. Saidi. Carbide stoichiometry in TiCx and Cu-TiCx produced by self-propagating high-temperature synthesis. *Scr. Mater.* **46(2)**, 121-126 (2002).

[44] B.Y. Li, L.J. Rong, Y.Y. Li, V.E. Gjunter. Synthesis of porous Ni-Ti shape-memory alloys by self-propagating high-temperature synthesis: Reaction mechanism and anisotropy in pore structure. *Acta Mater.* **48(15)**, 3895-3904 (2000).

[45] X. Su, F. Fu, Y. Yan, G. Zheng, T. Liang, Q. Zhang, X. Cheng, D. Yang, H. Chi, X. Tang, Q. Zhang, C. Uher. Self-propagating high-temperature synthesis for compound thermoelectrics and new criterion for combustion processing. *Nat. Commun.* **5**, 4908 (2014).

[46] W. Liu, C. Cao, J. Xu, X. Wang, X. Li. Molten salt assisted solidification nanoprocessing of Al-TiC nanocomposites. *Mater. Lett.* **185**, 392-395 (2016).

[47] A. Javadi, C. Cao, X. Li. Manufacturing of Al-TiB2 nanocomposites by flux-assisted liquid state processing. *Procedia Manuf.* **10**, 531-535 (2017).

[48] A.R. Kennedy, A.E. Karantzalis. The incorporation of ceramic particles in molten aluminum and the relationship to contact angle data. *Mater. Sci. Eng. A* **264(1-2)**, 122-129 (1999).

[49] C. Cao, H. Ling, N. Murali, X. Li. In-situ molten salt reaction and incorporation of small (10 nm) TiC nanoparticles into Al. *Materialia* **7**, 100425 (2019).

[50] Y. Birol. In situ synthesis of Al-TiCp composites by reacting K2TiF6 and particulate graphite in molten aluminum. *J. Alloys Compd.* **454**, 110-117 (2008).

[51] J. Fjellstedt, A.E.W. Jarfors. On the precipitation of TiB2 in aluminum melts from the reaction with KBF4 and K2TiF6. *Mater. Sci. Eng. A* **413-414**, 527-532 (2005).

[52] Y. Birol. Production of Al-B alloy by heating Al/KBF4 powder blends. *J. Alloys and Compd.* **481(1-2)**, 195-198 (2009).

[53] Y. Birol. Response to thermal exposure of Al/K2TiF6/C powder blends. *J. Alloys Compd.* **455**, 164-167 (2008).

[54] P. Baumli, J. Sytchev, G. Kaptay. Perfect wettability of carbon by liquid aluminum achieved by a multifunctional flux. *J. Mater. Sci.* **45**, 5177-5190 (2010).

[55] Z. Li, D. Chen, H. Wang, E.J. Lavernia, A. Shan. Nano-TiB2 reinforced ultrafine-grained pure Al produced by flux-assisted synthesis and asymmetrical rolling. *J. Mater. Res.* **29(21)**, 2514-2524 (2014).

[56] X. Wang, A. Jha, R. Brydson. In situ fabrication of Al3Ti particle reinforced aluminum alloy metal-matrix composites. *Mater. Sci. Eng. A* **364**, 339-345 (2004).

[57] F.A. Mirza, D.L. Chen. A unified model for the prediction of yield strength in particulate-reinforced metal matrix nanocomposites. *Materials* **8**, 5138-5153 (2015).

[58] J.B. Ferguson, B.F. Schultz, D. Venugopalan, H.F. Lopez, P.K. Rohatgi, K. Cho, C.-S. Kim. On the superposition of strengthening mechanisms in dispersion strengthened alloys and metal-matrix nanocomposites: Considerations of stress and energy. *Met. Mater. Int.* **20**, 375-388 (2014).

[59] W.S. Miller, F.J. Humphreys. Strengthening mechanisms in particulate metal matrix composites. *Scr. Mater.* **25**, 33 (1991).

[60] A. Sanaty-Zadeh. Comparison between current models for the strength of particulate-reinforced metal matrix nanocomposites with emphasis on consideration of Hall-Petch effect. *Mater. Sci. Eng. A* **531**, 112 (2012).

[61] T.W. Clyne, D. Hull. *An Introduction to Composite Materials.* 2nd Ed. Cambridge University Press (1996).

[62] N. Ramakrishnan. An analytical study on strengthening of particulate reinforced metal matrix composites. *Acta Mater.* **44**, 69 (1996).

[63] V.C. Nardone, K.M. Prewo. On the strength of discontinuous silicon carbide reinforced aluminum composites. *Scr. Metall.* **20(1)**, 43-48 (1986).

[64] B. Derby, J.R. Walker. The role of enhanced matrix dislocation density in strengthening metal matrix composites. *Scr. Mater.* **22**, 529 (1988).

[65] M.A. Meyers, K.K. Chawla. *Mechanical Behavior of Materials*. 2nd Ed. Cambridge University Press (2007).

[66] Z. Zhang, D.L. Chen. Consideration of Orowan strengthening effect in particulate-reinforced metal matrix nanocomposites: A model for predicting their yield strength. *Scr. Mater.* **54**, 1321 (2006).

[67] Z. Zhang, D.L. Chen. Contribution of Orowan strengthening effect in particulate-reinforced metal matrix nanocomposites. *Mater. Sci. Eng. A* **483-484**, 148-152 (2008).

[68] G. Chen, J. Wan, N. He, H.-M. Zhang, F. Han, Y.-M. Zhang. Strengthening mechanisms based on reinforcement distribution uniformity for particle reinforced aluminum matrix composites. *Trans. Nonferrous Met. Soc. China* **28**, 2395-2400 (2018).

[69] J.B. Ferguson, H. Lopez, D. Kongshaug, B. Schultz, P. Rohatgi. Revised Orowan strengthening: Effective interparticle spacing and strain field considerations. *Metall. Mater. Trans. A* **43A**, 2110-2115 (2012).

[70] C. Cao, G. Yao, L. Jiang, M. Sokoluk, X. Wang, J. Ciston, A. Javadi, Z. Guan, I. De Rosa, W. Xie, E.J. Lavernia, J.M. Schoenung, X. Li. Bulk/ultrafine grained/nanocrystalline metals via slow cooling. *Sci. Adv.* **5**, 1-10 (2019).

[71] Z. Liu. Review of grain refinement of cast metals through inoculation: Theories and developments. *Metall. Mater. Trans. A* **48A**, 4755-4776 (2017).

[72] W. Li, J. Mao, J. Feng. Aluminum grain refinement by Ti(C, N) nanoparticles additions: Principles, advantages and drawbacks. *Metall. Res. Technol.* **116(2)**, 212 (2019).

[73] A.L. Greer, A.M. Bunn, A. Tronche, P.V. Evans, D.J. Bristow. Modeling of inoculation of metallic melts: Application to grain refinement of aluminum by Al-Ti-B. *Acta Mater.* **48**, 2823-2835 (2000).

[74] T.E. Quested, A.L. Greer. The effect of the size distribution of inoculant particles on as-cast grain size in aluminum alloys. *Acta Mater.* **52**, 3859-3868 (2004).

[75] G. Couturier, C. Maurice, R. Fortunier. Three-dimensional finite-element simulation of Zener pinning dynamics. *Philos. Mag.* **83(30)**, 3387-3405 (2003).

[76] V.Y. Novikov. On Zener pinning in 3D polycrystals. *Scr. Mater.* **42(5)**, 439-443 (2000).

[77] C. Borgonovo, M.M. Makhlouf. Synthesis of aluminum-aluminum nitride nanocomposites by a gas-liquid reaction II. Microstructure and mechanical properties. *Metall. Mater. Trans. A* **47A**, 118 (2016).

[78] S. Fale, A. Likhite, J. Bhatt. Compressive, tensile and wear behavior of ex situ Al/AlN metal matrix nanocomposites. *J. Comp. Mater*. **49(16)**, 1917 (2015).

[79] X. Ma, Y.F. Zhao, W.J. Tian, Z. Qian, H.W. Chen, Y.Y. Wu, X.F. Liu. A novel Al matrix composite reinforced by nano-AlNp network. *Sci. Rep.* **6**, 34919 (2016).

[80] Y.-H. Cho, J.-M. Lee, S.-H. Kim. Al-TiC composites fabricated by a thermally activated reaction process in an Al melt using Al-Ti-C-CuO powder mixtures: Part II. Microstructure control and mechanical properties. *Metall. Mater. Trans A* **46A**, 1374-1384 (2015).

[81] X.C. Tong, H.S. Fang. Al-TiC composites in situ-processed by ingot metallurgy and rapid solidification technology: Part II. Mechanical behavior. *Metall. Mater. Trans. A* **29A**, 893-902 (1998).

[82] Z. Hu, M. Pozuelo, M. Sokoluk, S. Mathaudhu, C. Roach, X. Li, J.-M. Yang. Micro-mechanical properties of homogeneous- and inhomogeneous structured pillars in Al-TiC nanocomposite: An in-situ study. *Mater. Sci. Eng. A* **762**, 138084 (2019).

[83] T. Xu, G. Li, M. Xie, M. Liu, D. Zhang, Y. Zhao, G. Chen, X. Kai. Microstructure and mechanical properties of in-situ nano γ-Al2O3/A356 aluminum matrix composite. *J. Alloys and Compd.* **787**, 72-85 (2019).

[84] Y.-C. Kang, S.L. Chan. Tensile Properties of Nanometric Al2O3 particulate-reinforced aluminum matrix composites. *Mater. Chem. Phys.* **85**, 438 (2004).

[85] Z.Y. Ma, Y.L. Li, Y. Liang, F. Zheng, J. Bi, S.C. Tjong. Nanometric Si3N4 particulate-reinforced aluminum composite. *Mater. Sci. Eng. A* **219**, 229 (1996).

[86] Z. Chen, H. Kang, Y. Zhao, Y. Zheng, T. Wang. The role of TiB2 in strengthening TiB2 reinforced aluminum casting composites. *Mater. Sci. Eng.* **117**, 012039 (2016).

[87] M. Li, H. Zhai, Z. Huang, X. Liu, Y. Zhou, S. Li, C. Li. Tensile behavior and strengthening mechanism in ultrafine TiC0.5 particle reinforced Cu-Al matrix composites. *J. Alloys. And Compd.* **628**, 186 (2015).

[88] S. Fale, A. Likhite, J. Bhatt. Nanoindentation studies of ex situ AlN/Al metal matrix nanocomposites. *J. Alloys. Compd.* **615**, S395 (2014).

[89] N. Chawla, C. Andres, J.W. Jones, J.E. Allison. Effect of SiC volume fraction and particle size on the fatigue resistance of a 2080 Al/SiCp composite. *Metall. Mater. Trans. A* **29A,** 2843 (1998).

[90] O. Kolednik, K. Unterweger. The ductility of metal matrix composites – Relation to local deformation behavior and damage evolution. *Eng. Frac. Mech*. **75**, 3663 (2008).

[91] S. Ghosh, S. Moorthy. Particle fracture simulation in non-uniform microstructures of metal-matrix composites. *Acta Mater.* **46(3)**, 965-982 (1998).

[92] L. Babout, Y. Brechet, E. Maire, R. Fougères. On the competition between particle fracture and particle decohesion in metal matrix composites. *Acta Mater.* **52(15)**, 4517-4525 (2004).

[93] J. Yang, C. Cady, M.S. Hu, F. Zok, R. Mehrabian, A.G. Evans. Effects of damage on the flow strength and ductility of a ductile Al alloy reinforced with SiC particulates. *Acta. Metall. Mater.* **38(12)**, 2613-2619 (1990).

[94] M.T. Kiser, F.W. Zok, D.S. Wilkinson. Plastic flow and fracture of a particulate metal matrix composite. *Acta Mater.* **44(9)**, 3465-3476 (1996).

[95] M.T. Milan, P. Bowen. Tensile and fracture toughness properties of SiCp reinforced Al alloys: Effects of particle size, particle volume fraction, and matrix strength, *J. Mater. Eng. Perform.* **13**, 775-783 (2004).

[96] W.-S. Tian, D.-S. Zhou, F. Qiu, Q.C. Jiang. Superior tensile properties of in situ nano-sized TiCp/Al-Cu composites fabricated by reaction in melt method. *Mater. Sci. Eng. A*, **658** 409-414 (2016).

[97] A.I. Khdair, A. Fathy. Enhanced strength and ductility of Al-SiC nanocomposites synthesized by accumulative roll bonding. *J. Mater. Res. Tech.* **9(1)**, 478-489 (2020).

[98] Sajjadi, S.A., Ezatpour, H.R., & Torabi Parizi, M. Comparison of Microstructure and Mechanical Properties of A356 Aluminum Alloy/Al2O3 Composites Fabricated by Stir and Compo-Casting Processes. *Mater. Des.* **34**, 106 (2012).

[99] Mazahery, A. & Shabani, M.O. Plasticity and Microstructure of A356 Matrix Nanocomposites. *JKSUS* **25**, 41 (2013).

[100] R.G. Guan, D. Tie. A review on grain refinement of aluminum alloys: Progresses, challenges and prospects. *Acta Metall. Sin. (Eng. Lett.)* **30(5)**, 409-432 (2017).

[101] H.M. Fu, M.-X. Zhang, D. Qiu, P.M. Kelly, J.A. Taylor. Grain refinement by AlN particles in Mg-Al based alloys. *J. Alloys Compd.* **478**, 809-812 (2009).

[102] S.-B. Kim, Y.-H. Cho, M.-S. Jo, J.-G. Jung, Y.-K. Lee, J.-M. Lee. Quantitative approach to realization of ultrasonic grain refinement of Al-7Si-2Cu-1Mg alloy. *Sci. Rep.* **9**, 17812 (2019).

[103] Nan, C.-W. & Clarke, D.R. The Influence of Particle Size and Particle Fracture on the Elastic/Plastic Deformation of Metal Matrix Composites. *Acta. Mater.* **44**, 3801 (1996).

[104] T. Ye, Y. Xu, J. Ren. Effects of SiC particle size on mechanical properties of SiC particle reinforced aluminum metal matrix composite. *Mater. Sci. Eng. A* **753**, 146-155 (2019).

[105] Z. Zhang, D.L. Chen. Contribution of Orowan strengthening effect in particulate-reinforced metal matrix nanocomposites. *Mater. Sci. Eng. A* **483-484**, 148-152 (2008).

[106] T.J.A. Doel, P. Bowen. Tensile properties of particulate-reinforced metal matrix composites. *Comp. Part A* **27A**, 655-665 (1996).

[107] A.L. Greer, A.M. Bunn, A. Tronche, P.V. Evans, D.J. Bristow. Modeling of inoculation of metallic melts: Application to grain refinement of aluminum by Al-Ti-B. *Acta Mater.* **48**, 2823-2835 (2000).

[108] T.E. Quested, A.L. Greer. The effect of the size distribution of inoculant particles on as-cast grain size in aluminum alloys. *Acta Mater.* **52**, 3859-3868 (2004).

[109] D. Wang, M.P. De Cicco, X. Li. Using diluted master nanocomposites to achieve grain refinement and mechanical property enhancement in as-cast Al-9Mg. *Mater. Sci. Eng. A* **532**, 396-400 (2012).

[110] K.J.M. Bishop, C.E. Wilmer, S. Soh, B.A. Grzybowski. Nanoscale forces and their uses in self-assembly. *Small* **5(14)**, 1600-1630 (2009).

[111] Y. Min, M. Akbulut, K. Kristiansen, Y. Golan, J. Israelachvili. The role of interparticle and external forces in nanoparticle assembly. *Nature Mater*. **7**, 527–538 (2008).

[112] H. Somekawa, A. Singh, Y. Mukai. High fracture toughness of extruded Mg-Zn-Y alloy by the synergistic effect of grain refinement and dispersion of the quasicrystalline phase. *Scr. Mater.* **56**, 1091-1094 (2007).

[113] T. Nishizawa, I. Ohnuma, K. Ishida. Examination of the Zener relationship between grain size and particle dispersion. *Mater. Trans. JIM* **38(11)**, 950-956 (1997).

[114] D.J. Srolovitz, M.P. Anderson, G.S. Grest, P.S. Sahni. Computer simulation of grain growth-III. Influence of a particle dispersion. *Acta Metall.* **32(9)**, 1429-1438 (1984).

[115] S. García-Rodríguez, N. Alba-Baena, N.M. Rudolph, J. Wellekoetter, X.C. Li, T.A. Osswald. Dimensional analysis and scaling in mechanical mixing for fabrication of metal matrix nanocomposites. *J. Manuf. Proc.* **14(3)**, 388-392 (2012).

[116] A.H. Jabbari, M. Sedighi. Investigation of electromagnetic and mechanical stirring sequence effects on production of magnesium matrix nanocomposite. *Int. J. Metalcast.* **14**, 489-504 (2020).

[117] D. Zhang, L. Nastac. Numerical modeling of the dispersion of ceramic nanoparticles during ultrasonic processing of aluminum-based nanocomposites. *J. Mater. Res. Tech.* **3**, 296 (2014).

[118] P. Mohanty, R. Mahapatra, P. Padhi, CH.V.V. Ramana, D.K. Mishra. Ultrasonic cavitation: An approach to synthesize uniformly dispersed metal matrix nanocomposites – A review. *Nano-Structures & Nano-Objects* **23**, 100475 (2020).

[119] S.G. Thoma, M. Ciftcioglu, D.M. Smith. Determination of agglomerate strength distributions: Part 1. Calibration via ultrasonic forces. *Powder Technol.* **68(1)**, 53-61 (1991).

[120] K.A. Kusters, S.E. Pratsinis, S.G. Thomas, D.M. Smith. Ultrasonic fragmentation of agglomerate powders. *Chem. Eng. Sci.* **48(24)**, 4119-4127 (1993).

[121] K.A. Kusters, S.E. Pratsinis, S.G. Thoma, D.M. Smith. Energy-size reduction laws for ultrasonic fragmentation. *Powder Technol.* **80(3)**, 253-263 (1994).

[122] Z. Wang, M. Song, C. Sun, Y. He. Effects of particle size and distribution on the mechanical properties of SiC reinforced Al-Cu alloy composites. *Mater. Sci. Eng. A* **528**, 1131 (2011).

[123] J. Nafar Dastgerdi, B. Anbarlooie, A. Miettinen, H. Hosseini-Toudeshky, H. Remes. Effects of particle clustering on the plastic deformation and damage initiation of particulate reinforced composite utilizing X-ray CT data and finite element modeling. *Compos. B Eng.* **153**, 57-69 (2018).

[124] H. Ghodrati, R. Ghomashchi. Effect of graphene dispersion and interfacial bonding on the mechanical properties of metal matrix composites: An overview. *FlatChem* **16**, 100113 (2019).

[125] L. Chen, J. Xu, H. Choi, M. Pozuelo, X. Ma, S. Bhowmick, J. Yang, S. Mathaudhu, X. Li. Processing and properties of magnesium containing a dense uniform dispersion of nanoparticles. *Nature* **528**, 539-543 (2015).

[126] S.C. Tjong. Novel nanoparticle-reinforced metal matrix composites with enhanced mechanical properties. *Adv. Eng. Mater.* **9**, 639 (2007).

[127] V. Viswanathan, T. Laha, K. Balani, A. Agarwal, S. Seal. Challenges and advances in nanocomposite processing techniques. *Mater. Sci. Eng.* **54(5-6)**, 121-285 (2006).

[128] S. Tahamtan, M. Emamy, A. Halvee. Effects of reinforcing particle size and interface bonding strength on tensile properties and fracture behavior of Al-A206/aluminum micro/nanocomposites. *J. Compos. Mater*. **48(27)**, 3331 (2014).

[129] T.P.D. Rajan, R.M. Pillai, B.C. Pai. Reinforcement coatings and interfaces in aluminum metal matrix composites. *J. Mater. Sci.* **33**, 3491-3503 (1998).

[130] F.A. Feest. Interfacial phenomena in metal-matrix composites. *Composites* **25(2)**, 75-86 (1994).

[131] B. Chen, J. Shen, X. Ye, H. Imai, J. Umeda, M. Takahashi, K. Kondoh. Solid-state interfacial reaction and load transfer efficiency in carbon nanotubes (CNTs)-reinforced aluminum matrix composites. *Carbon* **114**, 198-208 (2017).

[132] W. Zhou, S. Bang, H. Kurita, T. Miyazaki, Y. Fan, A. Kawasaki. Influence and interfacial reactions in multi-walled carbon nanotube-reinforced aluminum matrix composites. *Carbon* **96**, 919-928 (2016).

[133] B.Y. Zong, F. Zhang, G. Wang, L. Zuo. Strengthening mechanism of load sharing of particulate reinforcements in a metal matrix composite. *J. Mater. Sci.* **42**, 4215-4226 (2007).

[134] Q. Guo, Y. Han, D. Zhang. Interface-dominated mechanical behavior in advanced metal matrix composites. *Nano Mater. Sci.* **2**, 66-71 (2020).

[135] V.A. Romanova, R.R. Balokhonov, S. Schmauder. The influence of the reinforcing particle shape and interface strength on the fracture behavior of a metal matrix composite. *Acta Mater.* **57**, 97-107 (2009).

[136] L.M. Tham, M. Gupta, L. Cheng. Effect of limited matrix-reinforcement interfacial reaction on enhancing the mechanical properties of aluminum-silicon carbide composites. *Acta Mater.* **49**, 3243-3253 (2001).

[137] J.C. Lee, J.P. Ahn, Z. Shi, Y. Kim, H.I. Lee. Modification of the interface in SiC/Al Composites. *Metall. Mater. Trans. A* **31A**, 2361-2368 (2000).

[138] L. Wang, F. Qiu, Q. Zhao, M. Zha, Q. Jiang. Superior high creep resistance of in situ nano-sized TiCx/Al-Cu-Mg composite. *Sci. Rep.* **7**, 4540 (2017).

[139] G.C. Weatherly. Coherent and incoherent particles, and loss of coherency. *Can. Metall. Q.* **10(1)**, 9-11 (1971).

[140] S. Iwamura, Y. Miura. Loss in coherency and coarsening behavior of Al3Sc precipitates. *Acta Mater.* **52**, 591-600 (2004).

[141] Y. Ji, Y. Lou, M. Qu, J.D. Rowatt, F. Zhang, T.W. Simpson, L.-Q. Chen. Predicting coherency loss of γ'' precipitates in IN718 superalloy. *Metall. Mater. Trans. A* **47A**, 3235-3247 (2016).

[142] J.B. Mitchell. Mechanisms of growth and loss coherency of HfN particles in molybdenum. *Acta Metall.* **19**, 1063-1077 (1971).

[143] C.W. Reese, A. Gladstein, J.M. Fedors, V. De Andrade, B. Mishra, A.J. Shahani, A.I.Taub. *In situ* Al-TiC composites fabricated by self-propagating high-temperature reaction: Insights on reaction pathways and their microstructural signatures. *Metall. Mater. Trans. A* **51,** 3587–3600 (2020).

[144] A. Paknia, A. Pramanik, A.R. Dixit, S. Chattopadhyaya. Effect of size, content and shape of reinforcements on the behavior of metal matrix composites (MMCs) under tension. *J. Mater. Eng. Perform.* **25**, 4444-4459 (2016).

[145] L. Banks-Sills, V. Leiderman, D. Fang. On the effect of particle shape and orientation on elastic properties of metal matrix composites. *Compos. Part B-Eng.* **28**, 465-481 (1997).

[146] T. Fan, C. Zhang, J. Chen, D. Zhang. Thermodynamics and kinetics to alloying addition on in-situ AlN/Mg composites synthesis via displacement reactions in liquid Mg melt. *Metall. Mater. Trans. A* **40A**, 2743-2750 (2009).

[147] Q. Zheng, R.G. Reddy. Mechanism of in situ formation of AlN in Al melt using nitrogen gas. *J. Mater. Sci.* **39(1)**, 141-149 (2004).

[148] Q. Zheng, R.G. Reddy. Kinetics of in-situ formation of AlN in Al alloy melts by bubbling ammonia gas. *Metall. Mater. Trans. B* **34(6)**, 793-804 (2003).

[149] C. Borgonovo, D. Apelian. Aluminum nanocomposites via gas assisted processing. *Mater. Sci. Forum* **690**, 187-191 (2011).

[150] J. Goldstein, D.E. Newbury, D.C. Joy, C.E. Lyman, P. Echlin, E. Lifshin, L. Sawyer, J.R. Michael. *Scanning Electron Microscopy and X-Ray Microanalysis*. 3rd Ed. Springer (2012).

[151] B.D. Cullity. *Elements of X-Ray Diffraction*. 2nd Ed. Pearson (1978).

[152] X.C. Tong, H.S. Fang. Al-TiC composites in situ-processed by ingot metallurgy and rapid solidification technology: Part I. Microstructural evolution. *Metall. Mater. Trans. A* **29A**, 875-891 (1998).

[153] M.S. Song, M.X. Zhang, S.G. Zhang, B. Huang, J.G. Li. In situ fabrication of TiC particulates locally reinforced aluminum matrix composites by self-propagating reaction during casting. *Mater. Sci. Eng. A* **473**, 166-171 (2008).

[154] Y.-H. Cho, J.-M. Lee, H.-J. Kim, J.-J. Kim, S.-H. Kim. Feasible process for producing in situ Al/TiC composites by combustion reaction in an Al melt. *Met. Mater. Int.* **19(5)**, 1109-1116 (2013).

[155] A. Tronche, M. Vandyoussefi, A.L. Greer. Instability of TiC particles in aluminum melts inoculated with an Al-Ti-C grain refiner. *Mater. Sci. Technol.* **18**, 1072-1078 (2002).

[156] N. Frage, N. Frumin, L. Levin, M. Polak, M.P. Dariel. High-temperature phase equilibria in the Al-rich corner of the Al-Ti-C system. *Metall. Mater. Trans. A* **29A**, 1341-1345 (1998).

[157] M. Vandyoussefi, J. Worth, A.L. Greer. Effect of instability of TiC particles ongrain refinement of Al and Al-Mg alloys by addition of Al-Ti-C inoculants. *Mater. Sci. Technol.* **16**, 1121-1128 (2000).

[158] H.-M. Ding, X.-F. Liu. Influence of Si on stability of TiC in Al melts. *Trans. Nonferrous Met. Soc. China* **21**, 1465-1472 (2011).

[159] P.S. Mohanty, J.E. Gruzleski. Grain refinement mechanisms of hypoeutectic Al-Si alloys. *Acta Mater.* **44(9)**, 3749-3760 (1996).

[160] V.H. López, A. Scoles, A.R. Kennedy. The thermal stability of TiC particles in an Al7wt.%Si alloy. *Mater. Sci. Eng. A* **356**, 316-325 (2003).

[161] W.F. Riley, L.D. Sturges, D.H. Morris. *Mechanics of Materials*. 6th Ed. Wiley (2009).

[162] Z. Wang, R.J. Zhang. Mechanical behavior of cast particulate SiC/Al (A356) metal matrix composites. *Metall. Trans. A* **22A**, 1585-1593 (1991).

[163] D.F. Susan, T.B. Crenshaw, J.S. Gearhart. The effects of casting porosity on the tensile behavior of investment cast 17-4PH stainless steel. *J. Mater. Eng.Perform.* **24**, 2917-2924 (2015).

[164] R.A. Hardin, C. Beckermann. Effect of porosity on deformation, damage, and fracture of cast steel. *Metall. Mater. Trans. A* **44**, 5316-5332 (2013).

[165] R. Becker. The effect of porosity distribution on ductile failure. *J. Mech. Phys. Solids* **35(5)**, 577-599 (1987).

[166] Myriounis, D.P., Hasan, S.T., & Matikas, T.E. Microdeformation Behaviour of Al-SiC Metal Matrix Composites. *Compos. Interfaces* **15(5)**, 495-514 (2008).

[167] E.S. Palma. On the influence of porosity on the Portevin-Le Chatlier Effect in Sintered Iron. *J. Mater. Eng. Perform.* **5**, 646-650 (1996).

[168] B.Dang, X. Zhang, Y.Z. Chen, C.X. Chen, H.T. Wang, F.Liu. Breaking through the strength-ductility trade-off dilemma in an Al-Si-based casting alloy. *Sci. Rep.* **6**, 30874 (2016).

[169] M. Ostad Shabani, A. Baghani, A. Khorram, F. Heydari. Evaluation of fracture mechanisms in Al-Si metal matrix nanocomposites produced by three methods of gravity sand casting, squeeze casting, and compo casting in semi-solid state. *Silicon* (2020).

[170] L.M. Foster, G. Long, M.S. Hunter. Reactions between aluminum oxide and carbon: The Al2O3 – Al4C3 phase diagram. *J. Am. Ceram. Soc.* **39(1)**, 1-11 (1996).

[171] J.-M. Lihrmann. Thermodynamics of the Al2O3 – Al4C3 system I. Thermochemical functions of Al oxide, carbide, and oxycarbides between 298 and 2100 K. *J. Eur. Ceram. Soc.* **28**, 633-642 (2008).

[172] T.Y. Kosolapova. *Carbides.* 1st Ed. Springer (1971).

[173] J.H. Cox, L.M. Pidgeon. An investigation of the aluminum-oxygen-carbon system. *Can. J. Chem.* **41**, 671-683 (1962).

[174] E. Zhang, S. Zeng, B. Yang, Q. Li, M. Ma. A study on the kinetic process of reaction synthesis of TiC: Part I. Experimental research and theoretical model. *Metall. Mater. Trans. A* **30A**, 1147-1151 (1999).

[175] V. De Andrade, A. Deriy, M.J. Wojcik, D. Gürsoy, D. Shu, K. Fezzaa, F. De Carlo. Nanoscale 3D imaging at the Advanced Photon Source (SPIE, 2016). Accessed 8/20/2019.

[176] C.S. Kaira, V. De Andrade, S.S. Singh, C. Kantzos, A. Kirubanandham, F. De Carlo, N. Chawla. Probing novel microstructural evolution mechanisms in aluminum alloys using 4D nanoscale characterization. *Adv. Mater.* **29**, 1703482 (2017).

[177] J.H. Friedman, J.L. Bentley, R.A. Finkel. An algorithm for finding best matches in logarithmic expected time. *ACM Trans. Math. Software* **1549**, 1-38 (1976).

[178] R. Keinan, H. Bale, N. Gueninchault, E.M. Lauridsen, A.J. Shahani. Integrated imaging in three dimensions: Providing a new lens on grain boundaries, particles, and their correlations in polycrystalline silicon. *Acta Mater.* **148**, 225-234 (2018).

[179] A.J. Shahani, X. Xiao, K. Skinner, M. Peters, P.W. Voorhees. Ostwald ripening of faceted Si particles in an Al-Si-Cu melt. *Mater. Sci. Eng. A* **673**, 307-320 (2016).

[180] D. Gürsoy, F. De Carlo, X. Xiao, C. Jacobsen. TomoPy: A framework for the analysis of synchrotron tomographic data. *J. Synchrotron Radiat.* **21**, 1188-1193 (2014).

[181] B.A. Dowd, G.H. Campbell, R.B. Marr, V.V. Nagarkar, S.V. Tipnis, L. Axe, D.P. Siddons. Developments in synchrotron X-ray computed microtomography at the National Synchrotron Light Source. *Dev. X-ray Tomogr. II Conf. Proc.,* 224-236 (1999).

[182] D.M. Pelt, V. De Andrade. Improved tomographic reconstruction of large-scale real-world data by filter optimization. *Adv. Struct. Chem. Imaging* **2**, 1-14 (2017).

[183] K. Lee, D.S. Stewart, M. Clemenson, N. Glumac, C. Murzyn. Modeling the ignition of a copper oxide aluminum thermite. *AIP Conf. Proc.,* 1-4 (2017).

[184] P.C. Maity, P.N. Chakraborty, S.C. Panigrahi. Al-Al2O3 in situ particle composites by reaction of CuO particles in molten pure Al. *Mat. Lett.* **19**, 1109-1116 (2013).

[185] S.H. Fischer, M.C. Grubelich. A survey of combustible metals, thermites, and intermetallics for pyrotechnic applications. *32nd AIAA/ASME/SAE/ASEE Joint Propul. Conf. Proc.*, 1-13 (1996).

[186] D.S. Stewart. A Gibbs formulation for reactive materials with phase change. *AIP Conf. Proc.*, 1-4 (2017).

[187] R.A. Rapp, X. Zheng. Thermodynamic consideration of grain refinement of aluminum alloys by titanium and carbon. *Metall. Trans. A* **22**, 3071-3075 (1991).

[188] N. Samer, J. Andrieux, B. Gardiola, N. Karnatak, O. Martin, H. Kurita, L. Chaffron, S. Gourdet, S. Lay, O. Dezellus. Microstructure and mechanical properties of an Al-TiC metal matrix composite obtained by reactive synthesis. *Compos. Part A-Eng.* 72, 50-57 (2015).

[189] Q.C. Jiang, H.Y. Wang, Y.G. Zhao, X.L. Li. Solid-state reaction behavior of Al-Ti-C powder mixture compacts. *Mater. Res. Bull.* **40**, 521-527 (2005).

[190] V.V. Dalvi, A.K. Suresh. A contact-point based approach for the analysis of reactions among solid particles. *AIChE J.* **57**, 1329-1338 (2011).

[191] A. Banerji, W. Reif. Development of Al-Ti-C grain refingers containing TiC. *Metall. Trans. A* **17**, 2127-2137 (1986).

[192] M.E. Fine, J.G. Conley. Discussion of "On the free energy of formation of TiC and Al4C3." *Metall. Trans. A* **21A**, 2609-2610 (1990).

[193] Z.W. Liu, Q. Han, J.G. Li. Formation of small blocky Al3Ti particles via direct reaction between solid Ti powders and liquid Al. *Metall. Mater. Trans. A* **43**, 4460-4463 (2012).

[194] V.T. Witusiewicz, B. Hallstedt, A.A. Bondar, U. Hecht, S.V. Sleptsov, T.Y. Velikanova. Thermodynamic description of the Al-C-Ti system. *J. Alloys Compd.* **623**, 480-496 (2015).

[195] U.R. Kattner, J.C. Lin, Y.A. Chang. Thermodynamic assessment and calculation of the Ti-Al system. *Metall. Trans. A* **23A**, 2081-2090 (1992).

[196] J.F. Hair, Jr., W.C. Black, B.J. Babin, R.E. Anderson. *Multivariate Data Analysis*. 7th Ed. Harlow (2014).

[197] A.A.A. Kuylen, T.M.M. Verhallen. The use of canonical analysis. *J. Econ. Psycho.* **1**, 217-237 (1981).

[198] A. Lawrence, J.M. Rickman, M.P. Harmer, A.D. Rollett. Parsing abnormal grain growth. *Acta Mater.* **103**, 681-687 (2016).

[199] V. Uurtio, J.M. Monteiro, J. Kandola, J. Shawe-Taylor, D. Fernandez-Reyes, J. Rousu. A tutorial on canonical correlation methods. *ACM Comput. Surv.* **50**, 1-33 (2017).

[200] A. Sherry, R.K. Henson. Conducting and interpreting canonical correlation analysis in personality research. *J. Pers. Assess.* **3891**, 37-41 (2010).

[201] K.E. Muller. Understanding canonical correlation through the general linear model and principal components. *Am. Stat.* **36**, 342-354 (1982).

[202] J.M. Rickman, Y. Wang, A.D. Rollett, M.P. Harmer, C. Compson. Data analytics using canonical correlation analysis and Monte Carlo simulation. *npj Comput. Mater.* **3**, 1-5 (2017).

[203] R.C. MacCallum, K.F. Widaman, S. Zhang, S. Hong. Sample size in factor analysis. *Psychol. Methods* **4(1)**, 84-99 (1999).

[204] S.L. Weinberg, R.B. Darlington. Canonical analysis when number of variables is large relative to sample size. *J. Educ. Stat.* **1(4)**, 313-332 (1976).

[205] J. Stevens. *Applied Multivariate Statistics for the Social Sciences*. Lawrence Erlbaum Associates, Inc. (1986).

[206] H.-S. Lee. Canonical correlation analysis using small number of samples. *Commun. Stat.-Simul. C.* **36**, 973-985 (2007).

[207] A.K. Chaubey, S. Scudino, N.K. Mukhopadhyay, M.S. Khoshkhoo, B.K. Mishra, J. Eckert. Effect of particle dispersion on the mechanical behavior of Al-based metal matrix composites reinforced with nanocrystalline Al-Ca intermetallics. *J. Alloys Compd.* **536**, S134-S137 (2012).

[208] Z. Wang, M. Song, C. Sun, Y. He. Effects of particle size and distribution on the mechanical properties of SiC reinforced Al-Cu alloy composites. *Mater. Sci. Eng. A* **528**, 1131-1137 (2011).

[209] J. Chen, C. Bao, Y. Ma, Z. Chen. Distribution control of AlN particles in Mg-Al/AlN composites. *J. Alloys Compd.* **695**, 162-170 (2017).

[210] B.M. Tyson, R.K. Abu Al-Rub, A. Yazdanbakhsh, Z. Grasley. A quantitative method for analyzing the dispersion and agglomeration of nano-particles in composite materials. *Compos. Part B-Eng.* **42**, 1395-1403 (2011).

[211] H. Shimazaki, S. Shinomoto. Kernal bandwidth optimization in spike rate estimation. *J. Comput. Neurosci.* **29**, 171-182 (2010).

[212] I. González, S. Déjean, P.G.P. Martin, A. Baccini. CCA: An R package to extend canonical correlation analysis. *J. Stat. Software* **23**, 1-14 (2008).

[213] S. Jin, P. Shen, D. Zhou, Q. Jiang. A common regularity of stoichiometry-induced morphology evolution of transition metal carbides, nitrides, and diborides during self-propagating high-temperature synthesis. *Cryst. Growth Des.* **12**, 2814-2824 (2012).

[214] S. Jin, P. Shen, Q. Lin, L. Zhan, Q. Jiang. Growth mechanism of TiCx during self-propagating high-temperature synthesis in an Al-Ti-C system. *Cryst. Growth Des.* **10**, 1590-1597 (2010).

[215] B.X. Dong, H.Y. Yang, F. Qiu, Q. Li, S.L. Shu, B.Q. Zhang, Q.C. Jiang. Design of TiCx nanoparticles and their morphology manipulating mechanisms by stoichiometric ratios: Experiment and first-principle calculation. *Mater. Design* **181**, 107951-107951 (2019).

[216] D. Zhang, H. Liu, L. Sun, F. Bai, Y. Wang, J. Wang. Shape-controlled TiCx particles fabricated by combustion synthesis in the Cu-Ti-C system. *Crystals* **7**, pp. 1-12 (2017).

[217] L. Arnberg, L. Bäckerud, H. Klang. Intermetallic particles in Al-Ti-B-type master alloys for grain refinement of alumninum. *Met. Technol.* **9**, 7-13 (1982).

[218] D.H. St. John, L.M. Hogan. Metallography and growth crystallography of Al3Ti in Al-Ti alloys up to 5 wt% Ti. *J. Cryst. Growth* **46**, 387-398 (1979).

[219] M.S. Lee, B.S. Terry. Effects of processing parameters on aluminide morphology in aluminum grain refining master alloys. *Mater. Sci. Tech.* **7**, 608-612 (1991).

[220] V. Auradi, S.A. Kori. Influence of reaction temperature for the manufacturing of Al-3Ti and Al-3B master alloys. *J. Alloys Compd.* **453**, 147-156 (2008).

[221] J. Zhao, T. Wang, J. Chen, L. Fu, J. He. Preparation of Ti3AlC2 and Ti2AlC by self-propagating high-temperature synthesis. *Materials* **10**, 1-10 (2017).

[222] E.G. Kandalova, V.I. Nikitin, J. Wanqi, A.G. Makarenko. Effects of Al powder content on SHS Al-Ti grain refiner. *Matt. Lett.* **54**, 131-134 (2002).

[223] J. Zhao, T. Wang, J. Chen, L. Fu, J. He. Effect of cooling rate on morphology of TiAl3 particles in Al-4Ti master alloy. *Materials* **10**, 1-10 (2017).

[224] Z. Liu, M. Rakita, X. Wang, W. Xu, Q. Han. In situ formed Al3Ti particles in Al alloy matrix and their effects on the microstructure and mechanical properties of 7075 alloy. *J. Mater. Res.* **29(12)**, 1354-1361 (2014).

[225] X. Wang, A. Jha, R. Brydson. In situ fabrication of Al3Ti particle reinforced aluminum alloy metal-matrix composites. *Mater. Sci. Eng., A* **364**, 339-345 (2004).

[226] R. Nikbakht, H. Assadi. Phase-field modelling of self-propagating high-temperature synthesis of NiAl. *Acta Mater.* **60**, 4041-4053 (2012).

[227] N. Provatas, M. Grant, K.R. Elder. Phase-field model for activated reaction fronts. *Phys. Rev. B* **53(10)**, 6263-6272 (1996).

[228] B.B. Khina, B. Formanek, I. Solpan. Limits of applicability of the "diffusion-controlled product growth" kinetic approach to modeling SHS. *Physica B* **355**, 14-31 (2005).

[229] M. Ge, D.S. Coburn, E. Nazaretski, W. Xu, K. Gofron, H. Xu, Z. Yin, W.-K. Lee. Design, characterization, and performance of a hard X-ray transmission microscope at the National Synchrotron Light Source II 18-ID beamline. *Appl. Phys. Lett.* **113**, 053701 (2018).

[230] G. Requena, G. Garcés, S. Danko, T. Pirling, E. Boller. The effect of eutectic Si on the strength of short-fibre-reinforced Al. *Acta Mater.* **57**, 3199-3210 (2009).

[231] W. Li, S. Cui, J. Han, C. Xu. Effect of silicon on the casting properties of Al-5.0% Cu alloy. *Rare Met.* **25(6)**, 133-135 (2006).

[232] X.-G. Chen, M. Fortier. TiAlSi intermetallic formation and its impact on the casting processing in Al-Si alloys. *J. Mater. Process. Technol.* **210**, 1780-1786 (2010).

[233] N. Saheb, T. Laoui, A.R. Daud, M. Harun, S. Radiman, R. Yahaya. Influence of Ti addition on wear properties of Al-Si eutectic alloys. *Wear* **249(8)**, 656-662 (2001).

[234] J.M. Rickman, H.M. Chan, M.P. Harmer, J.A. Smeltzer, C.J. Marvel, A. Roy, G. Balasubramanian. Materials informatics for the screening of multi-principal elements and high-entropy alloys. *Nat. Commun.* **10**, 2618 (2019).

[235] Y. Choi, S.-W. Rhee. Reaction of TiO2-Al-C in the combustion synthesis of TiC-Al2O3 composite. *J. Am. Ceram. Soc.* **78(4)**, 986-992 (1995).

[236] T.D. Xia, Z.A. Munir, Y.L. Tang, W.J. Zhao, T.M. Wang. Structure formation in the combustion synthesis of Al2O3-TiC composites. *J. Am. Ceram. Soc.* **83(3)**, 507-512 (2000).

[237] R. Shi, J.M. Maier, A.A. Luo. Controlling particle/melt interactions in metal matrix composites during solidification: The role of melt viscosity and cooling rate. *Metall. Mater. Trans. A* **50A**, 3736-3747.

[238] J.Q. Xu, L.Y. Chen, H. Choi, X.C. Li. Theoretical study and pathways for nanoparticle capture during solidification of metal melt. *J. Phys.: Condens. Matter* **24**, 255304 (2012).

[239] A. Dehghan Hamedan, M. Shahmiri. A new model for the solidification of metal matrix nanocomposites: Wet cluster engulfment of nanoparticles by the solidification front. *J. Compos. Mater.* **51(20)**, 2913-2932 (2017).

[240] Y. Wang, J. Shi. Engulfment and distribution of second-phase nanoparticles during dendrite solidification of an Al-Si binary alloy: A simulation study. *Appl. Phys. A* **125**, 449 (2019).

[241] H. Aufgebauer, J. Kundin, H. Emmerich, M. Azizi, C. Reimann, J. Friedrich, T. Jauß, T. Sorgenfrei, A. Cröll. Phase-field simulations of particle capture during the directional solidification of silicon. *J. Cryst. Growth* **446**, 12-26 (2016).

[242] A.J. Clarke, D. Tourret, S.D. Imhoff, P.J. Gibbs, K. Fezzaa, J.C. Cooley, W.-K. Lee, A. Deriy, B.M. Patterson, P.A. Papin, K.D. Clarke, R.D. Field, J.L. Smith. X-ray imaging and controlled solidification of Al-Cu alloys toward microstructures by design. *Adv. Eng. Mater.* **17(4)**, 454-459 (2015).

[243] A.J. Clarke, D. Tourret, Y. Song, S.D. Imhoff, P.J. Gibbs, J.W. Gibbs, K. Fezzaa, A. Karma. Microstructure selection in thin-sample directional solidification of an Al-Cu alloy: In situ X-ray imaging and phase-field simulations. *Acta Mater.* **129**, 203-216 (2017).

[244] A. Bogno, H. Nguyen-Thi, A. Buffet, G. Reinhart, B. Billia, N. Mangelinck-Noël, N. Bergeon, J. Baruchel, T. Schenk. Analysis by synchrotron X-ray radiography of convection effects on the dynamic evolution of the solid-liquid interface and on solute distribution during the initial transient of solidification. *Acta Mater.* **59(11)**, 4356-4365 (2011).

[245] R.H. Mathiesen, L. Arnberg, Y. Li, V. Meier, P.L. Schaffer, I. Snigireva, A. Snigirev, A.K. Dahle. X-ray videomicroscopy studies of eutectic Al-Si solidification in Al-Si-Cu. *Metall. Mater. Trans. A* **42A**, 170-180 (2011).

[246] F. Sun, H. Markötter, I. Manke, A. Hilger, S.S. Alrwashdeh, N. Kardjilov, J. Banhart. Complementary X-ray and neutron radiography study of the initial lithiation process in lithium-ion batteries containing silicon electrodes. *Appl. Surf. Sci.* **399**, 359-366 (2017).

[247] B.R. Halls, C.D. Radke, B.J. Reuter, A.L. Kastengren, J.R. Gord, T.R. Meyer. High-speed, two-dimensional synchrotron white-beam X-ray radiography of spray breakup and atomization. *Opt. Express* **25(2)**, 1605-1617 (2017).

[248] C.F. Powell, Y. Yue, R. Poola, J. Wang. Time-resolved measurements of supersonic fuel sprays using synchrotron X-rays. *J. Synchrotron Rad.* **7**, 356-360 (2000).

[249] S.-B. Li, W.-H. Xiang, H.-X. Zhai, Y. Zhou. Formation of TiC hexagonal platelets and their growth mechanisms. *Powder Technol.* **185**, 49-53 (2008).

[250] R. Yu, Q. Zhan, L.L. He, Y.C. Zhou, H.Q. Ye. Si-induced twinning of TiC and formation of Ti_3SiC_2 platlets. *Acta Mater.* **50**, 4127-4135 (2002).

[251] J. Nie, X. Liu, X. Ma. Influence of trace boron on the morphology of titanium carbide in an Al-Ti-C-B master alloy. *J. Alloys Compd.* **491**, 113-117 (2010).

[252] M. Wang, Q. Han. Particle pushing during solidification of metals and alloys. *Mater. Sci. Forum* **783-786**, 1513-1517 (2014).

[253] R.J. Feller, C. Beckermann. Modeling of solidification of metal-matrix particulate composites with convection. *Metall. Mater. Trans. B* **28B**, 1165-1183 (1997).

[254] A.R. Kennedy, T.W. Clyne. Particle pushing during the solidification of metal matrix composites. *Cast Met.* **4(3)**, 160-164 (1991).

[255] F.R. Juretzko, B.K. Dhindaw, D.M. Stefanescu, S. Sen, P.A. Curreri. Particle engulfment and pushing by solidifying interfaces: Part I. Ground experiments. *Metall. Mater. Trans. A* **29A**, 1691-1696 (1998).

[256] J.W. Garvin, H.S. Udaykumar. Particle-solidification front dynamics using a fully coupled approach, Part II: comparison of drag expressions. *J. Cryst. Growth* **252**, 467-479 (2003).

[257] I.B. Ozsoy, G. Li, H. Choi, H. Zhao. Shape effects on nanoparticle engulfment for metal matrix nanocomposites. *J. Cryst. Growth* **422**, 62-68 (2015).

[258] J.K. Kim, P.K. Rohatgi. The effect of the diffusion of solute between the particle and the interface on the particle pushing phenomena. *Acta Mater.* **46(4)**, 1115-1123 (1998).

[259] G. Kaptay. Interfacial criterion of spontaneous and forced engulfment of reinforcing particles by an advancing solid/liquid interface. *Metall. Mater. Trans. A* **32A**, 993-1005 (2001).

[260] J.W. Garvin, H.S. Udaykumar. Particle-solidification front dynamics using a fully coupled approach, Part I: methodology. *J. Cryst. Growth* **252**, 451-466 (2003).

[261] R. Shi, J.M. Meier, A.A. Luo. Controlling particle/metal interactions in metal matrix composites during solidification: The role of melt viscosity and cooling rate. *Metall. Mater. Trans. A* **50A**, 3736-3747 (2019).

[262] L.-Y. Chen, J.-Q. Xu, X.-C. Li. Controlling phase growth during solidification by nanoparticles. *Mater. Res. Lett.* **3(1)**, 43-49 (2015).

[263] C. Cao, G. Yao, L. Jiang, M. Sokoluk, X. Wang, J. Ciston, A. Javadi, Z Guan, I. De Rosa, W. Xie, E.J. Lavernia, J.M. Schoenung, X. Li. Bulk ultrafine grained/nanocrystalline metals via slow cooling. *Sci. Adv.* **5**, 1-10 (2019).

[264] R. Daudin, S. Terzi, P. Lhuissier, J. Tamayo, M. Scheel, N. Hari Babu, D.G. Eskin, L. Salvo. Particle-induced morphological modification of Al alloy equiaxed dendrites revealed by sub-second in situ microtomography. *Acta Mater.* **125**, 303-310 (2017).

[265] L.-Y. Chen, J.-Q. Xu, H. Choi, H. Konishi, S. Jin, X.-C. Li. Rapid control of phase growth by nanoparticles. *Nat. Comm.* **5**, 3879 (2014).

[266] E. Guo, S. Shuai, D. Kazantsev, S. Karagadde, A.B. Phillion, T. Jing, W. Li, P.D. Lee. The influence of nanoparticles on dendritic grain growth in Mg alloys. *Acta Mater.* **152**, 127-137 (2018).